Linking Super Earth Composition to Planet Formation History

LINKING SUPER EARTH COMPOSITION TO PLANET FORMATION HISTORY

By

MATTHEW J. ALESSI, B.SC.

A Thesis Submitted to the School of Graduate Studies in Partial Fulfillment of the Requirements for the Degree Master's of Physics McMaster University

Descriptive Note

MASTER OF PHYSICS (2016) McMaster University (Physics and Astronomy) Hamilton, Ontario
AUTHOR: Matthew J. Alessi, B.Sc. (McMaster University)
SUPERVISOR: Dr. Ralph E. Pudritz
NUMBER OF PAGES: xi, 129

Abstract

Super Earths are a class of exoplanets with masses between 1-10 $M_\oplus$. Comprising nearly 70 % of the discovered planet population, they are largest class of exoplanets known. Super Earths exhibit an interesting variety of compositions, as their densities imply that they range from dense, rocky planets to those with substantial amounts of water. This thesis aims to understand why super Earths form so frequently, and to connect the final compositions of super Earths to the regions where they form in protoplanetary disks. To do this, we combine a model that calculates the physical and chemical conditions within a protoplanetary disk with a core accretion model of planet formation. A key feature of our planet formation model is planet traps that act as barriers to rapid type-I migration. The traps we include in our model are the dead zone, which can be caused by cosmic ray or X-ray ionization, the ice line, and the heat transition. In disks with lifetimes $\gtrsim$ 4 Myr we find that planet formation in all traps results in Jovian planets. Typically, the X-ray dead zone and heat transition traps produce hot Jupiters orbiting near 0.05 AU while the cosmic ray dead zone and ice line traps produce Jupiters near 1 AU. Super Earths are found to form in disks with short lifetimes $\lesssim$ 2 Myr that photoevaporate prior to planets undergoing runaway gas accretion. Additionally, we find that super Earth formation takes place in low-mass disks ($\lesssim$ 0.05 $M_\odot$), where planet formation timescales exceed disk lifetimes inferred through observations. The location of various traps throughout the disk play a key role in allowing super Earths to achieve a range of compositions. Super Earths forming in the ice line or heat transition accrete solids from cold regions of the disk, resulting in planets with large ice contents (up to 50 % by mass). Conversely, super Earths formed in the dead zone trap accrete solids from warm regions of the disk and are therefore composed of mostly rocky materials (less than 5 % ice by mass).

Acknowledgments

I am indebted to many individuals who helped me along the course of this two-year project. First, I would like to thank my supervisor, Prof. Ralph Pudritz for his consistent encouragement and guidance throughout this thesis. His enthusiasm and knowledge has made this research a rewarding experience and I very much look forward to continue working with him during my doctoral work. I am also thankful for the helpful conversations and committee support from Prof. James Wadsley and Prof. Christine Wilson.

This thesis' work builds upon previous work done by Dr. Yasuhiro Hasegawa during his thesis here at McMaster. I have benefitted from several conversations with him during the course of this thesis. His explanations on several aspects of this thesis' planet formation model - of which a large portion was developed and worked on by Yasuhiro - were especially helpful.

I have benefitted from many conversations with Dr. René Heller during and after his time spent at McMaster working as a postdoctoral fellow. I would like to thank René for his many helpful suggestions and insights regarding this thesis' planet formation model, implications of results, and prospects for future work.

I would also like to thank all of my fellow McMaster astronomy graduate students, past and present, for making this department such a friendly and enjoyable work environment. I have many fond memories of our frequent trips to the Phoenix, evenings playing on the department Liquid State softball team, and everyone tolerating my quality puns.

In particular, I would like to thank Alex Cridland, with whom I have worked with on overlapping projects during my MSc. Alex has made many contributions to this thesis - debugging HSC chemistry software, assistance in developing and working with our planet formation model, interpreting results, and discussing future direction and extensions of this project.

On a personal level, I would like to thank all my family and friends for their love and support throughout this project. In particular, I thank my parents John and Tamara Alessi for their kind encouragement during my academics, and for teaching me the values of hard work and dedication throughout my upbringing which have proven useful as I work to overcome hurdles and achieve my goals. I thank my sister, Danielle Alessi, for setting me up for success by teaching me how to do multiplication and long-division at the young age of three. I thank Angelo Arcaro for always being my dear friend and someone to talk to about anything and everything. Lastly, I thank "the gang" – Laura Bottrell, Danielle Janicas, Shawn McInnis, John McIntyre, Ashlyn Richard, and Jim Rudolph – for relieving stress with great company and yearly camping trips.

Finally, I would like to sincerely thank my fiancée (soon to be wife!) Janelle Davey for her continued unconditional love and emotional support. Thank you for giving me encouragement and confidence during the times when my studies were overbearing.

Now, on to the doctoral work!

Contents

List of Figures

List of Tables

Chapter 1

Introduction

Over recent years, observations have revealed the existence of a wealth of planets orbiting stars other than the Sun. The observed masses, radii, and semi-major axes among the vast numbers of exoplanets contrast considerably with the planets in the Solar system, and this challenges our understanding of how planets form (Rowe et al., 2014). For example, the first exoplanets observed had masses comparable to that of Jupiter, yet orbit extremely close to their host stars, with semimajor axes between 0.05 and 0.5 AU (Mayor & Queloz, 1995; Butler & Marcy, 1996). The orbital radii of these planets are much different than the Jovian planets in the Solar system, whose closest orbit to the Sun is 5.2 AU. More recent observations have revealed an abundance of planets with masses between that of the Earth, and that of Neptune (whose mass is roughly 17 $M_\oplus$), orbiting with semimajor axes of 0.01 - 0.5 AU from their host stars (Udry & Santos, 2007; Borucki et al., 2011; Mayor et al., 2011; Cassan et al., 2012). As these planets - so called super Earths - do not possess a Solar system analogue, the observations of such planets again challenged our understanding of how planets form.

One of the two main methods of observing exoplanets is through the technique of radial velocity. In a two-body problem, gravitationally bound bodies will orbit their mutual centre of mass. When viewing a star that hosts an orbiting planet edge-on, the star's motion around the centre of mass will result in a sinusoidally varying radial velocity. The radial velocity technique involves observing the star's motion (induced by the planet) through Doppler shifting of its spectral lines. Such observations can decipher the minimum mass[1] of the planet through the amplitude of Doppler shifts, as well as the

[1] The RV method can only infer a lower limit, or minimum mass of the planet, as the inclination of the disk to the observer's line of sight is often unknown. The RV amplitude gives us the planet's $M_p \sin i$, where i is the inclination of the system.

planet's orbital period by how frequently the star's radial velocity oscillates. This method relies on the star moving appreciably throughout the planet's orbit in order to result in detectable velocities. Thus, the planet-star centre of mass must be displaced substantially from the star's centre. The radial velocity method therefore is biased to observing high mass planets, with roughly the mass of Jupiter, on short-period orbits, as these planets displace the centre of mass the most and provide favourable conditions for detecting planets with this method. The radial velocity method is therefore best-suited to detecting Jovian planets with semimajor axes $\lesssim 1$ AU.

The radial velocity method was used to detect the first exoplanets around sun-like stars (Mayor & Queloz, 1995; Butler & Marcy, 1996; Marcy & Butler, 1996). In each case, the detected planet was a Jovian planet several times the mass of Jupiter. In these RV measurements, the planet's minimum masses were only certain to roughly 10-20% due to limitations on the radial velocity precision of such measurements, which was roughly 10 m/s. Subsequent RV observations have been used to detect less massive planets, comparable in mass to Jupiter (Mayor et al., 2004), and even Neptune (Melo et al., 2007). Modern RV observations are achieving high precisions close to 1 m/s, and are therefore capable of detecting planets with smaller mass uncertainties (Mordasini et al., 2015).

The second main detection method is the transit method. Viewing a planet-hosting star edge-on will result in the planet crossing the stellar disk during its orbit, blocking a fraction of the light that can reach us. The planet's orbit will then cause a periodic decrease in the flux received from the star, and the amount by which it decreases scales with the radial size of the planet. If the planet is large enough (blocking $\gtrsim 0.1$ % of the host-star's flux), this decrease will be detectable, and the presence of a planet can be inferred. This method allows for the radial size of the planet to be measured, as well as its orbital period through the time between decreases in the star's brightness. Similarly to the RV method, detection via transits also favours massive planets on short-period orbits, as transits by these planets cause the largest changes in the star's brightness. The transit method's capability to detect planets is highly sensitive to the system's inclination, as transit events can only be observed when the planet's orbit is nearly edge-on with respect to the observer's line of sight. Follow-up observations using the RV method is a way of confirming transit detections.

In March of 2009, the Kepler telescope was launched into space. The Kepler mission was designed to target Sun-like stars in the Milky Way to detect Earth-like terrestrial planets via the transit method. Particular importance was placed on determining what fraction of these terrestrial worlds orbited within their host stars' habitable zones - the region where a planet has the right surface temperature to harbour liquid water on its surface - in an effort to find Earth analogues. The telescope observed a 105 square degree field of view, harbouring over 10^5 stars, which were monitored for over 3.5 years. The instrument was designed to have enough sensitivity to detect terrestrial planets in transit of G-type stars, after accounting for stellar variability.

Analyzing the data taken with Kepler allowed for planetary candidates to be selected. In these cases, transits were found to be present in the stars' light curves, suggesting the presence of a planet, or multiple planets. Radial velocity follow up measurements were then performed to confirm these observations, retrieving planet masses and semimajor axes. The first Kepler data release in 2014 revealed over 1000 exoplanets detected with this survey, and this represented only a fraction of the candidates found with Kepler (Rowe et al., 2014). The planets revealed in this data release displayed a range of masses, from that of Earth up to and beyond Jupiter's mass, and a range of semimajor axes. More recently, a statistical approach was used to confirm over 1000 more Kepler candidates within a 99 % confidence interval (Morton et al., 2016).

The data retrieved with the Kepler mission has provided the vast majority of current exoplanet data. The observations provided by this mission have played a crucial role in driving the field of exoplanet science. The current science being done with the Atacama Large Millimetre/sub-millimetre array (ALMA), as well as future missions such as James Webb Space Telescope and the PLAnetary Transits and Oscillations of stars (PLATO) mission will maintain the advances in this field over the coming decades. Planet formation theories have changed drastically as a result of constraints provided by the Kepler data, and the new types of planets without Solar system analogues it has revealed. Now, with nearly 3000 confirmed exoplanets, we are starting to gain a statistical understanding of what the process of planet formation results in. Since the Kepler mission specifically targeted Sun-like stars in the search for Earth like planets, the data retrieved from this mission is likely biased as it corresponds to only a particular stellar type.

In figure 1.1, we show the distribution of confirmed exoplanets on the mass semimajor axis diagram (left panel). As was first done in Chiang & Laughlin (2013), this diagram can be divided into zones outlining different classes of planets, or planet populations. Zone 1 corresponds to hot Jupiters, zone 2 to warm Jupiters, zone 3 to Jupiters orbiting near 1 AU, zone 4 to directly imaged Jovians, and zone 5 to super Earths and hot Neptunes. The frequencies by which planets populate different zones inform planet formation theories as they reveal what types of planets formation processes tend to produce. For example, among the high mass Jovian regions of the diagram (zones

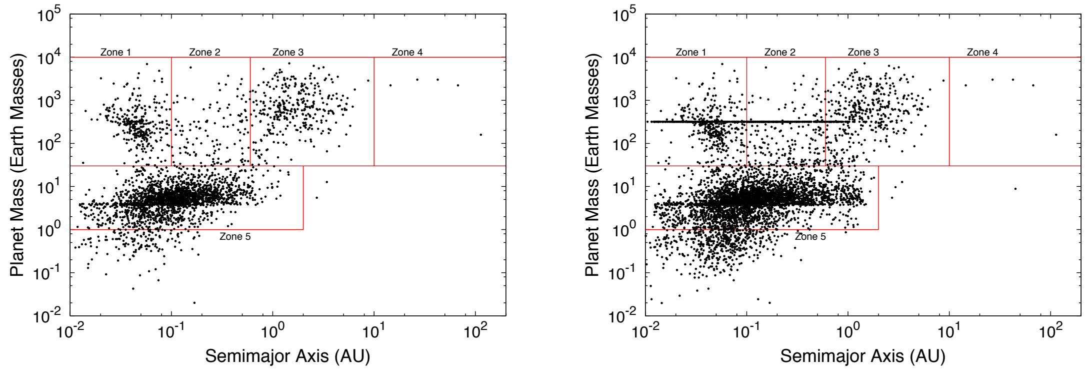

Figure 1.1: The mass semimajor axis distribution of exoplanets, with data taken from *exoplanets.org* on July 12, 2016. **Left Panel:** The observed distribution of confirmed exoplanets. Confirmed planets populate zones of the diagram with the following frequencies: zone 1: 10.36%, zone 2: 4.26%, zone 3: 11.35%, zone 4: 0.17 %, zone 5: 67.78 %.
Right Panel: Both confirmed and unconfirmed planets are shown. This data set populates zones with frequencies: zone 1: 10.56%, zone 2: 7.36%, zone 3: 8.02%, zone 4: 0.09%, zone 5: 63.08%.

1-4), we see that zone 3 is the most frequently populated, meaning Jupiters are most likely to form and end up on orbits of roughly 1-2 AU than they are to form into short-period orbits. By far the most frequently populated zone of the diagram is zone 5, corresponding to super Earths and hot Neptunes. The large frequency by which planets populate this zone tell us that the process of planet formation favours the formation of lower mass (1-30 $M_\oplus$) planets as opposed to massive Jupiters.

In the right panel of figure 1.1, we include the $\sim$ 2500 unconfirmed candidates on the diagram. The unconfirmed planets tend to lie along horizontal bands across the diagram, as their masses have yet to be determined through radial velocity follow-ups. Instead, their masses are estimated via the radii determined through transit depths (using a simple model which uses observed radii to infer planet mass). Comparing the confirmed planets with this data set, containing both unconfirmed candidates and confirmed planets, we see that the unconfirmed planets fill in the inner regions of the diagram, especially zone 2. Additionally, low mass candidates lying beneath zone 5 comprise a large fraction of the unconfirmed population.

In figure 1.2, we show another key exoplanet distribution on the mass-radius diagram. This diagram shows that planets of all masses display a range of radii corresponding to a range of mean densities. Massive planets having a large fraction of their mass in a gaseous atmosphere have radii sensitive to the amount of flux received from their host stars, as this alters their atmospheric struc-

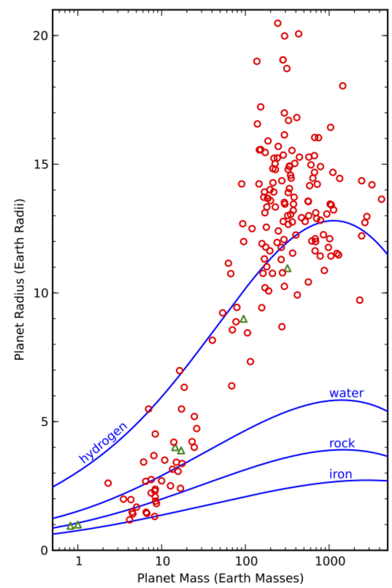

Figure 1.2: The mass-radius distribution of exoplanets is shown in red data points. The green data points correspond to Solar system planets. Blue curves show mass-radius relations for spheres of homogeneous compositions. This diagram illustrates that planets over all sizes have a range of mean densities. For planets with massive atmospheres, this range of radii can be explained by differing stellar fluxes impinging on the planets. Conversely, for the low mass super Earths whose masses are primarily in solids, the range of densities suggests a variety of compositions. *Credit: Howard et al. (2013).*

tures. Super Earths, conversely, lie closer to the curves corresponding to planets whose mass is primarily in solids. The range of mean densities for these planets show that super Earths as a population have a range of solid compositions (Wolfgang, Rogers & Ford, 2015).

The goal of this thesis is to reproduce the characteristics of the population of exoplanets with a theoretical model of planet formation. Namely, we would like to understand the physical mechanisms by which different classes of planets form. We additionally aim to reproduce the interesting variety of compositions shown among super Earths. To do this, we will combine models of a protoplanetary disk that describes the physical and chemical environment out of which planets form, with a core accretion model of planet formation. The core accretion model is a bottom-up model of planet formation, that predicts planet formation to take place through the formation of a solid core before accretion of a gaseous envelope. A key feature of the core accretion model studied in this thesis is the inclusion of planet traps - barriers to the rapid inward migration of forming planets. The combination of disk chemistry and planet formation modelling will allow us to track the materials accreted onto planets during their formation, and calculate the final compositions of planets formed with our model. The combination of these two models will allow us to study the link between super Earth compositions and the region(s) in the disk where they formed.

This thesis is structured as follows. In the remaining sections of this chapter, we give a physical background and overview of the sub-fields of astrophysics our model considers: protoplanetary disk observations and theory (1.1), disk chemistry (1.2), the core accretion model (1.3), and planet migration & traps (1.4). Lastly, in sections 1.5 & 1.6, we outline population synthesis models and planet interior structure models, respectively, as extensions of this thesis' model and prospects for future work. In chapter 2, we give a detailed quantitative description of our model (section 2.2), present planet formation and composition results (2.3), and discuss how our work compares with results obtained by other authors (2.4). In chapter 3, we study our planet formation model's sensitivities by performing parameter studies, and discuss extensions of this model to population synthesis studies. Lastly, chapter 4 highlights the main conclusions of this thesis.

1.1 Protoplanetary Disks

Star formation takes place through the gravitational collapse of a molecular cloud core. As a consequence of angular momentum conservation throughout this collapse, the core's material does not all fall directly onto the protostar. Rather, most of the material will collapse and form into a disk of material orbiting around the star, with distance from the star determined by how much angular momentum the material possesses (Hartmann, 1998). This disk, known as a protoplanetary disk, is a disk of gas and μm-sized dust that provides the material out of which a planetary system can form. Stable protoplanetary disks are a natural result of star formation and are predicted to exist around stars in the T-Tauri phase of their formation. Since all stars with main-sequence masses of $\lesssim 3$ $M_\odot$ undergo this formation phase, planet formation has the potential to take place within disks around every such star.

Since planet formation takes place within the environment of a protoplanetary disk, understanding the physical conditions throughout the disk is a first step in theoretical studies of planet formation. The density of gas and dust throughout the disk are of crucial importance to planet formation as they determine the accretion timescales onto planets. Additionally, as disks represent an intermediate process in star formation, they have finite lifetimes (~ 3 Myr) which set the upper limit to how long planets have to form. The process of disk evolution connects the initial state of the disk to its conditions at the end of its lifetime, and modelling this process is important since planets form over Myr timescales in the core accretion scenario. Lastly, the temperatures and pressures throughout the disk set thermodynamic conditions for disk chemistry, determining what materials are present for planets to accrete. The remainder of this section will discuss observational constraints of protoplanetary disks and different theoretical methods of modelling disk structure. Disk structure and evolution is a key component of this thesis' model, and section 2.2.1 provides a detailed quantitative description of how this modelling is done.

1.1.1 Observational Constraints of Disk Masses and Lifetimes

Protoplanetary disks can be detected around stars spectroscopically via excess radiation in infrared wavelengths. This excess IR emission arises due to dust grains throughout the disk absorbing radiation from the protostar and re-emitting at wavelengths that are characteristic of the size of the dust grains themselves. The spectral energy distribution (SED) observed from the star will therefore be a sum of those arising from the protostar and the processed radiation from dust in the disk. One can approximate the disk's SED by modelling the disk as a series of annuli, each emitting as blackbodies at the local disk temperature, and summing the radiation emitted by each annulus. The flux emitted by an annulus at a radius r from the protostar will be dependent on the disk's temperature $T(r)$, and optical depth $\tau_\nu(r)$ from the disk's midplane to photosphere. The optical depth can be written as,

$$\tau_\nu(r) = \Sigma(r)\kappa_\nu(r)/2 \ , \tag{1.1}$$

where $\Sigma(r)$ is the disk's column density and $\kappa_\nu(r)$ is the disk's opacity. In principle, by tuning $T(r)$, $\Sigma(r)$, and $\kappa_\nu(r)$, one can find a set of profiles that fits the observed SED, and in doing so obtain the disk's structure. In practice, this is a difficult and degenerate problem, so deriving disk structure via SED fitting is an unreliable method (Roberge, 2010). Theoretical models are therefore useful tools in understanding disk structure. Disk structure models can provide radial temperature and surface density profiles, while one needs to consider disk chemistry to calculate opacities, which is discussed in section 1.2. The remainder of this subsection will focus on observational constraints of disk quantities, as a preceding discussion to theoretical modelling.

Disk lifetimes can be estimated by observing the fraction of stars whose SEDs possess IR excess in star clusters whose age is known. By performing observations in many young clusters, one can find a correlation between the fraction of stars with disks (inferred through IR excesses) in a cluster, and the age of the cluster. In doing so, one finds that nearly 100 % of stars in young clusters, with ages $\lesssim$ 1 Myr, have disks. As more evolved systems are considered, one finds that the fraction of stars with disks decreases to roughly 50% for 3 Myr-old clusters, and to nearly 0% for clusters older than 6 Myr (Hernández et al., 2007; Armitage, 2010). This provides a means of estimating of the average lifetime of a protoplanetary disk, as the observations suggest that on average disks will exist around young stars for 3 Myr.

However, this method does have several sources of uncertainty. Observations of IR excess trace the dust around a star as opposed to the gas. It is possible that the gas around a star has disappeared leaving behind the dust in a debris disk. Unfortunately, direct observation of disk gas is extremely limited, and current observations are forced to infer disk gas through the presence of dust. Furthermore, observations and models of clusters suggest that the dispersion in disk lifetimes within clusters can vary by up to an order of magnitude (Roberge, 2010). Thus, the disk lifetime is a somewhat poorly constrained quantity. Nonetheless, a fiducial disk lifetime of 3 Myr is generally used, with 1 and 10 Myr taken as lower and upper limits, respectively.

The disk mass is one of the most important quantities for disk structure as well as for planet formation, yet it is poorly constrained observationally. Disk masses can be estimated using the amount of IR excess the host star's SED possesses (Beckwith et al., 1990). Using radiative transfer equations, the luminosity (L_ν) from a spatially thin axisymmetric disk is (Hartmann, 1998),

$$\nu L_\nu = 4\pi\mu \int_{r_{in}}^{r_{out}} \nu B_\nu(T)(1 - \exp(-\tau_\nu/\mu))2\pi R dR \ , \tag{1.2}$$

where r_{in} and r_{out} are the inner and outer radii of the disk, $B_\nu(T)$ is the Planck function at disk temperature T at radius R, $\mu = \cos i$ where i is the disk inclination, and τ_ν is the optical depth. If the optical depth is large ($\tau_\nu >> 1$) then the luminosity depends only on the disk temperature structure and is independent of the disk mass. In the alternate case where the optical depth is small ($\tau_\nu << 1$), equation 1.2 can be written as,

$$\nu L_\nu = 4\pi \int_{r_{in}}^{r_{out}} \nu B_\nu(T)\kappa_\nu \Sigma(R) 2\pi R dR \ . \tag{1.3}$$

If the radiation is observed at wavelengths where the disk is optically thin, then this formula can be used to estimate a total disk mass from the observed flux. This calculation requires an estimation of the surface density and temperature power law profiles, however.

There are three main problems or uncertainties associated with inferring the total disk's mass via the amount of radiation received from μm dust grains. The most apparent one is that this method relies on the estimated dust to gas ratio in the disk, which is often taken to be 1:100 - the value seen in molecular clouds (Roberge, 2010). Secondly, dust grains coagulate and grow into 10 cm-sized pebbles, or even into km-sized planetesimals over short timescales. These processes act to remove μm dust throughout the disk. Thus, the IR excess may not even indicate the amount of solid material in the disk. Lastly, if the disk is optically thick to IR radiation in certain regions, the SED will underestimate the amount of dust in those regions. In these high-density regions of the disk, IR radiation from the disk's midplane will be absorbed prior to escaping the disk, and the observed radiation will only probe a portion of the disk's vertical extent (Roberge, 2010).

With these uncertainties in mind, observational estimations of disk masses are poorly constrained, with an extremely large range of disk masses ranging from 0.0004 $M_\odot$ to 0.2 $M_\odot$ inferred from observations of disks in star forming regions (Andrews & Williams, 2005; Williams et al., 2005; Andrews & Williams, 2007). An additional source of scatter is expected when considering stars of different masses, as disk masses are expected to correlate with stellar mass. Additionally, disks are not static structures but are rather evolving as stellar accretion takes place. Their masses are expected to vary throughout this evolution, providing another source of scatter.

Stellar accretion rates can be estimated through the amount of excess emission is seen in the UV portion of the spectrum. Physically, it is caused by disk material falling along stellar magnetic field lines in a process known as "magnetospheric accretion" (Hartmann, 1998). Typical disk accretion rates estimated with this method are $10^{-8} - 10^{-7}$ $M_\odot$/yr, but can vary by over an order of magnitude above or below this range (Armitage, 2010). Separating the radiation caused by accretion from that of the star is difficult, and leads to uncertainties in this method. Accretion rates therefore are poorly constrained, much like disk masses.

We are restricted to working with SED fitting when we cannot spatially resolve disks. However, the high degree of spatial resolution and sensitivity provided by the Atacama Large Millimeter/submillimeter Array (ALMA) have allowed us to uncover detailed disk structure in recent infrared and sub-mm wavelength observations (ALMA Partnership et al., 2015). Figure 1.3 shows the ALMA disk image of the HL Tauri disk, showing several ring-like structures, or gaps throughout the disk.

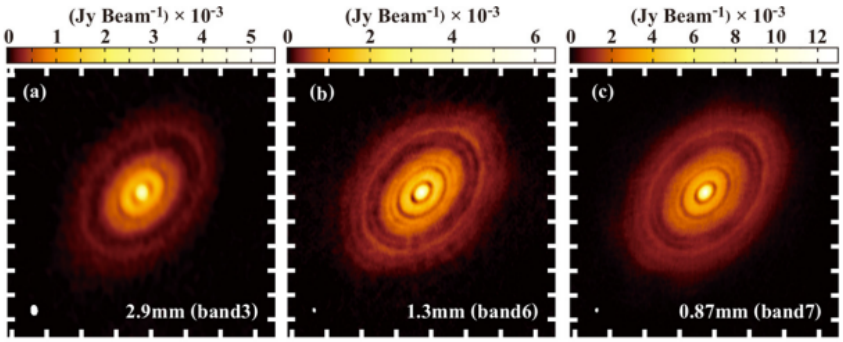

Figure 1.3: Images of the HL Tau disk are shown. The three images correspond to observations at different wavelengths, which probe dust grains of different sizes. *Credit: Akiyama et al. (2016).*

The radiation detected by observations in the IR/sub-mm bands is probing radiation emitted by dust grains dispersed throughout the disk. These dust grains intercept stellar radiation and re-emit in the IR or sub-mm with characteristic wavelengths based on the sizes of the grains. This is seen in figure 1.3, as images taken in different wavelengths show that dust grains of different sizes have different radial distributions around the host star. To compare with ALMA observations, one must model the dust structure throughout the disk, which we discuss in section 1.1.3.

1.1.2 Theoretical Models of Disk Structure & Evolution

One of the first models of protoplanetary disks was the so called *Minimum Mass Solar Nebula*, or MMSN model, introduced by Hayashi (1981). The MMSN model aimed to predict the structure of the disk that was a progenitor to the Solar system planets. To construct this disk model, each planet's mass is augmented with enough hydrogen and helium to reach Solar composition, and is then spread out over an annulus centred on the planet's semi-major axis, reaching halfway to neighbouring planets (Armitage, 2010). The static disk model obtained with this method has a column density power law profile of,

$$\Sigma_{mmsn}(r) \simeq 1700 \left(\frac{r}{1\,\mathrm{AU}} \right) \mathrm{g\,cm^{-2}} \, . \tag{1.4}$$

Integrating this profile out to 30 AU results in an enclosed mass of 0.01 $M_{\odot}$, well within the range of disk masses estimated from observations. While this disk model is simplistic, it gives estimations for typical surface densities in disks, $\Sigma(r)$ profiles, and a lower limit of total disk masses.

The MMSN model poses significant constraints on planet formation models. The model suggests that planet formation must be extremely efficient in converting disk material into planets. Additionally, the low densities predicted by this low-mass model make it difficult for planets to accrete and form within a few Myr average disk lifetime. When disk evolution is considered, the mass of the MMSN model will decrease with time which worsens the problem. In order for planets to form in the core accretion scenario, heavier disks that result in higher densities are necessary for planets to have formation timescales within 3 Myr. Typical disk models therefore use initial disk masses of $\simeq 0.1$ $M_\odot$ as a fiducial value. A disk this massive is not unreasonable as observations poorly constrain this parameter. Disks that are significantly more massive ($\gtrsim 0.2$ $M_\odot$) than this fiducial value are typically not used as they are Toomre unstable over the majority of their radii, and provide necessary conditions for planet formation to take place via gravitational instability, which is an alternative scenario to the core accretion model. Together, the MMSN model and Toomre stability considerations provide theoretical constraints on initial disk masses.

While protoplanetary disks are thin in the sense that their radial extent greatly exceeds their vertical extent, they still have finite heights (D'Alessio et al., 1998; Hueso & Guillot, 2005; Chambers, 2009). To determine the vertical extent of a disk, one can consider the disk to be in hydrostatic equilibrium in the vertical direction. In this case, a parcel of gas at a height z above the disk's midplane will experience a force balance between the vertical component of gravity directed towards the disk midplane, and hydrostatic pressure forcing it away. When neglecting the disk's self-gravity, the force balance results in,

$$\frac{1}{\rho}\frac{dP}{dz} = -\frac{GM_* z}{(r^2+z^2)^{3/2}} \ , \tag{1.5}$$

where ρ is the density of disk material and P is the gas pressure. Writing the gas pressure as $P = c_s\rho$ where c_s is the sound speed, and assuming that the disk is vertically isothermal, we obtain the differential equation,

$$c_s^2\frac{d\rho}{dz} \simeq -\frac{GM_* z}{(r^2+z^2)^{3/2}}\rho \ . \tag{1.6}$$

With disk geometry in mind, we can assume $z << r$, and obtain a solution to this equation,

$$\rho(r,z) = \rho_M(r)\exp\left(-\frac{z^2}{2H^2(r)}\right) \ , \tag{1.7}$$

where $\rho_M(r)$ is the density at the disk's midplane at radius r, and $H(r)$ is the disk's scale height,

$$H(r) = \frac{c_s(r)}{\Omega(r)} = \sqrt{\frac{k_B T r^3}{\mu m_H G M_*}} \ , \tag{1.8}$$

where $\Omega(r)$ is the Keplerian angular frequency. This equation can be used to estimate disk vertical extents. Typical disk scale heights are 0.5-1 AU, with scale heights becoming larger farther out in the disk. These are indeed small compared to the disk radial extents $\sim$ 100-200 AU.

SED fitting of disks find that the temperatures at large radii are larger than expected for a geometrically flat disk (D'Alessio et al., 1998; Roberge, 2010). This suggests that disks should have flared profiles, which allows outer regions to intercept more radiation from their host stars. In other words, the disk's vertical extent should become larger farther out in the disk. Understanding disk flaring is important for modelling the amount of energy they receive from their host stars which in turn determines their midplane temperature profiles. The disk's aspect ratio $h \equiv H/r$ determines the disk's shape, and h profiles that increase with r lead to flaring. From equation 1.8 we find that,

$$h \sim r^{-\beta/2+1/2} \, , \tag{1.9}$$

where $T(r) \sim r^{-\beta}$. From this, we find that disks will have flared profiles when their temperatures vary as $T(r) \sim r^{-1}$ or shallower.

Throughout the duration of the protoplanetary disk's lifetime, the protostar will continue to accrete material through the disk at a rate of roughly $10^{-8} - 10^{-7}$ $\mathrm{M}_{\odot}$/year (Chambers, 2009). The accretion process will result in some material losing angular momentum, and in order to conserve angular momentum throughout the disk, other material must gain angular momentum. Globally, this results in the radial extent of the disk increasing with time as some material gains angular momentum and moves outwards. Throughout the disk, then, material must somehow exchange angular momentum with material at neighbouring radii in order to explain the process of accretion.

Disk material can exert viscous torques on material orbiting at neighbouring radii, and provide a means of redistributing angular momentum throughout the disk. The molecular viscosity, however, is too small by several orders of magnitude to reproduce observed accretion rates. The mechanism that generates the necessarily large viscosities throughout disks is still debated. Notable proposed methods are turbulence generated via the magnetorotational instability (Balbus & Hawley, 1991), disk winds (Pudritz & Norman, 1986; Bai & Stone, 2013; Gressel et al., 2015), and the zombie vortex instability (Mohanty, Ercolano & Turner, 2013; Marcus et al., 2015). The disk viscosity, ν, can be written in terms of an α parameter (Shakura & Sunyaev, 1973),

$$\nu = \alpha c_s H \ , \tag{1.10}$$

with α corresponding to the efficiency of angular momentum transport methods in the disk. When more than one process is acting, α will be a summation the effective α's corresponding to each process. To obtain viscosities necessary to explain observed accretion rates, α is typically in the range of 0.001-0.01 (Hueso & Guillot, 2005).

The steady-state angular momentum equation,

$$\frac{\partial \Sigma}{\partial t} = \frac{3}{r}\frac{\partial}{\partial r}\left[r^{1/2}\frac{\partial}{\partial r}\left(r^{1/2}\nu\Sigma\right)\right] \ , \tag{1.11}$$

describes the disk's time-dependent viscous evolution. It can be solved to obtain time-dependent radial surface density $\Sigma(r)$ profiles that account for the efficiency of angular momentum transport throughout the disk. As shown in Lynden Bell & Pringle (1974), self-similar solutions to this equation can be obtained for alpha disk models, where ν is parameterized as in equation 1.10. One of the key results of these solutions is their relation of the disk accretion rate, $\dot{M}$, to the viscosity and column density through,

$$\dot{M} = 3\pi\nu\Sigma \ . \tag{1.12}$$

We note that due to viscous evolution, the disk $\dot{M}$ will itself be a decreasing function of time, with exact time-dependency depending on the disk model used. From the disk evolution equation, one can derive an associated characteristic disk evolution timescale similar to a diffusion timescale. This timescale, known as the viscous timescale,

$$\tau_{vis} \simeq \frac{r^2}{\nu} \ , \tag{1.13}$$

corresponds to the timescale over which disk viscosity will smooth out surface density gradients. It is the typical timescale used to characterize disk evolution processes and is of the order of 1 Myr for typical disk parameters.

The temperature profile along the disk's midplane, $T(r)$, is a necessary output of disk models as it sets the thermodynamic, and therefore chemical environment where planet formation takes place.

To calculate the disk's temperature structure, one can assume that the disk is in thermodynamic equilibrium as the timescale to reach equilibrium is often much shorter than the viscous timescale (Armitage, 2010). Determining $T(r)$ then becomes a problem of balancing heating and radiative cooling. There are two heating mechanisms in the disk; one is viscous heating generated by accretion through the disk concentrated towards the disk midplane, and the second is due to the disk intercepting radiation from the star. Viscous heating will dominate the inner regions of the disk (typically $\lesssim$ 10 AU) where the densities are highest, while radiation dominates the outer regions of the disk due to the disk's flared profile allowing it to intercept more radiation at large orbital radii.

Working in the viscous regime, we want to combine equations describing viscous heating with the disk's radiative cooling to calculate the temperature structure. We assume that radiative cooling happens in the vertical direction, so this calculation takes into account the disk's vertical thermal structure. To calculate this thermal structure in the disk's vertical direction z, one can combine an equation that describes the vertical flux variation (Armitage, 2010),

$$\frac{dF_z}{dz} = \frac{9}{4}\rho\nu\Omega^2 \ , \tag{1.14}$$

with a radiative diffusion equation describing the variation in disk temperature with flux in an optically thick ($\tau >> 1$) medium,

$$\frac{dT}{dz} = -\frac{3\kappa\rho}{16\sigma T^3}F_z \ . \tag{1.15}$$

Integrating equation 1.14 results in,

$$\begin{aligned} \int_0^z \frac{dF}{dz'}dz' &= \frac{9}{4}\nu\Omega^2 \int_0^z \rho(z')dz' \\ F_z &= \frac{9}{4}\nu\Omega^2 \left(\frac{\Sigma}{2}\right) \\ \sigma T_{eff}^4 &= \frac{9}{8}\nu\Sigma\Omega^2 \ , \end{aligned} \tag{1.16}$$

where we assume that the viscous energy is dissipated at the disk midplane where the density is largest, resulting in $F_z = \sigma T_{eff}^4$. Using this assumption, and integrating equation 1.15, we can derive the relation,

$$\frac{T^4}{T_{eff}^4} \simeq \frac{3}{4}\tau \ , \tag{1.17}$$

where T corresponds to the disk's midplane temperature, and we assume that $T^4 >> T_{eff}^4$ is true for an optically thick disk. These results allow us to calculate the disk's midplane temperature in the viscous regime given the disk's $\Sigma(r)$ profile and $\nu(r)$ profile. The difficulty with this calculation is that $\nu = \alpha c_s H$ depends on the midplane temperature through its H and c_s dependencies.

Thermodynamic equilibrium in the region of the disk heated via irradiation implies that the flux received from the star heating the disk is balanced by the flux radiated from the disk allowing it to cool (Chiang & Goldreich, 1997). This results in a vertical $F_z = 0$, which in turn implies that $T = T_{eff}$ in the irradiated region of the disk. We note that the stellar radiation intercepted by the disk is done so by dust grains, which re-emit the radiation in the infrared. The flux balance used to derive this result rests on the assumption that the disk is optically thin in IR wavelengths. More detailed models that do not rely on this assumption find that the disk's midplane and effective temperatures are indeed different (Hasegawa & Pudritz, 2010).

Accounting only for the disk's viscous evolution in equation 1.11 results in disk lifetimes that are inconsistent with observations. Viscous evolution alone is too slow to explain 3 Myr-lived disks and viscous disk models can allow disks to survive for longer than 10 Myr, which is problematic. In order to have viscous disk lifetimes consistent with observations, planet formation models would abruptly set the disk surface density to zero everywhere at the desired lifetime. While this is unphysical, it is a necessary feature of models including only viscous evolution in order to terminate planet accretion and migration at observed disk lifetimes.

The solution to this problem is the fact that photoevaporation can sharply truncate disk evolution (Pascucci & Sterzik, 2009). In this process, high energy radiation emitted by the young star couples to disk material in the photosphere and constantly drives away disk material. For early stages of disk evolution, this process is slow and produces mass loss rates that are negligible compared to the disk's viscous accretion. At more evolved stages, however, the mass loss rate due to photoevaporation can become comparable to the disk's $\dot{M}$. At this point, photoevaporation will quickly blast away the disk material over 10^4 year timescales (Pascucci & Sterzik, 2009; Owen et al., 2011). Photoevaporation is a physical mechanism of disk dispersal, and when included in disk evolution models, can reproduce observed disk lifetimes (Hasegawa & Pudritz, 2013). The effects of photoevaporation can be included in the disk evolution equation by modifying equation 1.11 (Owen et al., 2011),

$$\frac{\partial \Sigma}{\partial t} = \frac{3}{r}\frac{\partial}{\partial r}\left[r^{1/2}\frac{\partial}{\partial r}\left(r^{1/2}\nu\Sigma\right)\right] + \dot{\Sigma}_{pe} \ , \tag{1.18}$$

where $\dot{\Sigma}_{pe}$ represents the rate of disk depletion through photoevaporation. Simple models take this quantity to be a constant throughout the duration of the disk's existence, while more complicated ones scale $\dot{\Sigma}_{pe}$ with the stellar accretion rate. This quantity is often parameterized in some manner that allows the strength of photoevaporation to be set in accordance with desired disk lifetimes in mind.

Currently, there are several different kinds of disk models in the literature, each with different areas of applications. The disk model used in this thesis is largely developed in Chambers (2009) and is a semi-analytic model. Semi-analytic disk models make several assumptions that simplify calculations while still reproducing the majority of observed or simulated disk features. For example, semi-analytic models often assume constant α parameters throughout the disk resulting in a radially-independent disk $\dot{M}$. Additionally, these models often use simple disk opacity profiles. Semi-analytic disk models are useful as they allow for fast calculation of disk structure and evolution that can then be used in detailed and time-consuming computation of disk chemistry or planet formation.

A second class of disk models are static models that do not compute the disk's evolution. Rather, they focus on detailed modelling of snapshots of disk structure. For example, the series of models presented in D'Alessio et al. (1998, 1999, 2001) produce detailed disk surface density and temperature structures dependent on an overall disk $\dot{M}$ that is used as an input parameter to the calculations. While avoiding a model of how $\dot{M}$ evolves with time, these models are useful as the disk snapshots provided can be compared with observations by calculating SEDs from computed disk structure and fitting to observations.

Lastly, a third type of disk model utilizes detailed numerical and computational methods. Numerical disk models include the effects of hydrodynamics, radiative transfer, and in some cases magnetohydrodynamics, on protoplanetary disk structure and evolution. These models often use detailed disk opacity (Stepinski, 1998) and α profiles (Gressel et al., 2015) that vary throughout the disk. Often these profiles are informed via disk chemistry models, discussed in section 1.2. Detailed numerical models of disks are useful as they can reveal different fluid or MHD instabilities that can be present in accretion disks, while providing detailed calculations of their structure. These models are often limited by the amount of time it takes to compute snapshots of disk evolution, as well as their use of sub-grid models which are necessary due to the large range of relevant scales involved in protoplanetary disk physics.

1.1.3 Dust Dynamics & Evolution

In order to compare theoretical disk models with the detailed structures revealed in ALMA IR/sub-mm observations, one must focus on modelling dust distributions throughout the disk. For example, the ring-like structures shown in figure 1.3 do not suggest that gaps are fully cleared out at these radii. They rather tell us that dust grains (with size corresponding to the image's wavelength) are not present at these locations in the disk. Theoretical models have attempted to explain the origin of the gaps in the HL Tau disk with rapid grain growth (Zhang et al., 2015), or planet formation (Akiyama et al., 2016), both of which deplete local regions in the disk of small grains detectable in the (sub)mm wavelength band.

Dust grains dispersed throughout the protoplanetary disk represent the smallest solids out of which planets will form in the core accretion scenario. These μm grains are predicted to condense out of the gaseous nebula on short timescales, and provide the solid material that will make up planetary interiors after the planet formation process has completed. Simple disk models assume that the density of dust grains is 1 % of the gas density everywhere throughout the disk, but much more detailed models of the distribution of dust grains are possible by considering the various physical mechanisms governing their dynamics. This section will discuss these important processes, as well as those that lead to growth of these dust grains. Modelling of dust dynamics and evolution is important to consider both as an early stage in the core accretion scenario, and also for comparisons with observations of disks via dust emission. We note that this thesis does not model the physics of dust evolution, but we recognize this as an important and current problem in the astrophysics of disks and planet formation.

The growth of dust grains takes place upon collisions via a process referred to as coagulation. Collisions of the small, μm-sized dust grains throughout the disk often lead to growth, but as grains become larger ($\sim$ cm-sized or larger), they are more prone to fragmentation upon collision. Collisions leading to fragmentation replenish the disk with small grains that are being depleted by coagulation. Modelling the simultaneous growth and fragmentation of grains within a disk will lead to a distribution of grain sizes, with the functional form depending on how efficiently grain growth happens. Since larger grains are more prone to fragmentation, the grain size distribution will have a larger amount of small grains than large ones. Most models of grain growth predict that 10 cm-sized grains are the largest ones to form via coagulation (Birnstiel, Klahr, & Ercolano, 2012; Testi et al., 2014).

The relative velocities between colliding grains is a key quantity in determining whether a collision will result in growth or fragmentation, as low velocity impacts favour the grains sticking together, and high velocity impacts favouring fragmentation. Individual grains will have different fragmentation energy barriers depending on the grain structure and composition. Grains outside the disk's snow line will have ice frozen onto their surfaces, resulting in the grains being "sticky", and allowing them to have a higher energy barrier for fragmentation (Testi et al., 2014). Conversely, dry grains inside the disk's snow line have a lower fragmentation barrier, leading to collisions being more likely to fragment dry grains.

The vertical distribution of dust grains in the disk is governed by the competing processes of gravity, which forces grains towards the disk's midplane, and disk turbulence, which stirs up dust grains, forcing them away from the disk's midplane. Dust grains of each size acted on by these two forces will reach an equilibrium, achieving a vertical distribution following a Gaussian profile centred on the disk's midplane (Armitage, 2010). The scale height of this Gaussian depends on the sizes of the grains, and the effect turbulence has relative to the strength of gravity. Large grains will tend to lie closer to the disk's midplane, having a smaller scale height, while small grains are more prone to being stirred up by turbulence and will have a larger scale height. The disk will then be optically thick to shorter wavelength IR radiation from small grains as they are spread over the majority of the disk's vertical extent, and observing at these wavelengths will thus probe dust higher in the disk. Observations at longer wavelengths corresponding to larger grains will conversely probe closer to the disk's midplane due to these grains having smaller scale heights (Testi et al., 2014).

The radial motion of dust in the disk is governed by the drag forces dust grains experience throughout their orbits. Since the gas in the protoplanetary disk is pressure supported, it moves at a slightly sub-Keplerian rotation rate. The solids, conversely, do not have additional pressure support, so they orbit at the Keplerian frequency, and thus experience a drag force from the gas. The drag force provides negligible effects on km-sized or larger objects. However, the drag force on smaller dust particles present in abundance throughout the disk will be an important effect to consider while modelling their dynamics. We can distinguish two different drag regimes based on the size of the dust particles and the local density of gas. For dust grains with radii $R < 9\lambda/4$, where λ is the mean free path of gas molecules, the grains undergo Epstein drag (Chambers, 2010), with drag force,

$$F_{drag} = -\left(\frac{\rho_{gas} c_s}{\rho R}\right) M(v - v_{gas}) \ , \tag{1.19}$$

where ρ_{gas} and c_s are the density and sound speed of the gas, ρ and M are the density and mass of the solid dust grain, and v and v_{gas} are the velocity of the grain and gas, respectively. In the Epstein drag regime, dust particles are expected to be strongly coupled to, and thus tracers of, the flow of gas in the disk. Epstein drag is expected to be the drag regime for particles with sizes up to roughly 1 cm for typical disk conditions. In this drag regime, the dust particles are small enough that the drag force on them are a consequence of many collisions with individual gas molecules

The second drag regime is the so-called Stokes drag regime. Grains with radii $R > 9\lambda/4$ are governed by Stokes drag, and in this regime the solids are large enough that they experience a fluid-like drag force from the gas. In the Stokes regime, the drag force is,

$$F_{drag} = -\frac{3C_D \rho_{gas}}{8\rho R} M(v - v_{gas})|v - v_{gas}| \ . \tag{1.20}$$

C_D is a drag coefficient, which depends on the Reynolds number Re$= 2R|v - v_{gas}|/\nu_m$ where ν_m is the molecular viscosity. The drag coefficient has the form,

$$\begin{aligned} C_D &\simeq 24\mathrm{Re}^{-1} && \mathrm{Re} < 1 \\ &\simeq 24\mathrm{Re}^{-0.6} && 1 < \mathrm{Re} < 800 \ . \\ &\simeq 0.44 && \mathrm{Re} > 800 \end{aligned} \tag{1.21}$$

The Stokes drag is expected the be strongest for solids roughly 1 metre in size. Objects 100 metres or larger have negligible Stokes drags, while the Stokes drag on particles 1-10 cm in size provides a transition between the Epstein (gas coupled) and Stokes regime. The process of dust trapping in disks can halt the inward radial drift of large dust particles in the Stokes regime, arising due to pressure maxima in disks. Dust trapping is likely an important effect when considering planetesimal formation (see section 1.3.1).

Current simulations of dust evolution that consider radial drift, vertical settling, growth and fragmentation are able to compute radial density distributions of grains over all sizes from μm up to 10 cm. The model presented in Birnstiel et al. (2012) finds that efficient grain growth in the outer disk, followed by rapid inward radial drift depletes the outer disk of large grains. Meanwhile, grain growth in the inner disk is limited by fragmentation of dry dust grains. This calculation showed fragmentation and radial drift limits throughout the disk, setting physical upper limits to the sizes of grains at all radii. These distributions, however, are sensitive to the sticking efficiencies and resulting fragmentation barriers used to characterize dust grains inside and outside the ice line.

1.2 Disk Chemistry

In order to track materials accreted onto planets throughout their formation, one must first model the chemical structure of the planets' natal disk. In the last section, we outlined a method of determining the disk's midplane temperature and pressure profiles throughout its evolution. These quantities set the thermodynamic conditions for chemistry throughout the disk. While disk structure provides initial conditions for chemistry calculations, disk chemistry can in turn inform models of disk structure, as the disk's opacity profile is sensitive to the composition of solids throughout the disk. Disk chemistry models are not only essential for calculating compositions of planets during their formation, but also for tracing disk structure through comparisons with observations. Abundances of various solids and gases throughout the disk trace different temperature regimes, and observed chemical signatures can indicate temperatures in disks. For example, water undergoes a phase transition at roughly 170 K in disks, and the location is referred to as the snow line. Observing signatures indicative of this phase transition will indicate the location in the disk with this temperature and can inform disk models. Disk chemistry is a key component of the model presented in this thesis, and we refer the reader to section 2.2.2 for its detailed description.

1.2.1 Disk Ionization

As was discussed in the previous section, the method by which angular momentum is transported throughout disks is somewhat uncertain. One possible method is turbulence driven by the magnetorotational instability (MRI), which relies on the disk being sufficiently ionized in order for there to be coupling between disk material and an intersecting magnetic field. Coupling of a magnetic field to the disk gas, combined with the $\Omega(r) \sim r^{-3/2}$ profile in the disk which decreases with radius, gives rise to the MRI - a linear MHD instability. One must then calculate the disk's ionization structure in order to determine the activity of the MRI and its ability to transport angular momentum. The regions of the disk that are insufficiently ionized for MRI activity are considered as MRI-dead regions of the disk. To calculate disk ionization structure, an equilibrium state between sources of ionization and recombination can be considered.

Disk material is ionized by high energy photons penetrating the disk. X-rays, for example, that result from accretion onto the protostar, are one such source of ionizing radiation. If the disk is within a star forming cluster, X-rays from other members of the cluster could be another ionizing source. Lastly, high-energy interstellar cosmic rays are another candidate for ionizing radiation important for disks. The regions of the disk with highest column densities will be the least susceptible to ionizing radiation penetrating down to the disk's midplane. Since the disk $\Sigma(r) \sim r^{-3/2}$ roughly, one can expect the inner regions of the disk not to be penetrated by this radiation, while outer regions will have radiation reaching the disk midplane and thus will be more ionized. Thus, the MRI-dead region of the disk, or *dead zone*, will be located in the inner regions of the disk near the disk midplane. Most ionization models calculate the dead zone to be within 10-50 AU. Meanwhile, the outer region of the disk, and upper layers of the inner disk will be MRI-active as these are regions with low optical depths to ionizing radiation.

A crucial part of disk ionization models, and the portion that disk chemistry informs, is recombination reactions. Semi-analytic models can model these recombinations using simple temperature-dependent reaction rate equations (Matsumura & Pudritz, 2003). Another, more detailed method involves inputting recombination reactions in a disk chemistry network, and calculating recombination rates as a function of local disk properties. This is the method employed by non-equilibrium chemistry models that include radiative transfer in their calculations (Cleeves, Adams & Bergin, 2013; Cridland, Pudritz & Alessi, 2016). We note that the ionization model used in this thesis uses the first method, and we direct the reader to section 2.2.3 for a detailed description of our disk ionization model.

1.2.2 Equilibrium Chemistry

One method of modelling disk chemistry structure is through Gibbs free energy minimization. The thermodynamic Gibbs free energy is,

$$G = H - TS \; , \tag{1.22}$$

where H is the enthalpy, T is the system's temperature, and S is the entropy. For a system being composed of N species, the total Gibbs free energy is,

$$G_T = \sum_{i=1}^{N} X_i G_i = \sum_{i=1}^{N} X_i (G_i^0 + RT \ln X_i) \ , \tag{1.23}$$

where X_i, G_i, and G_i^0 are the mole fraction, Gibbs free energy, and Gibbs free energy of formation of species i, respectively.

In order to determine the equilibrium state, one first must specify the elemental abundances throughout the chemical system (for instance, Solar abundances). Then, the set of X_i (corresponding to amounts of disk gaseous and solid materials) which minimize equation 1.23 for a chemical system defined by temperature T and pressure P can be calculated. An additional constraint based on mass considerations is,

$$\sum_{i=1}^{N} a_{ij} x_i = b_j \quad (j = 1, 2, \ldots, m), \tag{1.24}$$

where m is the number of elements in the chemical system, x_i is the total number of moles of species i, a_{ij} is the number of atoms of element j contained in species i, and b_j is the total number of moles of element j. The total number of moles, x_i, and the mole fraction, X_i of species i are related by $x_i = X_i \times 100\,\mathrm{kmol}$.

Gibbs free energy minimization is a useful method of calculating disk chemistry, however it relies on the assumption that the chemical equilibrium timescale everywhere throughout the disk be smaller than the disk's viscous timescale. This physically means that disk material needs to come to chemical equilibrium before viscous evolution changes the temperature and pressure of the material. Laboratory experiments showed that solids condense out of gas under disk thermodynamic conditions on short timescales of $\sim$ 1 hour, much less than the disk's viscous timescale (Toppani et al., 2006). This indicates that equilibrium chemistry is an accurate method of modelling the solid chemistry structure throughout the disk. Conversely, the equilibrium timescale for gases can be comparable to or longer than the viscous timescale, especially in outer regions of the disk beyond 10 AU. In the case of gases, then, non-equilibrium chemistry is important for determining abundances of gaseous materials.

As one of the goals in this thesis is to determine the composition of super Earths, planets composed primarily of solids, equilibrium chemistry is used to calculate the disk's chemical structure. Another work that has calculated detailed solid chemistry throughout a disk of Solar abundance is Pignatale et al. (2011). Other groups have done similar disk chemistry calculations in order to track planet compositions during N-body simulations with the goal of producing terrestrial planets similar to those seen in the Solar system (Bond et al., 2010; Elser et al., 2012; Moriarty et al., 2014).

1.2.3 Non-Equilibrium Chemistry

Equilibrium chemistry calculations are limited in their ability to predict abundances of gases in regions of the disk where the chemical timescales are longer than the disk's viscous time. In order to determine chemical abundances in these regions of the disk, one must use non-equilibrium chemistry. Such codes use detailed chemical networks, and include non-equilibrium effects such as photon-driven reactions, ion chemistry, and grain surface reactions. In the case of photon-chemistry, the radiation field throughout the disk needs to be computed by radiative transfer calculations. Photon-driven reactions include photodissociation and X-ray ionization which contributes to the local electron fraction in the disc. The catalyzing effects of grain surfaces are another important non-equilibrium effect, as the freeze out of volatiles on grain surfaces can result in higher ice abundances than equilibrium models predict. Non-equilibrium chemistry models can be extremely detailed and are beyond the scope of this thesis. We refer the reader to Cleeves et al. (2013) and Cridland, Pudritz & Alessi (2016) for descriptions of non-equilibrium chemistry codes and resulting disk and planet atmosphere compositions.

1.3 Core Accretion Model

The core accretion model is a bottom-up model describing the process of Jovian planet formation within a protoplanetary disk[2]. In a global sense, it provides a means of explaining all growth stages between micrometer-sized dust grains throughout the disk into massive planets with radii $\sim 10^5 - 10^6$ km. Thus, the core accretion formation scenario aims to model growth over 15 orders of magnitude in size. This entire process must be completed prior to the disk lifetime of ~ 3 Myr, as once this material is dissipated a growing planet will no longer have any material to accrete. We therefore have an understanding of the timeline and size range constraining this problem. Additionally, we have observational constraints of the initial condition of this process - the protoplanetary disk, as well

[2]An alternative scenario of planet formation, known as *gravitational instability*, predicts planets to form in a "top-down" manner via direct gravitational collapse out of the disk.

as the end result of planet formation in the form of distributions of exoplanets on the mass-period and mass-radius diagrams. However, we currently have limited observational evidence to further constrain planet formation, and we rely on detailed models for understanding of how planets form in the core accretion scenario. Current and future ALMA observations of dust structure in disks will provide insights on the planet formation process, as dust distributions can infer the presence of forming planets.

Qualitatively, the core accretion model begins with the coagulation of μm dust grains into km-sized planetesimals, which gravitationally interact and collide via N-body processes forming large planetary cores with masses ~ 0.01 $M_\oplus$ and sizes of roughly 10 km. These large planetary cores continue to accrete smaller planetesimals before accreting gas from the disk in the form of an atmosphere, reaching masses comparable to that of Jupiter. As this model covers such a broad range of size scales, it naturally requires an immense amount of physics in order to explain different growth stages. However, most models within the core accretion framework only concern themselves with a subset of these process as opposed to the global picture. Most models can be broadly classified into those describing the growth of dust into planetesimals, and those modelling the N-body growth of planetesimals into planetary cores and subsequent gas accretion. The planet formation model presented in this thesis covers the latter. We refer the reader to section 2.2.4 for a detailed description of this model.

Accretion rates onto planets are sensitive to the density of surrounding disk material. Models of planet formation are therefore sensitive to the mass of the disk they are forming within. Early models of planet formation considered a minimum mass Solar nebular (MMSN) model with a disk mass of ~ 0.01 $M_\odot$ (Pollack et al., 1996; Crida, 2009) which ignored disk evolution. Their calculated formation timescales were therefore large- close to 10^7 years which is expected to be larger than the lifetime of disks. These early models informed us that more massive disks were necessary to obtain shorter formation times. When including the effects of disk evolution, larger initial disk masses such as 0.1 $M_\odot$ still resulted in surface densities consistent with observations after ~ 1 Myr of disk evolution. This tells us that the large initial disk masses necessary to form Jovian planets within 3 Myr are not unreasonable. Throughout this section, the timescales provided for different growth regimes will correspond to a disk with an initial mass of 0.1 $M_\odot$, considered a fiducial disk mass in the model presented in this thesis.

Even with a large range of size scales covered in the core accretion framework, there are only several key ideas that highlight the most important physical processes within each growth stage. In the following sections, we provide an overview of these key processes. We arrange the section by discussing core accretion model pieces in order of increasing size scale. We first discuss processes affecting growth of dust into planetesimals in section 1.3.1. Then, in section 1.3.2 we discuss the growth of a Jovian planet's core. Lastly, we cover gas accretion in section 1.3.3.

1.3.1 Planetesimal Formation

The growth of 1-10 cm grains, the largest grains that form when considering coagulation and fragmentation, up to km-sized planetesimals is an unresolved problem. This poses a difficulty for the core accretion model quite early on. Further collision of ~ 10 cm sized pebbles often results in fragmentation as opposed to growth as the largest pebbles formed by coagulation are held together loosely (Chambers, 2010). An additional problem arises when one considers the gas drag on meter-sized boulders in the disk. The stokes drag on solids of roughly this size experience a strong headwind and are the most prone to radial drift. Boulders of this size will spiral into the star within 100 years, which drastically constrains the growth timescale solids in this size range have to further grow into planetesimals (Armitage, 2010). This short drift timescale is known as the meter barrier problem, owing to the theoretical difficulties it poses when considering growth of solid objects in the disk beyond 1 metre. A plausible model of the formation of km-sized planetesimals must therefore either provide a means to grow planetesimals rapidly, or provide a way of counteracting rapid inward radial drift of solids near the 1 meter size range.

One of the earliest models of planetesimal formation that aimed to simultaneously solve the metre barrier problem and the problems facing grain growth beyond the 10 cm size scale was the *Goldreich Ward Mechanism* (Goldreich & Ward, 1973). This model provides the basis of many modern theories of planetesimal formation. It suggests that settling of dust into an extremely thin layer along the disk's midplane would result in a gravitational instability within this solid particle disk. The gravitational instability would then result in rapid growth of solids up to the km-size range. Due to the rapid nature of growth in the instability, the grain growth problem is avoided, and the metre-barrier radial drift problem is overcome. The problem with this model, however, is that it ignores the counteractive role disk turbulence has on dust settling. In the majority of disk models, turbulence would be too strong to allow for grains to settle into a gravitationally-unstable disk that the Goldreich-Ward mechanism relies on. While this mechanism is unlikely to be an adequate model of planetesimal formation, it does highlight that local overdensities of solids in the disk can provide proper conditions for planetesimal formation.

One of the most promising models of planetesimal formation within turbulent disks relies on a process known as dust trapping. Dust will radially drift towards pressure maxima in the disk. Radial drift will cause dust at both larger and smaller radii to drift towards a local pressure maxima, and collisional growth within this dust trap can be enhanced (Armitage, 2010). Local enhancements in the dust-to-gas ratio can lead to an instability known as the streaming instability (Youdin & Goodman, 2005). The nature of this instability acts to further enhance the dust to gas ratio at the dust trap, and can lead to the solids at the over-density becoming gravitationally unstable, leading to a greatly enhanced growth as was the case in the Goldreich-Ward mechanism. Numerical models of planetesimal growth via the streaming instability predict the formation of planetesimals up to 100 km in size (Johansen et al., 2007; Birnstiel et al., 2010). However, the results of these models are unclear due to uncertainties present.

While the mechanism by which planetesimals form remain unclear, they are a necessary step in the process of core accretion. The phase of planetesimal formation is expected to be short-lived, with many planetesimals populating the disk at only $\sim 10^4$ years into disk evolution (Armitage, 2010). At the end of this step in the core accretion model, we expect a radial distribution of planetesimals throughout the disk that has a negative radial power law somewhat following that of the gas. Thus, planetesimals will preferentially populate inner regions of the disk as opposed to regions with large orbital radii. These criteria will provide the initial conditions to the next phase of the core accretion model, which aims to describe the growth of kilometre-sized planetesimals via N-body processes.

1.3.2 Planetary Core Growth

During N-body interactions between planetesimals, the cross-sectional radius over which a planetesimal will accrete is enhanced by a gravitational focusing factor,

$$F_g^2 = 1 + \frac{v_{esc}^2}{v_{rel}^2} \ , \tag{1.25}$$

where v_{esc} is the escape velocity from the planetesimal's surface, and v_{rel} is the relative velocity between two interacting planetesimals. Thus, a growing planetesimal will accrete material throughout the disk with an enhanced cross-section $\pi R_p^2 F_g^2$. This enhancement corresponds to the region in the disk over which planetesimals are deflected via gravitational interactions. Within a planetesimal disk with an isotropic velocity dispersion, Lissauer (1993) obtained the following accretion rate onto a planetesimal using this gravitational focusing term,

$$\frac{dM}{dt} = \frac{\sqrt{3}}{2}\Sigma_p \Omega \pi R_p^2 \left(1 + \frac{v_{esc}^2}{v_{rel}^2}\right) \ , \tag{1.26}$$

where Σ_p is the surface density of disk material at the planet's location, and Ω is the planet's orbital frequency. We note that this equation assumes that all material swept up by the planetesimal is accreted, and the amount of escaping fragments is negligible. We can now define two growth regimes dependent on the mass of the planetesimal in question.

The first regime corresponds to planetesimals that are sufficiently low mass so as to not affect the v_{rel} of surrounding planetesimals substantially. In this case, using $v_{esc}^2 \sim M_p/R_p$ and $R_p \sim M_p^{1/3}$, we can derive the growth rate for planetesimals as (Chambers, 2010),

$$\frac{dM}{dt} \propto \Sigma_p M_p^{4/3} \ . \tag{1.27}$$

This translates into a growth timescale of,

$$t_{grow} \sim \frac{M_p}{\dot{M}_p} \simeq M_p^{-1/3} \ . \tag{1.28}$$

This tells us that larger planetesimals will grow faster than smaller ones. This is therefore a runaway or divergent process. Integrating this process over 10^5 years in a disk populated with planetesimals will result in a relatively smaller number of the largest planetesimals dominating various regions of the disk. These massive planetesimals that result from runaway growth are referred to as planetary cores, or *oligarchs*, owing to their gravitational dominance over a local region of the disk. The masses of these planetary cores are roughly $10^{-3} - 10^{-2}$ $M_\oplus$.

Once planetesimals reach this mass, the second growth regime applies which is called Oligarchic growth. High mass planetary cores will affect the v_{rel} of surrounding, lower mass planetesimals, resulting in $v_{rel} \propto M_p^{1/3}$ (Chambers, 2010). The resulting accretion rate in this regime is,

$$\frac{dM}{dt} \propto \Sigma_p M_p^{2/3} \ , \tag{1.29}$$

leading to a growth timescale of,

$$t_{grow} \propto M_p^{1/3} \; . \tag{1.30}$$

In this regime, higher mass planetary cores take longer to accrete than lower mass ones. However, planetary cores still accrete faster than planetesimals due to their larger gravitational focusing factors. During this growth phase, dynamical friction will restrict the planetary core to a circular, coplanar orbit whereby it accretes planetesimals within a regime defined by the planet's Hill radius,

$$r_H = \left(\frac{M_p}{3M_*}\right)^{1/3} a_p \; . \tag{1.31}$$

This radius defines the region of the disk where the planetary core's gravitational field dominates over than of the host star. Planetary cores often maintain separations of roughly 10 Hill radii during this growth phase in the core accretion model.

The Oligarchic growth phase of planet formation is notably the first growth regime, or initial phase, in the planet formation model presented in this thesis. This process can allow the planetary core to grow from 0.01 $M_\oplus$ up to a few $M_\oplus$ within several 10^5 years - 1 Myr (ie. on a shorter timescale than the disk lifetime). However, the accretion rates during this stage are sensitive to the surface densities of planetesimals at the planetary core's location in the disk. Since the surface densities of planetesimals decrease with radius, the growth timescale will be much quicker close to the star than at large orbital radii. Therefore, the accretion rates necessary to form a 3 $M_\oplus$ planetary core can only be achieved within 5-10 AU in most disk models. Oligarchic growth outside of 10 AU can take longer by a factor of 10 or more. In this case, oligarchic growth could take up to a few Myr to complete, which is comparable to the disk lifetime. This is problematic, as core formation at such a slow rate will not give planets a chance to accrete gases prior to disk dispersal. Therefore, oligarchic growth is a plausible core formation mechanism within $\sim$ 10 AU in most disk models.

An additional enhancement of the planetary core's cross-sectional radius comes from gas drag. As a planetary core forms, there will be a small amount of gas gravitationally bound within the planet's Hill sphere that can act to damp the motion of planetesimals traversing through this region (D'Angelo et al., 2014). The drag produced by the core's atmosphere can remove enough energy so as to accrete planetesimals that would otherwise have too high of a relative velocity to be gravitationally bound. The effect is dependent on the size of the impacting planetesimal in question as well as the atmosphere model used. Generally, gas drag provided by a planetary core's atmosphere will have a small effect on planetesimals, providing only a small enhancement to the planetary core's effective cross-section.

The abundant amount of dust throughout the disk has lead to an alternative mechanism describing planetary core formation, known as *pebble accretion*, to be posed. Pebbles are 1-10 cm sized solids present throughout the disk, and represent the largest sizes of solids that can be formed via dust coagulation without the aid of dust traps or streaming instabilities. In contrast to planetesimals, the effect of gas drag on pebbles traversing through the planet's envelope will be substantial. Gas drag can provide a means of increasing a planetary core's effective cross-section greatly when accreting pebbles, and this can provide the necessary accretion rates to allow planetary cores to form within several 10^5 years (Bitsch et al., 2015). The advantage of pebble accretion models is that they are less sensitive to the planetary core's orbital radius, since pebbles are expected to be present in abundance everywhere throughout the disk, in contrast to planetesimals that preferentially populate the inner regions of the disk. Pebble accretion models have been shown to produce planetary cores with masses $\sim$ 1-5 $M_\oplus$ in disks with masses as low as 0.01 $M_\odot$, similar to a MMSN model (Ormel & Klahr, 2010; Bitsch et al., 2015). These recent results suggest that pebble accretion can provide an alternate core formation scenario and rule out the oligarchic growth phase of planet formation.

The end phase of oligarchic growth takes place when gas accretion becomes more efficient than planetesimal accretion. As is discussed in the next section, the gaseous envelope surrounding a planetary core is in hydrostatic balance, with energy provided by impacting planetesimals. Once planetesimal accretion becomes sufficiently slow, the energy that is necessary to maintain the pressure support of this envelope will no longer be supplied, and surrounding gas from the disk will flow onto the planet. Ikoma et al. (2000) found the following critical mass that represents the upper limit to the oligarchic growth regime,

$$M_{crit} \sim 7 \left(\frac{\dot{M}_{core}}{10^{-7} M_\oplus \, \mathrm{yr}^{-1}} \right)^q \left(\frac{\kappa_R}{1\,\mathrm{cm}^2\,\mathrm{g}^{-1}} \right)^s M_\oplus \; , \tag{1.32}$$

where $q \simeq 1.4$ and $s \simeq 1$ are parameters. For planets more massive than M_{crit}, gas accretion will govern their formation, which is discussed in the next section.

1.3.3 Gas Accretion

The final phase of the core accretion model is the phase of gas accretion. This stage of planet formation corresponds to planets larger than ~ 3 $M_\oplus$, and can provide a means of growth up to the mass of Jupiter. As was previously discussed, the previous stages of core accretion complete after $\sim$ several 10^5 years - 1 Myr, and are therefore expected to not be limited by the disk lifetime. This final stage of planet formation, however, can be limited by the disk lifetime provided it takes 1 Myr or longer to complete.

During the early phases of gas accretion during a planet's formation, the planet will be fully embedded within the material of its natal disk. The gas that is gravitationally bound to the planet, making up the planet's envelope, will have properties (density, pressure) that meet continuously with the surrounding fluid reservoir of the disk at the outer radius of the planet. The planet's outer radius can be defined by its Hill radius, r_H (equation 1.31), and represents the boundary between gas gravitationally bound to the planet, and that belonging to the disk. One can model the radial structure of the planet's envelope by solving the following three stellar structure equations (Armitage, 2010),

$$\frac{dM}{dr} = 4\pi r^2 \rho \ , \tag{1.33}$$

$$\frac{dP}{dr} = -\frac{GM}{r^2}\rho \ , \tag{1.34}$$

$$\frac{dT}{dr} = -\frac{3\kappa_R \rho}{16\sigma T^3}\frac{L}{4\pi r^2} \ , \tag{1.35}$$

where M represents the mass contained within radius r, κ_R is the Rosseland-mean opacity of the envelope, and $\rho(r)$, $P(r)$, and $T(r)$ are the radial density, pressure and temperature profiles in the planet's atmosphere.

In equation 1.35, L represents the luminosity of the planet. The energy output of a forming planet can be due to its gravitational contraction, or from energy deposited by impacting planetesimals. In core accretion scenarios, impacting planetesimals dominate the energy output for lower mass planets ($M_p < 20$ $M_\oplus$). In this case, L is referred to as an accretion luminosity. As the planetesimals are impacting the forming planet at the surface of its core, the energy will have to be transported throughout the whole envelope of the planet, and L will take a constant value of (Armitage, 2010),

$$L \simeq \frac{GM_{core}\dot{M}_{core}}{R_{core}} \ , \tag{1.36}$$

where R_{core} is the radius of the planet's solid core, and the location where energy is deposited during planetesimal impact.

During formation, this energy will have to be transported throughout the planet's envelope either via radiation or convection (the mode of energy transport determined via a Schwarszchild criterion) and deposited into the surrounding reservoir of the protoplanetary disk. This cooling and subsequent contraction of the atmosphere's envelope is a necessary step in order to allow more disk gas to flow into the planet's Hill radius and become gravitationally bound to the planet. The planet's growth timescale,

$$\tau_{grow} = \frac{M_{env}}{\dot{M}_{env}} \ , \tag{1.37}$$

can then be defined in terms of its atmosphere's cooling timescale. Ikoma, Nakazawa & Emori (2000) obtained fits to a numerical model of a forming planet's atmosphere, and phrased the planet's cooling timescale in terms of the Kelvin-Helmholtz contraction timescale,

$$\tau_{KH} \sim 10^8 \left(\frac{M_p}{M_\oplus}\right)^{-2.5} \left(\frac{\kappa_R}{1\,\mathrm{cm^2\,g^{-1}}}\right) \ \mathrm{yr} \ . \tag{1.38}$$

This result suggests that since cooling is the limiting stage in controlling gas accretion onto planets, one can simply calculate the Kelvin-Helmholtz contraction timescale as opposed to calculating detailed structure models of a forming planet's atmosphere throughout its formation. Semi-analytic models such as Ida & Lin (2004, 2008); Hasegawa & Pudritz (2012, 2013) did exactly this, allowing for fast calculations of gas accretion rates in planet formation runs. Equation 1.38 highlights the importance of the envelope opacity in controlling the planet's gas accretion rate. Large values will inhibit rapid cooling and lead to large Kelvin-Helmholtz timescales, while smaller values will allow for large gas accretion rates and favour the formation of massive planets.

To estimate the accretion rate onto a planet early in its gas accretion phase, we compute the Kelvin-Helmholtz timescale with equation 1.38 for a 5 $M_\oplus$ planet with an envelope opacity of 1 cm^2 g^{-1}, and find that such a planet has a gas accretion timescale of $\sim$ 2 Myr. This tells us that early gas accretion onto a planet is a slow process, rivalling the disk's lifetime in duration. The initial gas accretion phase of a planet's formation is referred to as *hydrostatic growth*, owing to the fact that its atmosphere is pressure-supported throughout the duration of this phase as gas accretion drives a slow expansion of its feeding zone. This phase ends when the mass of the planet's envelope becomes similar to the mass of its core ($\sim$ 15-20 $M_\oplus$). Since this stage of planet formation is long, the disk may be dissipated during the planet's hydrostatic growth. In that case, the planet's growth will cease at the time of dispersal, stranding the planet with a low mass, leading to a "failed core" or zone 5 planet (Hasegawa & Pudritz, 2013).

Once $M_{env} \simeq M_{core}$, the planet's atmosphere will no longer be pressure supported, resulting in rapid gas accretion as a consequence of gravitational collapse. Within 10^5 years, the planet can grow from ~ 20 $\mathrm{M}_\oplus$ up to a Jupiter mass (317.83 $\mathrm{M}_\oplus$) while in the runaway growth regime. The Kelvin-Helmholtz cooling timescale (equation 1.38) does predict an accretion timescale that decreases sensitively with the planet's mass as $\tau_{KH} \propto M_p^{-2.5}$, suggesting that massive planets should have much shorter accretion timescales than those early in their formation. Accretion onto high mass planets will continue until the disk is dissipated through photoevaporation, or the accretion onto the massive planet is terminated by other means. Since Kelvin-Helmholtz gas accretion is predicted to happen so quickly for massive planets, it is unlikely that disk dissipation can explain accretion termination for all Jovian planets, as the runaway gas accretion timescale can be as low as 10^3 years while disk dissipation takes place on a $10^4 - 10^5$ year timescale.

A physical mechanism explaining gas accretion shut off as an alternative to termination via disk dissipation is a currently unresolved issue in the core accretion scenario. As is discussed in section 1.4.2, massive planets can clear out annular gaps in their natal disks due to the strong gravitational torques they exert on surrounding material. After they do so, they become somewhat detached from the surrounding disk, but it is unclear to what degree of efficiency this can happen. Nonetheless, many ideas of how gas accretion terminates revolve around the planet opening a gap and becoming detached from the disk, thus being unable to continue to accrete. 3D hydrodynamical models, however, predict that accretion flows through the gap can continue even after than planet has exceeded its gap-opening mass (Kley & Dirksen, 2006). In this case, accretion onto the planet would continue, albeit at a slower rate.

Currently, all models impose an assumption which estimates the amount of material a planet accretes during the runaway growth stage of its formation. For example, some models use strictly a Kelvin-Helmholtz gas accretion rate, followed by an abrupt shut off after the planet has accreted a parameterized amount of material post-gap formation (Hasegawa & Pudritz, 2013, 2014). Alternatively, other models use a disk-limited accretion phase, whereby accretion rates onto the planet are set by the local disk accretion rate (Ida & Lin, 2004, 2008; Mordasini et al., 2012a). These disk-limited models also impose a parameterization that determines what fraction of disk accretion translates into accretion onto the planet. A third method of constraining this problem is by obtaining fits to hydrodynamical simulations, which do predict that gas accretion rates onto planets decrease with planet mass after a gap is formed in the disk (Lissauer et al., 2009; Mordasini et al., 2014). The accuracy of this method however, is limited by the accuracy of the simulation. Furthermore, most fits to hydrodynamic simulations involve some necessary parameterizations, thus limiting their advantages over semi-analytic approaches.

1.4 Planet Migration & Traps

As a planet embedded in its natal protoplanetary disk accretes material, its gravitational influence will exert torques on the surrounding material, altering the disk structure. The back-reaction of this process of the planet affecting disk structure is that the disk material will also exert torques on the forming planet. The result is an angular momentum exchange between the planet and the disk it is forming within, causing the planet's orbital radius to evolve with time throughout its formation. This is referred to as planet migration. The rate of planet migration depends on the planet and local disk properties, and this thesis section will provide an overview of our current understanding of the mechanics behind this process. Planet migration is a key aspect of the model presented in this thesis, of which a detailed description is presented in section 2.2.3.

Early models of core accretion that did not include migration, such as Pollack et al. (1996), predicted that planet formation takes place at or outside the snow line at orbital radii greater than roughly 5 AU. The observed semimajor axes of exoplanets present an apparent disconnect between the core accretion scenario and the observed mass-period distribution of planets. Planet migration presents further understanding of this problem, as it connects the final orbital radii of planets to the radii in the disk where they formed. This allows them to begin forming outside of 5 AU as early models predicted, while migration transports them to their final semimajor axes.

Understanding planet migration is also crucial for tracking compositions of planets during their formation. In-situ formation models that ignore migration predict that the compositions of planets reflect that of the natal disk at the orbital radii of the planets. Migration models conversely predict that a planet's composition will rather reflect the disk's composition over a range of semimajor axes that the planet's migration allowed it to sample throughout its formation. Migration therefore plays a key role affecting planet compositions, as it determines the region in the disk, and associated chemical environment, that planets are able to accrete from. Migration will likely also carry planets across compositional gradients throughout the disk, allowing them to accrete from regions of the disk with different materials present throughout their formation.

The amount of influence a planet can have on the disk's structure depends on the forming planet's mass, with small planetary cores at early stages of formation having small influences on disk material, and more massive planets greatly influencing the local disk structure. Since the resulting migration timescales for the two mass regimes can be drastically different, we separate them into two separate migration regimes,

- **Type-I migration** corresponding to planets with masses less than roughly 15 $M_\oplus$.
- **Type-II migration** corresponding to planets with masses greater than roughly 15 $M_\oplus$.

We will discuss the different physical mechanisms responsible for migration in each regime, as well as the mass-boundary between the two regimes in this section.

1.4.1 Type-I Migration

As previously mentioned, low mass planetary cores embedded within a disk will not greatly alter the disk's global structure. They will, however, influence disk material at or near resonant locations. This is depicted in figure 1.4, which shows the two important effects that a low-mass planet has on disk material as predicted in hydrodynamic simulations.

The first effect the planet will have on the disk is its excitation of spiral waves at Lindblad resonances (figure 1.4, left panel). Lindblad resonances are defined as regions in the disk excited by the planet at the natural frequency for epicyclic oscillations, $\kappa(r)$ (Armitage, 2010),

$$m(\Omega(r) - \Omega_p) = \pm\kappa(r) \ , \tag{1.39}$$

where $\Omega(r)$ corresponds to the orbital frequency of disk material at radius r, Ω_p to the planet's orbital frequency, and m being a nonzero integer. In a Keplerian disk, the epicyclic frequency is equal to the orbital frequency. Replacing $\kappa(r)$ with $\Omega(r)$, one can derive the radii of Lindblad resonances (r_L) as,

$$r_L = r_p \left(1 \pm \frac{1}{m}\right)^{2/3} \ . \tag{1.40}$$

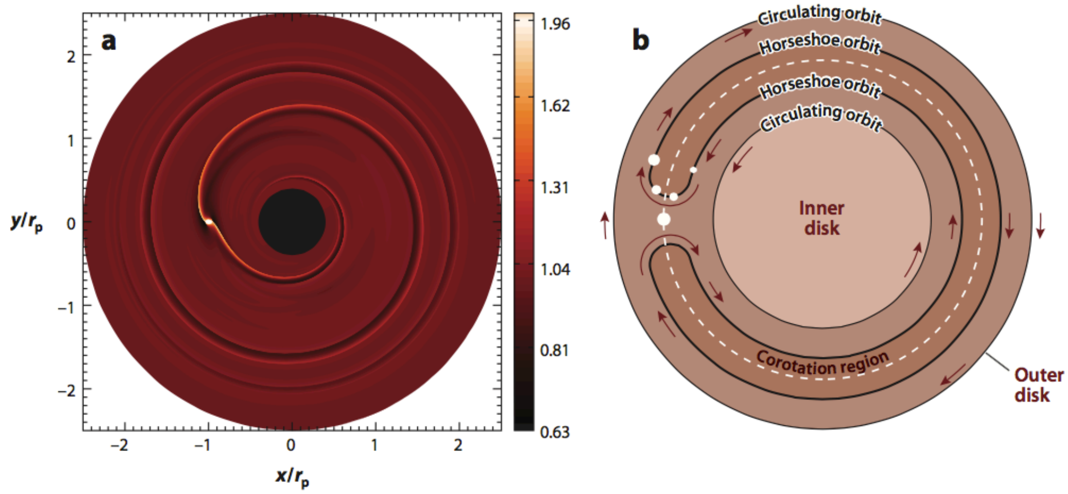

Figure 1.4: The above images illustrate the influence an embedded low-mass planet has on surrounding disk material. **Left Panel:** Simulated image of spiral waves excited throughout the disk at Lindblad resonances by the embedded planet. **Right Panel:** Disk material near the planet's orbital radius undergoes horseshoe orbits. *Credit: Kley & Nelson (2012).*

The second effect the planet has on the disk structure is that it will perturb disk material orbiting at, or near, the planet's orbital radius. The width of this region (called the corotation, or horseshoe region) is roughly twice the planet's Hill radius. Disk material within the corotation region will experience gravitational perturbations from the planet throughout its orbit. These gravitational kicks will cause the disk material to gain, or lose, angular momentum shifting them to slightly higher, or lower orbits. This is depicted in figure 1.4, right panel, which shows the motion of disk material in a frame rotating at the planet's orbital radius.

These two effects that the planet has on disk material in resonant orbits are important because the mutual torques between the planet and the disk that alter the disk's properties result in a transfer of angular momentum between the disk material and the planet. These torques are what causes type-I planet migration. The torque experienced by a low mass forming planet, Γ can be written as a sum of the torques exerted by material at Lindblad resonances Γ_L and by material on corotation orbits Γ_C (Tanaka, Takeuchi & Ward, 2002),

$$\Gamma = \Gamma_L + \Gamma_C \ . \tag{1.41}$$

The Lindblad torque is the net sum of the torques exerted on a planet by disk material at all

Lindblad resonances with respect to the planet's orbit (equation 1.40). Lindblad resonances with m values close to the inverse of the disk's aspect ratio ($(H/r)^{-1}$) typically have the strongest influence on the planet (Armitage, 2010). Tanaka et al. (2002) found the following equation for the Lindblad torque based on linear 3D calculations,

$$\Gamma_L = -(2.34 - 0.1\alpha)\left(\frac{M_p}{M_*}\right)^2 \left(\frac{H}{a_p}\right)^{-2} \Sigma_p a_p^4 \Omega_p^2 \ , \tag{1.42}$$

where M_p is the planet's mass, M_* is the star's mass, H is the disk scale height, a_p is the planet's radius, Σ_p is the disk surface density at the planet's location, and α is defined as the power law index of the disk's Σ profile,

$$\Sigma(r) \sim r^{-\alpha} \ . \tag{1.43}$$

Note the negative sign in front of equation 1.42, showing that the Lindblad torque experienced by a planet is directed inwards towards its host star, causing the planet to lose angular momentum.

We can use equation 1.42 to estimate the migration timescale,

$$\tau_{mig} = \frac{r_p}{|dr/dt|} \ , \tag{1.44}$$

of a forming planet core around a Solar-mass star with $M_p = 1$ $M_\oplus$, $a_p = 10$ AU, and using $\alpha = -1.5$, $(h/r) = 0.05$, and $\Sigma_p = 1000$ g cm^{-2} as typical disk quantities early (~ 1 Myr) in its evolution. Using,

$$\begin{aligned} \Gamma_L &= \frac{dL}{dt} = M_p \frac{d}{dt}(rv) \\ &= M_p \frac{d}{dt}\left(r\sqrt{\frac{GM_*}{r}}\right) = \frac{M_p}{2}\sqrt{\frac{GM_*}{r}}\frac{dr}{dt} \ , \end{aligned} \tag{1.45}$$

and plugging into equation 1.44, we find that $\tau_{mig} \simeq 10^5$ years.

This result tells us that the Lindblad torque causes the forming planet to migrate into its host star and become tidally disrupted on a 10^5 year timescale. This outcome is extremely problematic, as the migration timescale is at least a factor of 10 shorter than the planet formation timescale and disk lifetime, suggesting that planets will migrate into their host stars before they have time to form. In order for the core accretion model to be a plausible formation scenario, the migration rate caused by the Lindblad torque needs to be slowed by at least a factor of 10 to allow the planet enough time to build its core and reach a mass sufficient for type-II migration to apply. This timescale problem suggested by considering the Lindblad torque's effect on a low mass forming planet is known as *the type-I migration problem*.

Previous semi-analytic core accretion models have artificially decreased the rate of inward migration by this necessary factor of 10 to allow for the inclusion of type-I migration (Ida & Lin, 2004). While an artificial decrease was not physically motivated, it was a necessary model feature in order to give planets enough time to form. Physically, the Lindblad-driven inward migration timescale can be slowed if the corotation torque is included and transfers angular momentum from the disk to the planet, and this poses a potential solution to the type-I migration problem.

The corotation torque is caused by the planet's gravitational interaction with disk material undergoing horseshoe orbits with respect to the planet. Every time the planet gravitationally perturbs a fluid element of the disk into a higher or lower orbit, the planet loses or gains a small amount of angular momentum from the gravitational interaction. As this is happening for all the fluid elements within the horseshoe region, the corotation torque is the summation of the torques from all of these disk fluid elements.

If we track a single fluid element throughout its horseshoe orbit, such as the one depicted in figure 1.4, we can see that the planet undergoes two interactions or gravitational kicks throughout the fluid element's horseshoe orbit - one kick sends it to a higher orbit, and one to a lower orbit. If we consider the orbit averaged corotation torque from one fluid element on the planet, we will find that it is zero provided that the fluid element conserves its properties throughout the horseshoe orbit. This is because the two gravitational interactions cancel each other out - the angular momentum gained from one interaction will be the same as the amount lost from the other. This idea can be extended to predict that the time averaged corotation torque that considers the contributions from all fluid elements within the horseshoe region will be zero *if* all the fluid elements conserve their properties throughout their orbits. In this case, the net corotation torque does nothing to help solve the type-I migration problem, and the corotation torque is said to be saturated.

Alternatively, the corotation torque can provide a non-zero effect on the planet if the fluid elements change properties as they undergo their horseshoe orbits. If we again consider a single fluid element on a horseshoe orbit, we can see that it spends roughly half its orbit at a slightly larger semimajor axis and the other half at a smaller one. The disk temperature and surface density profiles decrease with radius, so the fluid element will encounter two regions with different properties throughout its orbit. If the fluid element can mix with the surrounding disk material quickly enough during its horseshoe orbit, then the element will change its properties based on the semimajor axis it is orbiting on. This will cause the two gravitational perturbations the fluid element has with the planet to be different, and can lead to a net angular momentum exchange. In this case, the corotation torque is said to be unsaturated, and can counteract the Lindblad torque.

In order to determine whether or not the corotation torque is saturated, one needs to compare the disk viscous timescale τ_{vis} which sets how quickly the disk's viscosity can allow fluid elements to mix, with the libration timescale τ_{lib} which corresponds to how quickly fluid elements in the planet's horseshoe region complete their horseshoe orbits. These timescales depend on the planet's properties as well as the local disk properties. If $\tau_{vis} < \tau_{lib}$, then the fluid elements can change properties quickly enough during their horseshoe orbits such that the corotation torque is unsaturated. Conversely, if $\tau_{lib} < \tau_{vis}$, then the fluid elements' horseshoe orbits happen too quickly and they do not have sufficient time to mix with surrounding disk material and change properties. This scenario corresponds to a saturated corotation torque.

Tanaka et al. (2002) obtained the following fit describing the strength of the corotation torque in the unsaturated case,

$$\Gamma_C = 0.64(1.5 - \alpha)\left(\frac{M_p}{M_*}\right)^2\left(\frac{H_p}{a_p}\right)^{-2}\Sigma_p a_p^4 \Omega_p^2 \,, \tag{1.46}$$

which is zero for surface density power laws with index $\alpha = 1.5$, as is the case for the minimum mass Solar nebula. With shallower surface density profiles, the corotation torque is positive, providing the planet with angular momentum and countering the Lindblad torque. However, even with an unsaturated corotation torque, most simple disk models predict the Lindblad torque to be dominant (Lubow & Ida, 2010). This means that having an unsaturated corotation torque alone is not sufficient to guarantee the planet migrates slowly enough to have time to form.

The model presented in Masset et al. (2006) showed that regions in the disk with steep surface density gradients had strong corotation torques, with magnitudes comparable to Lindblad torques. This work pioneered the idea of *planet traps* and showed that inhomogeneities in disk surface density profiles acted as barriers to rapid inward type-I migration due to the large corotation torque directed away from the host star. In these regions, it was found that the planet experiences zero net torque as the Lindblad and corotation torques canceled each other. This posed a solution to the type-I migration problem, giving planets sufficient time to form in the core accretion scenario.

The core accretion model coupled with trapped type-I migration was studied in detail in the semi-analytic models presented in Hasegawa & Pudritz (2011, 2012, 2013). These models considered three planet traps causing surface density inhomogeneities. The first trap is the ice line, which exists at the radius in the disk where water undergoes a phase transition, resulting in an opacity transition. The second trap is the heat transition, which is caused by a change in the disk's heating mechanism from viscous dissipation in the inner disk to heating via radiation from the protostar in the outer disk. Lastly, the third trap considered is the outer edge of the dead zone, separating a turbulently active outer disk from an inactive inner disk. These models showed that trapped type-I migration, when included in the core accretion model, can form different types of planets observed in exoplanetary systems, and can also reproduce the distributions of observed planets on the mass semimajor axis diagram (figure 1.1).

Other semi-analytic models have investigated in detail the strength of the corotation torque near planet traps. One such model presented in Dittkrist et al. (2014) used a simple timescale argument as a fit to a detailed hydrodynamic simulation to track the operation of the corotation torque during planet formation. This model found that the corotation torque saturates for planet masses smaller than what is necessary to transition into the type-II migration regime, suggesting that planet traps do not operate throughout the entirety of type-I migration, but rather for only a portion of it. Hellary & Nelson (2012) came to a similar conclusion using a detailed numerical model that included a detailed description of the planet-disk interactions throughout formation. These results suggest that planet traps may be mass dependent, with the corotation torque's magnitude depending sensitively on the planet's mass as well as the location in the disk the planet is forming. Further work on this matter is necessary to better understand the dynamics of low mass forming planets.

1.4.2 Gap Opening & Type-II Migration

As a forming planet accretes and becomes more massive, it starts to exert stronger torques on surrounding disk material. After it reaches a so-called gap opening mass (which is roughly 15 $M_\oplus$ for typical disk properties), the torques it exerts on the disk will become so strong that they act to clear out an annular gap in the disk with width comparable to the planet's Hill radius centred on the planet's orbit, as is depicted in figure 1.5. After the planet has done this, it will no longer be fully embedded in disk material, and the mechanism causing planet migration differs significantly from the type-I migration phase. For this reason, the migration phase corresponding to high-mass

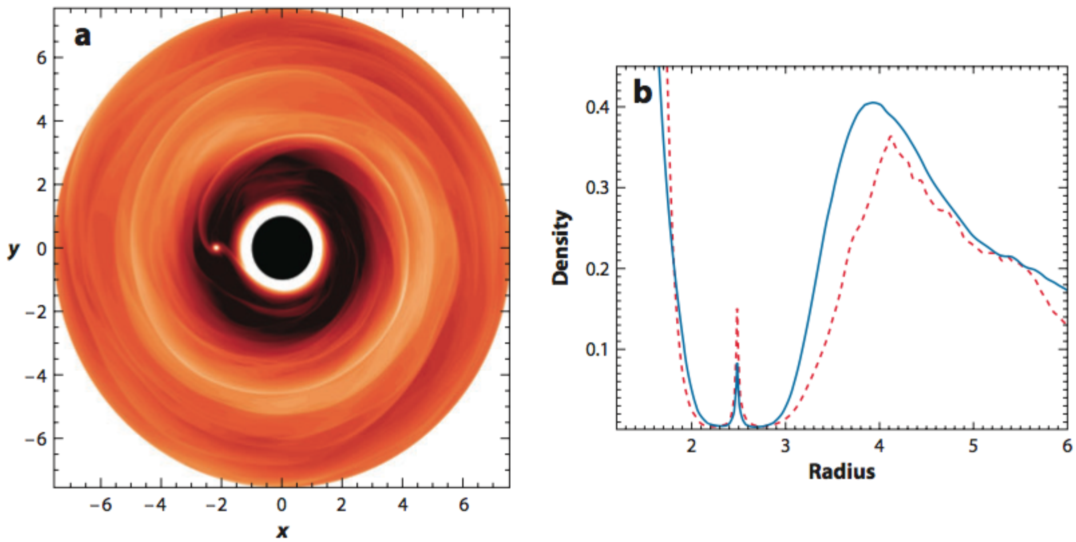

Figure 1.5: Effect that a massive forming planet has on disk structure. **Left Panel:** A massive planet clears an annular gap in the disk as its tidal torques dominate the viscous torques in the disk. **Right Panel:** A radial density profile throughout the disk with a massive forming planet embedded which has opened a gap in the disk. *Credit: Kley & Nelson (2012).*

planets that have cleared out an annular gap in the disk is referred to as type-II migration.

There are two means by which a planet can clear out a gap in the disk that result from studying this process in the 1D fluid regime. The first is that the planet's Hill-radius becomes larger than the disk's local pressure scale height, preventing gas pressure in the disk from closing the gap. Mathematically, this criterion can be derived by setting the planet's Hill radius to the disk pressure scale height,

$$\begin{aligned} R_H &\gtrsim H_p \\ \left(\frac{M_P}{3M_*}\right)^{1/3} a_p &\gtrsim H_p \\ \frac{M_p}{M_*} &\gtrsim 3h_p^3 \,. \end{aligned} \tag{1.47}$$

The second gap-opening criteria suggests that the torque exerted by the planet is strong enough so as to clear out the disk material faster than the fluid viscosity can close the gap (which takes place on the viscous timescale $\tau_{vis} \sim H^2/\nu$). This criteria was derived in Lin & Papaloizou (1993) and is written as,

$$\frac{M_p}{M_*} \gtrsim \frac{40\nu}{a_p^2 \Omega_p} \,. \tag{1.48}$$

For gap-opening to take place, the planet's torque on the disk will have to counteract the gap-suppressing effects of both gas pressure and viscosity simultaneously. The two mass criteria presented above only take into account one suppressing effect at a time. The semi-analytic model presented in Crida et al. (2006) considered both of these effects combined and derived the following criteria that is satisfied by planets massive enough to clear a gap in their natal disk,

$$\frac{3}{4}\frac{H_p}{R_H} + \frac{50\nu_p}{q\Omega_p a_p^2} \lesssim 1 \; , \tag{1.49}$$

where $q = M_p/M_*$ is the ratio of the planet's mass to the star's mass and subscripts p denote the quantities are defined at the planet's location.

After a planet has reached its gap-opening mass, it is unclear what fraction of the gas within the gap will be removed. For planets with masses that are only slightly above the gap-opening mass, a fraction of roughly 20 % of the gas is predicted to remain (Baruteau et al., 2014), while this fraction decreases towards 10 % as the planet grows more massive. For this reason, the planet is not entirely detached from disk material even after an annular gap is cleared. This can allow for accretion onto the planet to continue even though the planet is situated in the low-density environment of a gap during type-II migration.

Once a planet has cleared a gap, its migration timescale is no longer set by the strength of its interaction with disk material at resonant locations throughout the disk. In this regime, the planet acts as an intermediary gravitating body, communicating the viscous torque between the outer and inner edges of the gap in the disk (Lubow & Ida, 2010). Through this mechanism, the planet gets pushed inwards as the disk evolves on the viscous timescale, causing $\tau_{mig} \simeq \tau_{vis} \sim 10^6$ years. It is worth noting that the migration timescale in the type-II phase is roughly an order of magnitude longer than the type-I migration timescale predicted when only considering the Lindblad torque. The type-II migration timescale is also predicted to be longer than the viscous timescale for the most massive planets near the end of their formation ($M_p \gtrsim M_{Jup}$). In this high-mass case, the inertia of the planet can be large enough to resist even the viscous evolution of the disk forcing it inwards (Hasegawa & Pudritz, 2012).

1.5 Planet Population Synthesis

The outcome of planet formation calculations are sensitive to the disk lifetime which sets the upper limit to the timescale planet formation has to take place, and to the disk mass which sets the density of disk material and the core accretion timescale. In this sense, the disk's mass and lifetime can be seen as input parameters to a planet formation calculation, as they play a large role in affecting the type of planets resulting from formation calculations. Determining the outcomes of the core accretion model within disks of different masses and lifetimes is a major goal of this thesis. We study this process in individual disks using only a limited set of disk mass and lifetime values over their corresponding observational ranges.

A more robust method of studying how disk parameters affect planet formation models is through the use of planet population synthesis models. Population synthesis models take into account the observed distributions of disk parameters as priors to a Monte-Carlo simulation, whereby disk parameters are randomly sampled from their observed distributions and used as inputs into a planet formation calculation. Performing large numbers of planet formation calculations allows the observed distributions to be well-sampled in this Monte-Carlo approach, and one can obtain a statistical understanding of the result of their core accretion model through the computed population that results, which takes into account the range of physical environments planet formation takes place within. We note that a population synthesis approach is not presented in this thesis, but is a direct extension of this model and a next step for future work.

The two most common disk parameters whose observed distributions are used in population synthesis approaches are disk lifetimes, and initial disk masses (or surface density profiles) before viscous evolution takes place. For example, Ida & Lin (2008) used a Gaussian distribution of $\log(t_{LT}/10^6 \text{ years})$ with a mean of 6.5 (corresponding to an average disk lifetime of ~ 3 Myr) and standard deviation 0.5. Similarly, they used a Gaussian distribution of $\log(M_{disk,0}/M_\odot)$ with mean -1.66 and standard deviation 0.56. In some studies, such as Mordasini et al. (2009a) and Hasegawa & Pudritz (2014), the distribution of disk metallicities are also included as this sets the dust to gas ratio throughout the disk, directly affecting the planet core formation timescale. As an example, Hasegawa & Pudritz (2014) used a range of dust to gas ratios of $-0.6 \leq \log(f_{dtg}/f_{dtg,\odot}) \leq 0.6$ where $f_{dtg,\odot} \simeq 0.01$ corresponds to the dust to gas ratio in a disk of Solar metallicity.

Comparing the computed population resulting from a population synthesis study with observed distributions of planets on the mass semimajor axis diagram provides a means of testing planet formation models. When comparing with observations, however, it is important to account for the observational biases that are present in the observations and affect the detectability of different exoplanet populations. One method of accounting for observational biases is to perform synthetic observations of a computed planet population. Doing so requires a detailed knowledge of the observational completeness corresponding to a particular observational method for all planet masses, radii, and semimajor axes. Mordasini et al. (2009b) estimate detection probabilities for radial velocity surveys, but to compare with the wealth of data provided by the Kepler survey, one needs to have knowledge of detection probabilities corresponding to a transit survey. The difficulty with this is that it requires the model to compute the physical radii of planets, which requires additional model components - interior structure models and atmosphere models - discussed briefly in the next section.

Comparing results of population synthesis calculations to observed planet distributions allows for model parameters and physical mechanisms themselves to be tested in their ability to reproduce observed planet populations. For example, one can obtain optimal values of a particular parameter in a semi-analytic core accretion model by determining what parameter setting provides the best theoretical fit in a population synthesis approach to observed planet distributions. Additionally, one can compare two competing models of planet growth over a particular size regime in their ability to reproduce observations. For example, this can be done to compare oligarchic growth and pebble accretion - competing theories of planet core formation, or to compare runaway Kelvin-Helmholtz accretion and disk-limited accretion as models of gas accretion onto high mass planets.

The method of population synthesis has been used by several authors over the past decade to constrain core accretion models of planet formation. The semi-analytic model presented in Ida & Lin (2004) pioneered this approach. Subsequent semi-analytic models using this population synthesis approach can be found in Ida & Lin (2008, 2010). Hasegawa & Pudritz (2012, 2013, 2014) used a population synthesis approach to show that the core accretion model that includes the effect of planet traps in type-I migration can reproduce characteristics of the mass-period distribution of observed planets. The Mordasini et al. (2009a, 2012a, b, c, 2014) papers use detailed hydrodynamic simulations to constrain parameters in their semi-analytic models where applicable. Notably, these works use a disk-limited accretion phase to model gas accretion onto high-mass planets. Lastly, Bitsch et al. (2015) used a population synthesis approach to show the range of outputs a core accretion model using pebble accretion to form solid cores can produce.

1.6 Interior Structure Models

The model presented in this thesis aims to calculate super Earth masses and compositions by tracking materials accreted onto planets throughout their formation. These model outputs provide the initial conditions for planetary interior structure models that aim to calculate radial density profiles $\rho(r)$ and in doing so, determine the radii of planets. Such a model provides a mean of mapping planets from the mass-semimajor axis diagram to the mass-radius diagram. This provides an additional means of comparing planet formation results with exoplanetary data. While this thesis does not do interior structure calculations, it is an extension of our model as it directly applies the planet formation results our model computes, and is a prospect for future work.

Interior structures of planets are modelled by solving the modified stellar structure calculations. It is useful to write the equations in the following form, corresponding to a radially symmetric planet that is mineralogically homogeneous (Valencia et al., 2006),

$$\frac{d\rho}{dr} = -\frac{\rho g}{\phi} \, , \tag{1.50}$$

$$\frac{dg}{dr} = 4\pi G\rho - \frac{2Gm}{r^3} \, , \tag{1.51}$$

$$\frac{dm}{dr} = 4\pi r^2 \rho \, , \tag{1.52}$$

$$\frac{dP}{dr} = -\rho g \, , \tag{1.53}$$

where g is the gravitational acceleration at radius r, and ϕ is the seismic parameter that can be determined using the equation of state of the particular material the planet is composed of.

Like terrestrial planets in the solar System, super Earths are expected to be differentiated whereby the heavy iron-based refractories comprise the planet's solid core, the silicate-based materials build up the planet's mantle, and ice and water lie on the planet's solid surface. Care must be taken when applying the above equations, which correspond to a homogeneous planet, to differentiated planets since their compositions vary with radius. Interior structure models do this by building the planet out of spherical slabs of material that are compositionally different - first by calculating the structure of its iron core, then the rocky mantle, and finally the ice/liquid water component on the planet's surface. Doing this requires knowledge of what fraction of the planet's mass is in each of these different components (core materials, mantle materials, ice), and these fractions are treated as parameters in structure calculations. As this thesis' model computes compositions of planets during formation, our results can inform the values chosen for these mass fractions.

The results of an interior structure model will provide a $\rho(r)$ profile and planet radius for a given planet mass and mass fractions in irons, silicates, and ice. For example, figure 1.6 show the resulting planet radii as functions of planet masses and compositions. The radii of planets depend on their mean densities, with denser planets necessarily being composed of denser materials. Therefore, a planet composed only of irons and silicates will be denser, and have a smaller radius, than a planet with the same mass that has a substantial amount of water (Valencia et al., 2007). We note that a planet's radius is not a unique function of its mass, as it is possible to obtain the same radii for planets with different compositions. The problem of determining a planet's composition via its mass and radius is therefore degenerate, as different compositions can lead to planets of the same mass having the same mean density. Interior structure models provide a means of studying what sets of compositions lead to degeneracies in planet radii for a given mass, as is shown in figure 1.6.

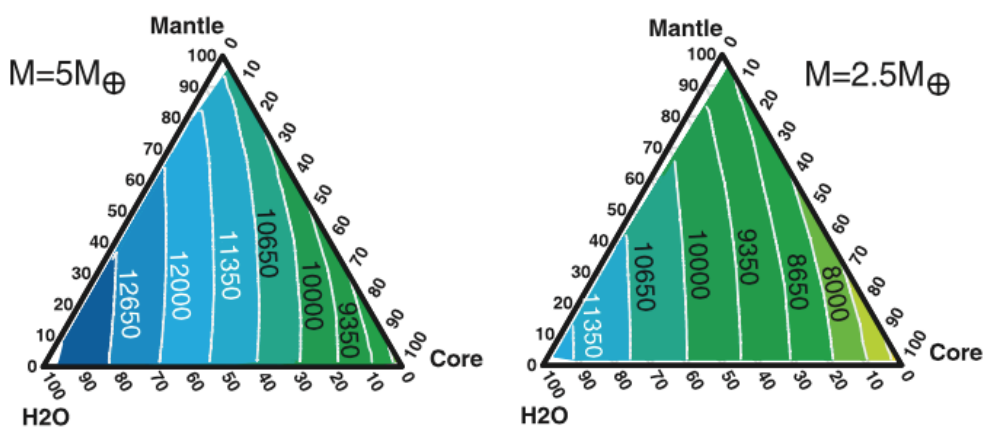

Figure 1.6: Results of interior structure calculations are shown using ternary diagrams. Each axis corresponds to a mass fraction in irons, silicates, and water. The contours throughout the diagrams represent the planet's radius in km. Planets composed of lighter materials have larger radii as the mass is held constant. These diagrams also show that a large set of compositions lead to the same planetary radii. *Credit: Valencia, Sasselov & O'Connell (2007).*

Recent modelling presented in Thomas & Madhusudhan (2016) has shown that super Earth structure and radii are extremely sensitive to how their water component is modelled. Since water is a lighter material than the refractories that build up the planet's interior, changes in the equation of state used for water can have significant effects on the planet's radius. It is therefore necessary to have knowledge of the thermodynamic conditions on a planets surface in order to accurately model the structure of the ice/water component on a planet. The temperatures and pressures on the planet's surface can be computed by modelling their atmospheres.

Super Earths are not composed entirely of solids and water, but are rather seen to have a small fraction of their masses in an atmosphere, which is typically ~ 1 % of their total mass (Wolfgang et al., 2015). As was shown in Lopez & Fortney (2013), even a small atmosphere around a planet can greatly increase its radius, since atmospheres are composed of extremely light materials. Additionally, the structures of super Earth atmospheres are affected by the amount of flux the planet receives from its host star. Thus, including atmosphere models is likely to be important in determining the radii of planets. Even 1D atmosphere models are difficult however, as they are affected not only by the radiation field throughout the planet's atmosphere but also by the atmosphere's composition. Additionally, it is unclear whether a super Earth will retain all the gas it accretes after the disk dissipates. While atmosphere models are beyond the scope of this thesis, our planet formation results can also inform these models as our model calculates how much gas a planet accretes, as well as estimating the gas' composition (albeit using an equilibrium model).

Chapter 2

On the Formation and Chemical Composition of Super Earths

Matthew Alessi, Ralph Pudritz, & Alex Cridland

N.B.: This chapter has been accepted for publication in Monthly Notices of the Royal Astronomical Society (DOI: 10.1093/mnras/stw2360) and summarizes the new research described in this thesis.

Abstract

Super Earths are the largest population of exoplanets and are seen to exhibit a rich diversity of compositions as inferred through their mean densities. Here we present a model that combines equilibrium chemistry in evolving disks with core accretion that tracks materials accreted onto planets during their formation. In doing so, we aim to explain why super Earths form so frequently and how they acquire such a diverse range of compositions. A key feature of our model is disk inhomogeneities, or planet traps, that act as barriers to rapid type-I migration. The traps we include are the dead zone, which can be caused by either cosmic ray or X-ray ionization, the ice line, and the heat transition. We find that in disks with sufficiently long lifetimes ($\gtrsim$ 4 Myr), all traps produce Jovian planets. In these disks, planet formation in the heat transition and X-ray dead zone produces hot Jupiters while the ice line and cosmic ray dead zones produce Jupiters at roughly 1 AU. Super Earth formation

takes place within short-lived disks ($\lesssim$ 2 Myr), whereby the disks are photoevaporated while planets are in a slow phase of gas accretion. We find that super Earth compositions range from dry and rocky (< 6 % ice by mass) to those with substantial water contents (> 30 % ice by mass). The traps play a crucial role in our results, as they dictate where in the disk particular planets can accrete from, and what compositions they are able to acquire.

2.1 Introduction

The growing sample of nearly 3000 observed exoplanets with over 2500 unconfirmed candidates has revealed new and unexpected populations of planets that do not share a Solar system analogue (Borucki et al. 2011, Mayor et al. 2011, Cassan et al. 2012, Rowe et al. 2014, Morton et al. 2016, see also exoplanets.org). The robustness of planet formation theories can be tested in their ability to reproduce these statistically significant populations of planets on the mass semi-major axis diagram, such as super Earths (1-10 $M_{\oplus}$), hot Neptunes ($\sim$ 10-30 $M_{\oplus}$), hot Jupiters, and 1 AU Jupiters (Ida & Lin, 2004, 2008; Mayor et al., 2011; Chiang & Laughlin, 2013; Hasegawa & Pudritz, 2013).

The distribution of observed planets on the mass-radius diagram adds another set of data to constrain models of planet formation. This distribution reveals a range of mean densities of planets that have similar masses (Fortney, Marley & Barnes, 2007; Howard et al., 2013), suggesting an interesting variety of chemical compositions among them. How, then, can planets that have similar masses and semi-major axes achieve such different compositions? This could arise for several reasons, such as variations in metallicities of their host stars, or the accretion of material at different locations in disks around stars with similar compositions. Our work studies the latter case, whereby planet compositions are intimately linked to their formation history.

In order to track materials accreted onto a planet throughout its formation, the physical and chemical conditions throughout the protoplanetary disk it is forming within must first be modelled. One approach is to use equilibrium chemistry, whereby the Gibbs free energy of the system is minimized (White, Johnson & Dantzig, 1958). This technique is useful in determining chemical abundances throughout a complex system, and has been used in previous studies of disk chemistry (Pasek et al., 2005; Pignatale et al., 2011). Solid compositions are largely unaffected by non-equilibrium effects mainly due to their short equilibrium timescale (Toppani et al., 2006), allowing for equilibrium chemistry models to obtain good estimates of condensation sequences along the disk's midplane.

Due to the method's ability to model solid chemistry, this technique has largely been used to track compositions of terrestrial planets throughout their formation (Bond, O'Brien & Lauretta, 2010; Elser, Meyer & Moore, 2012; Moriarty, Madhusudhan & Fischer, 2014). However, non-equilibrium effects such as photodissociation, grain-surface reactions, and ion driven chemistry are expected to be present within protoplanetary disks (Visser & Bergin, 2012; Cleeves, Bergin & Adams, 2014) and will affect gas-phase chemistry. Gaseous abundances are therefore more reliably studied when taking non-equilibrium effects into consideration.

In this paper, we apply the technique to modelling planet compositions as they form in the core accretion model, a model of Jovian planet formation. We focus on the compositions of super Earths and hot Neptunes as their masses are mainly in solids, where our chemistry method is most applicable.

The core accretion model is a bottom-up process of planet formation whereby an initially small ($\sim 0.01 M_{\oplus}$) planetary embryo grows by accreting $\sim$ 1-10 km-sized planetesimals before becoming massive enough to accrete gas from the disk (Pollack et al., 1996; Hubickyj, Bodenheimer & Lissauer, 2005). As was shown in Hasegawa & Pudritz (2012) and Ida & Lin (2004), this model predicts the formation of massive (1-10 Jupiter mass) gas giants in average to long-lived disks ($\gtrsim$ 2 Myr). If the process of photoevaporation is efficient enough to disperse the disk before the planetary core can accrete substantial amounts of gas, the core will be unable to continue growing. One can recognize the failed cores that result from these short-lived disks ($\lesssim$ 2 Myr) as super Earths and hot Neptunes (Hasegawa & Pudritz, 2013).

The success of the core accretion model is seen in its ability to reproduce the observed distribution of planets on the mass-period diagram (Ida & Lin, 2008; Hasegawa & Pudritz, 2012, 2013; Mordasini et al., 2015). One of the key processes shaping this distribution is planet migration. Througout its formation, the gravitational interaction between a planet and the surrounding disk results in an exchange of angular momentum (Goldreich & Tremaine, 1980; Menou & Goodman, 2004; Hellary & Nelson, 2012). Properly accounting for migration throughout all stages of planet formation is critical to understand where in the disk a planet is forming and therefore what material it accretes.

Planet traps are a key feature of our core accretion model, and are used to model planet-disk interactions and radial migration throughout a large portion of planet formation. Planet traps arise from inhomogeneities in disks and act as barriers to rapid type-I migration (Masset et al., 2006; Matsumura, Pudritz & Thommes, 2007). The inhomogeneities we study in our model are the outer edge of the dead zone (a transition from an MRI inactive to active region), the ice line (an opacity transition), and the heat transition (an entropy transition). Planet traps have been combined with a semi-analytic core accretion model in Hasegawa & Pudritz (2011, 2012, 2013) and have been shown to play a key role in reproducing the mass-period distribution of exoplanets. Here, our work builds upon these previous studies and attempts to determine how planet formation in traps affects their compositions.

The goal of this paper is to combine chemical models of protoplanetary disks with the core accretion model in order to account for the formation of different classes of planets as well as the chemical variety observed among super Earths. After obtaining planet masses and compositions at the end of their formation, we hope to provide initial conditions for modelling the interior structures of planets in the super Earth and hot Neptune population (Valencia, Sasselov & O'Connell, 2007). By including the effects of trapped type-I migration, we will reveal what effect planet traps have on the compositions of planets formed in our models.

As our work combines planet formation with migration, the materials a planet accretes change with both its position and time. Computing a time dependent chemical disk model offers an improvement on previous works which have limited their focus to the disk chemistry at a single time in the disk's evolution (Bond et al., 2010). The work we present here tracks planet formation from oligarchic growth (core formation) through the end of runaway gas accretion, and can be considered a global model of planet formation as it covers physical processes over a wide range of planet masses. This builds on previous works that have studied one aspect of Jovian planet formation in detail, such as gas accretion, migration, or oligarchic growth (Lissauer et al. (2009); Kley (1999); Hellary & Nelson (2012), respectively).

We first outline our model of the physical and chemical conditions in sections 2.1 and 2.2, respectively. With a disk model in hand, the locations of different planet traps can be calculated, and are discussed in section 2.3. The planet formation model we use is then outlined in section 2.4. In section 3, we present individual planet formation tracks and resulting compositions while varying important parameters in our model such as disk mass and lifetime. We focus primarily on conditions giving rise to super Earths and hot Neptunes, and what range of compositions among these planets our model predicts. We leave a complete statistical treatment of this to our next paper (Alessi, Pudritz, & Cridland 2016, in prep.). Finally, in section 4 we discuss key implications and conclusions of our work.

2.2 Model

2.2.1 Accretion Disk Model

The core accretion model predicts that Jovian planet formation occurs on a timescale of a few million years (Pollack et al., 1996). This timescale is comparable to the viscous timescale for protoplanetary disks. Therefore, the disk that a Jovian planet is forming within will evolve substantially throughout its formation as accretion onto the host star takes place (Chambers, 2009). Due to this, we require a dynamic and evolving disk in our model to account for the changes in disk properties over the course of a planet's formation. This leads to disk chemistry being inherently time dependent, as the governing temperatures and pressures throughout the disk are decreasing. Disk evolution is crucial in our model, as time-dependent physics and chemistry throughout the disk lead to planet traps sweeping through the disk, allowing planets forming within them to encounter regions with different materials available for accretion.

The analytic, 1+1D disk model presented in Chambers (2009) will be used throughout this paper. An analytic disk model is advantageous for our work as it allows us to efficiently calculate the conditions throughout the disk while modelling disk chemistry and planet formation. The self-similar approach adopted by Chambers (2009) simultaneously models viscously heated, active inner regions of the disk and the outer regions that are passively heated by direct irradiation of the host star. In doing so, it merges the viscous disk models that are used for planet formation (Hasegawa & Pudritz, 2012; Ida & Lin, 2004) with models that are aimed at reproducing observed spectra of disks (D'Alessio et al., 1998, 1999) that only consider heating by radiation. The Chambers (2009) model also has one of the three traps we are interested in tracking, the heat transition, built into the mathematical framework. However, it does not include the effects of an ice line or dead zone, which is a drawback of the model. To track these two traps, we use our disk chemistry (see section 2.2) and ionization (see section 2.3) models. We note that while we are able to use the disk structure to calculate the location of the ice line and dead zone, the back-reaction of these effects on the disk structure is not included.

The disk model in Chambers (2009) gives an analytic solution to the viscous evolution equation describing the surface density profile $\Sigma(r, t)$ of a circumstellar disk in polar coordinates,

$$\frac{\partial \Sigma}{\partial t} = \frac{3}{r}\frac{\partial}{\partial r}\left[r^{1/2}\frac{\partial}{\partial r}\left(r^{1/2}\nu\Sigma\right)\right] , \tag{2.1}$$

where ν is the disk's viscosity. As shown in Lynden Bell & Pringle (1974), self-similar solutions to this equation can be obtained for alpha disk models where the viscosity in the disk is taken to be proportional to the sound speed c_s and disk scale height H (Shakura & Sunyaev, 1973),

$$\nu = \alpha c_s H \ , \tag{2.2}$$

where α is the effective viscosity coefficient.

We expect there to be multiple sources of angular momentum transport in disks, such as by torques exerted by MHD disk winds as well as MRI generated turbulence (the latter, outside the dead zone). The disk's effective α can then be written as a sum of individual α_i parameters characterizing particular angular momentum transport mechanisms. For example, in the case where disk angular momentum is transported through a combination of disk winds and MRI turbulence,

$$\alpha = \alpha_{\rm wind} + \alpha_{\rm turb} \ . \tag{2.3}$$

While our model uses α values corresponding to these two means of angular momentum transport, other possible mechanisms such as the hydrodynamic zombie vortex instability (Mohanty, Ercolano & Turner, 2013; Marcus et al., 2015) can fit within this framework by adding subsequent α parameters to equation 2.3.

The activity of the MRI instability depends on the ionization rates throughout the disk, discussed in detail in section 2.3. In the MRI active regions of the disk, $\alpha_{\rm turb} \sim 10^{-3} - 10^{-2}$, whereas it is $\sim 10^{-5}$ in the MRI inactive regions (referred to as the dead zone). It has been shown recently in Gressel et al. (2015) and Gressel & Pessah (2015) that disk winds can maintain disk accretion rates through the MRI dead zones in disks. We therefore make the assumption that the disk's effective α is a constant throughout the disk with a particular value of $\alpha = 10^{-3}$ used.

The Chambers (2009) model describes disk evolution under the influence of only viscous processes. An additional source of disk evolution is expected to be caused by high energy radiation from the protostar slowly dispersing the disk material, known as photoevaporation (Pascucci & Sterzik, 2009; Owen, Ercolano & Clarke, 2011). As was shown in Hasegawa & Pudritz (2013), viscous evolution alone cannot reproduce the mass-period distribution of observed exoplanets, and results in low-mass planets being formed too far from their host stars. Photoevaporation's gradual removal of material

Table 2.1: Constants used in the Chambers disk model.

Constant	$T_{vis} > T_{rad}$	$T_{vis} < T_{rad}$
Σ_{vis}	$\frac{7M_0}{10\pi s_0^2}$	$\Sigma_{rad}\left(\frac{T_{rad}}{T_{vis}}\right)^{4/5}$
Σ_{rad}	$\Sigma_{vis}\left(\frac{T_{vis}}{T_{rad}}\right)$	$\frac{13M_0}{28\pi s_0^2}\left[1-\frac{33}{98}\left(\frac{T_{vis}}{T_{rad}}\right)^{52/33}\right]^{-1}$
Σ_0	Σ_{vis}	Σ_{rad}
T_0	T_{vis}	T_{rad}

Table 2.2: Results of the Chambers (2009) disk model. The surface density Σ and temperature T in each of the three zones are given below. In all cases, both Σ and T are found to have power law dependences on the radius in the disk, and the disk's accretion rate (causing them to be functions of time as $\dot{M} = \dot{M}(t)$).

	$r < r_e$	$r_e < r < r_t$	$r > r_t$
$\Sigma(r,t)$	$\Sigma_{evap}\left(\frac{\dot{M}}{\dot{M}_0}\right)^{17/19}\left(\frac{r}{s_0}\right)^{-24/19}$	$\Sigma_{vis}\left(\frac{\dot{M}}{\dot{M}_0}\right)^{3/5}\left(\frac{r}{s_0}\right)^{-3/5}$	$\Sigma_{rad}\left(\frac{\dot{M}}{\dot{M}_0}\right)\left(\frac{r}{s_0}\right)^{-15/14}$
$T(r,t)$	$\frac{T_0\Sigma_0}{\Sigma_{evap}}\left(\frac{\dot{M}}{\dot{M}_0}\right)^{2/19}\left(\frac{r}{s_0}\right)^{-9/38}$	$\frac{T_0\Sigma_0}{\Sigma_{vis}}\left(\frac{\dot{M}}{\dot{M}_0}\right)^{2/5}\left(\frac{r}{s_0}\right)^{-9/10}$	$\frac{T_0\Sigma_0}{\Sigma_{rad}}\left(\frac{r}{s_0}\right)^{-3/7}$

acts as a means to accelerate disk evolution in the viscous framework. This allows planets to migrate inwards on a shorter timescale, forming planet populations consistent with exoplanet data, such as super Earths and hot Jupiters (Hasegawa & Pudritz, 2013). Motivated by these results, we make the following modification to the disk accretion rate presented in Chambers (2009),

$$\dot{M}(t) = \frac{\dot{M}_0}{(1 + t/\tau_{vis})^{19/16}} \exp\left(-\frac{t-\tau_{int}}{\tau_{dep}}\right) \,, \tag{2.4}$$

which includes an exponentially decaying factor which models photoevaporation's effect on the disk's viscous evolution. In the above equation, $\dot{M}_0$ is the disk accretion rate at initial time $\tau_{int} = 10^5$ years, $\tau_{dep} = 10^6$ years is the depletion timescale, and τ_{vis} is the viscous timescale,

$$\tau_{vis} = \frac{3M_0}{16\dot{M}_0} \,, \tag{2.5}$$

where M_0 is the disk's mass at time $t = 0$.

The lifetimes of disks are dictated by the efficiency of the photoevaporation process. The disk lifetime, t_{LT}, is a key parameter in our model, as it sets an upper limit on the timescales that disk evolution, disk chemistry, and planet formation have to take place (Pascucci & Sterzik, 2009; Owen et al., 2011). A fiducial value for the disk lifetime that we adopt in this paper is 3 Myr, although a range of lifetimes as short as 0.5 Myr and up to 10 Myr for the longest lived disks are considered reasonable in our model, as they match with disk lifetimes inferred through disk observations in young star clusters (Hernández et al., 2007). While calculating our disk models, we use equation 2.4 to compute accretion rates for all times $t \leq t_{LT}$. At $t = t_{LT}$, we assume the disk is rapidly dispersed in less than 10^4 years due to photoevaporation dominating disk evolution. Thus, at this time we set the disk accretion rate and mass to zero, halting all subsequent disk evolution, planet formation, and planet-disk interactions.

Throughout the entire disk, the opacity is assumed to be a constant value of 3 g cm^{-2}. This assumption is simplistic, as condensation fronts will play a role in changing the opacity. However, previous works which have used complicated piecewise opacity power laws obtain surface densities and midplane temperatures that are weakly sensitive to the disk's opacity (Stepinski, 1998). Moreover, these models have neglected variations in opacity due to time dependent dust compositions and size distributions. Since we are not employing sophisticated models of dust growth and composition, our assumption of constant opacity simplifies the problem and allows for analytic disk models to be used.

Within the innermost region of the disk, the temperature is so high that dust grains are evaporated. Thus, within the *evaporative radius*, r_e, the opacity will be less than the assumed constant value due to a reduced dust content. The evaporative radius can be calculated using,

$$r_e = s_0 \left(\frac{\Sigma_{evap}}{\Sigma_{vis}}\right)^{95/63} \left(\frac{\dot{M}}{\dot{M}_0}\right)^{4/9} , \tag{2.6}$$

where s_0 is the initial disk radius, and,

$$\Sigma_{evap} = \Sigma_0 \left(\frac{T_0}{T_{vis}}\right)^{4/19} \left(\frac{T_0}{1380\text{ K}}\right)^{14/19} , \tag{2.7}$$

is the surface density constant in the evaporative zone. The viscous heating temperature constant, T_{vis}, is defined in equation 2.9, while the constants Σ_{vis}, Σ_0, and T_0 can be found in table 2.1. Values of r_e for disk masses in the range 0.01-0.05 $M_\odot$ after 1 Myr of evolution are generally $\sim$ 0.1 AU, in agreement with observations (Eisner et al., 2005). Thus this inner region with reduced opacity comprises a small fraction of the disk. The opacity in this region takes on a temperature power law of the form (Stepinski, 1998),

$$\kappa = 3\text{ g cm}^{-2} \left(\frac{T}{1380\,\text{K}}\right)^{-14} , \tag{2.8}$$

and this only applies when $T > T_e \equiv 1380$ K.

We now summarize the formulation of our disk model. All of the remaining equations presented in this section are taken from Chambers (2009). The input parameters to the model are the viscosity parameter α, the initial disk mass M_0, initial disk radius s_0, as well as the mass, radius, and temperature of the protostar (M_*, R_*, T_*). The output of the calculations gives the disk accretion rate as a function of time, as well as time-dependent radial profiles of surface density, and midplane temperature.

When starting the calculation, it must first be determined whether or not an irradiation-dominated region is present by comparing initial temperatures caused by viscous heating and irradiation at the outer edge of the disk. The initial temperature at the outermost point of the disk, s_0, caused by viscous heating is,

$$T_{vis} = \left(\frac{27\kappa_0}{64\sigma}\right)^{1/3} \left(\frac{\alpha\gamma k}{\mu m_H}\right)^{1/3} \left(\frac{7M_0}{10\pi s_0^2}\right)^{2/3} \left(\frac{GM_*}{s_0^3}\right)^{1/6} , \tag{2.9}$$

where σ is the Stefan-Boltzmann constant, γ is the adiabatic index ($\simeq 1.4$), μ is the mean molecular weight ($\simeq 2.4$), k is Boltzmann's constant, m_H is the mass of the hydrogen atom, and G is Newton's gravitational constant. The initial outer temperature caused by irradiation from the central protostar is,

$$T_{rad} = \left(\frac{4}{7}\right)^{1/4} \left(\frac{T_*}{T_c}\right)^{1/7} \left(\frac{R_*}{s_0}\right)^{3/7} T_* , \tag{2.10}$$

where,

$$T_c = \frac{GM_*\mu m_H}{kR_*}. \tag{2.11}$$

After comparing the two initial outer temperatures, several constants are set as shown in table 2.1. If the outer radius is initially in the viscous regime, the input time t needs to be compared with the time at which an irradiated regime is first present at the outer edge of the disk, t_1. This time is determined by first calculating how much the disk radius needs to expand for the two heating mechanisms to produce the same temperature at the outer edge. The time at which the disk expands to this radius is,

$$t_1 = \tau_{vis} \left[\left(\frac{T_{vis}}{T_{rad}}\right)^{112/73} - 1 \right]. \tag{2.12}$$

We note that t_1 is set to zero for disks that initially have outer regions dominated by irradiation. Equation 2.4 can be used to determine the accretion rates whenever $t < t_1$, as these disks are entirely

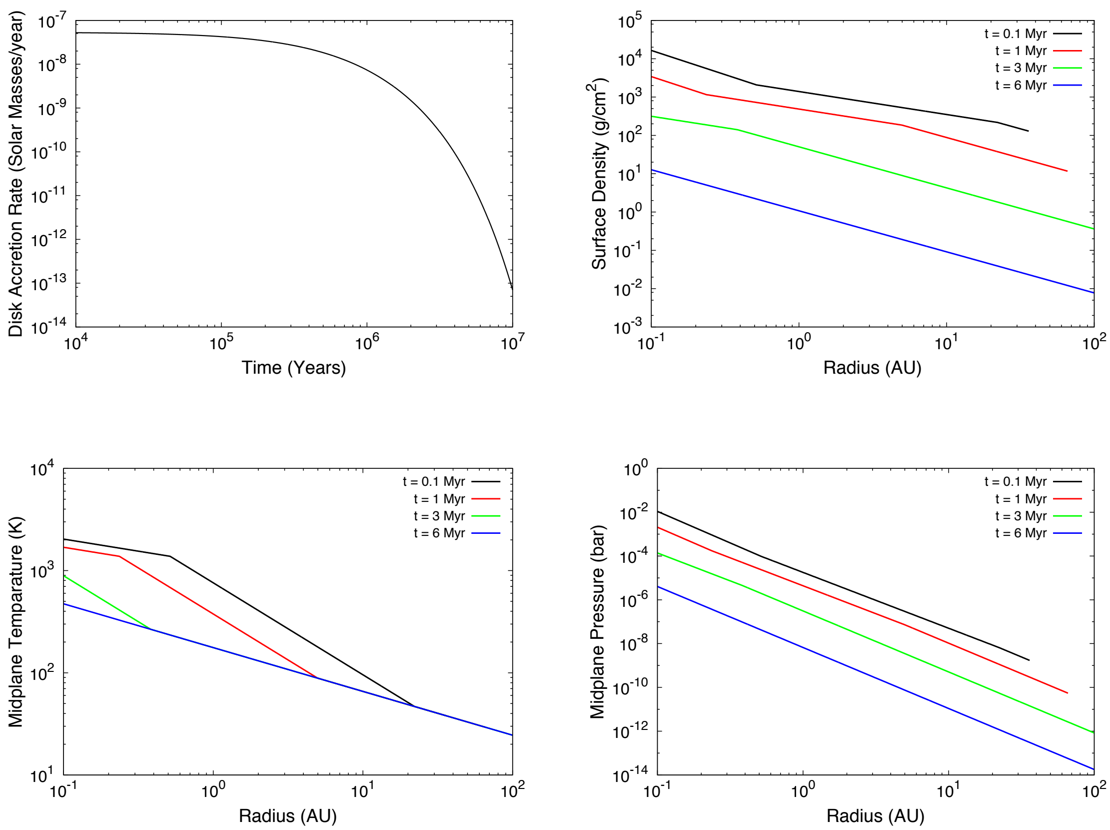

Figure 2.1: The time-evolution of the disk accretion rate along with radial profiles of surface density, midplane temperature and pressure at various times throughout the disk's evolution. These plots pertain to a fiducial disk model whose parameters are outlined in the text. The outer radius of the disk is seen to increase with time in the radial profiles as a consequence of angular momentum conservation as the disk evolves.

viscous. Alternatively, if there is an irradiated region present ($t > t_1$), then the accretion rate at time t_1, defined as $\dot{M}_1$, first needs to be found using equation 2.4,

$$\dot{M}_1 \equiv \dot{M}(t_1) = \frac{\dot{M}}{(1 + t_1/\tau_{vis})^{19/16}} \exp\left(-\frac{t_1 - \tau_{int}}{\tau_{dep}}\right) . \tag{2.13}$$

Then, the accretion rate for time $t > t_1$ is,

$$\dot{M}(t) = \frac{\dot{M}_1}{(1 + (t - t_1)/\tau_{rad})^{20/13}} \exp\left(-\frac{t - t_1}{\tau_{dep}}\right), \tag{2.14}$$

where,

$$\tau_{rad} = \frac{7M_1}{13\dot{M}_1}. \tag{2.15}$$

The disk is divided into three regions; the innermost one being the small ($\sim$ 0.1 AU) evaporative zone previously discussed. The remaining two are defined by regions where the two mechanisms that heat the disk, viscous dissipation and irradiation from the central star, dominate. The model assumes a flared profile in the disk's vertical direction, allowing the outermost regions of this disk to intercept radiation from the star most efficiently. This arises because stellar radiation is the primary source of heating in outer regions of the disk. In the inner regions, the disk's surface density is highest, allowing for viscous dissipation to dominate heating in the inner disk. The radius separating the innermost evaporative zone and the viscously heated zone is given in equation 2.6. The heat transition, r_t, separates the viscous and irradiated regions. It is calculated by determining the radius where the two heating mechanisms result in the same midplane temperature. In the Chambers (2009) model, the heat transition's location is given by,

$$r_t = s_0 \left(\frac{\Sigma_{rad}}{\Sigma_{vis}}\right)^{70/33} \left(\frac{\dot{M}}{\dot{M}_0}\right)^{28/33} . \tag{2.16}$$

Note that both r_e and r_t move inwards with time due to their dependencies on accretion rate. The input radius r is compared with these two radii to deduce what region of the disk is being considered before calculating surface density and midplane temperature. In table 2.2 we present the surface density and midplane temperature profiles within each of the three regions of the disk.

Motivated by defining the external parameters (temperature and pressure) of a chemical system, we include a calculation of the disk's midplane pressure. In order to obtain a midplane pressure from surface density and midplane temperature, the ideal gas equation of state is used,

$$P(r) = \frac{\rho_M(r)kT(r)}{\mu m_H} \,, \tag{2.17}$$

where ρ_M represents the density at the midplane,

$$\rho_M(r) = \frac{\Sigma(r)}{2\pi H(r)} \,, \tag{2.18}$$

and the scale height, H is given by,

$$H(r) = \sqrt{\frac{kT(r)r^3}{\mu m_H G M_*}} \,. \tag{2.19}$$

We assume that the disk is isothermal in the vertical direction z. In the viscous regime of the disk, the disk's effective temperature T_{eff} differs from the midplane temperature by a factor of $(\kappa\Sigma/2)^{1/4}$. We find that this is a factor of order unity using our disk opacity and surface density values within the viscous region. While this vertical temperature gradient is important to consider when calculating disk chemistry away from the midplane, we feel that the assumption of a vertically isothermal disk is justified for our purpose of calculating the midplane pressure. Under this assumption, the density ρ at height z is,

$$\rho(r,z) = \rho_M \exp\left(-\frac{z^2}{2H^2(r)}\right) \,, \tag{2.20}$$

Using the definition of surface density the midplane density can be solved for and input into the ideal gas equation, resulting in,

$$P(r) = \Sigma(r)\sqrt{\frac{GM_*kT(r)}{2\pi\mu m_H r^3}} \,. \tag{2.21}$$

Figure 2.1 shows the disk accretion rate as a function of time, along with radial profiles of surface density, midplane temperature and pressure at several times throughout disk evolution for a fiducial set of model parameters,

$$\begin{aligned} &M_0 = 0.1\ \mathrm{M}_\odot \,,\ \alpha = 10^{-3} \,,\ s_0 = 33\ \mathrm{AU} \,, \\ &M_* = 1\ \mathrm{M}_\odot \,,\ T_* = 4200\ \mathrm{K} \,,\ R_* = 3\mathrm{R}_\odot \,. \end{aligned} \tag{2.22}$$

Our choice of stellar parameters models a pre main sequence Solar type star (Siess, Dufour & Forestini, 2000), while our initial disk mass is chosen such that disk evolution results in disk masses similar to the observed MMSN after 3 Myr (Cieza et al., 2015). We find that our model produces surface density and midplane temperature profiles that compare reasonably well (within a factor of 2 over all disk radii) to those found in D'Alessio, Calvet & Hartmann (2001) and Hueso & Guillot (2005) when using the same initial conditions and disk accretion rate. The kinks present in the radial profiles in figure 2.1 occur at boundaries between the three zones of the disk. We emphasize their presence, predominantly the heat transition, as they are locations of planet traps. The temperature profiles can be seen to all converge to a final profile in this figure. This is due to the assumed constancy of the irradiating stellar flux over the disk's lifetime. This differs from viscous heating as it does not depend on the disk accretion rate (see table 2.2). At late times in the disk's evolution, a decreasing surface density causes the viscous regime to shrink, eventually disappearing altogether. Thus, the entire disk becomes radiation dominated, resulting in a passive, or time-independent, temperature structure.

2.2.2 Equilibrium Disk Chemistry

In order to track accreted materials throughout planet formation simulations, and to constrain the dust to gas ratio within the disk, chemistry has been integrated into our accretion disk model. Here, we assume that the materials present in circumstellar disks are formed in situ rather than being accreted directly from their pre-stellar cores.

The question of "reset" (in-situ formation) vs. "inheritance" (direct transport from the stellar core) is debated as both are plausible mechanisms for chemical evolution of disks (Pontoppidan et al., 2014). While a combination of both mechanisms is likely responsible for the chemical structures of disks, there is evidence that the short chemical timescales lead to the "reset" scenario dominating the chemical evolution in the inner disk regions (Öberg et al., 2011; Pontoppidan et al., 2014). Conversely, direct inheritance likely has a dominant effect in the outer disk (Aikawa & Herbst, 1999).

In our core accretion model, planets accrete materials within 10 AU in the majority of cases (see sections 2.3 & 2.4). While tracking planet compositions, we only consider the in-situ formation of materials to simplify disk chemistry, and assume that the "reset" scenario has the most significant effects on our planetary compositions. We note, however, that the effects of direct inheritance from the stellar core on disk chemistry will likely be important (especially for planets that accrete solids at large disk radii), but are not considered here.

The time-dependent midplane temperature and pressure define the local conditions for a chemical

Table 2.3: Elemental abundances used in equilibrium chemistry calculations. Taken from (Pignatale et al., 2011).

Element	Abundance (kmol)
H	91
He	8.89
O	4.46×10^{-2}
C	2.23×10^{-2}
Ne	1.09×10^{-2}
N	7.57×10^{-3}
Mg	3.46×10^{-3}
Si	3.30×10^{-3}
Fe	2.88×10^{-3}
S	1.44×10^{-3}
Al	2.81×10^{-4}
Ar	2.29×10^{-4}
Ca	2.04×10^{-4}
Na	1.90×10^{-4}
Ni	1.62×10^{-4}

system at each radius within the disk. Equilibrium abundances of gases, ices, and refractories are calculated by determining the set of abundance values that minimizes the disk's total Gibbs free energy. The Gibbs free energy of a chemical system is defined as,

$$G = H - TS \; , \tag{2.23}$$

where H is the enthalpy, T is the system's temperature, and S is the entropy. For a system being composed of N species, the total Gibbs free energy is,

$$G_T = \sum_{i=1}^{N} X_i G_i = \sum_{i=1}^{N} X_i (G_i^0 + RT \ln X_i) \; , \tag{2.24}$$

where X_i, G_i, and G_i^0 are the mole fraction, Gibbs free energy, and Gibbs free energy of formation of species i, respectively.

In order to determine the equilibrium state, the set of X_i which minimize equation 2.24 for a chemical system defined by temperature T and pressure P must be calculated. An additional constraint based on mass considerations is,

$$\sum_{i=1}^{N} a_{ij} x_i = b_j \quad (j = 1, 2, \ldots, m), \tag{2.25}$$

Table 2.4: A list of species present in the chemistry model. Solids that are present in figure 2.2 have their common names bracketed following their chemical formulae.

Gas Phase			Solid Phase		
Al	H	NO_2			
Ar	H_2	Na	Al_2O_3	Fe_2O_3 (Hematite)	Na_2SiO_3
C	H_2O	Ne	$CaAl_2SiO_6$	Fe_3O_4 (Magnetite)	SiO_2
C_2H_2	HCN	Ni	$CaMgSi_2O_6$ (Diopside)	$FeSiO_3$ (Ferrosilite)	FeS (Troilite)
CH_2O	HS	O	CaO	Fe_2SiO_4 (Fayalite)	NiS
CH_4	H_2S	O_2	$CaAl_{12}O_{19}$ (Hibonite)	H_2O	Ni_3S_2
CO	He	OH	$CaAl_2Si_2O_8$	MgO	Al
CO_2	Mg	S	$Ca_2Al_2SiO_7$ (Gehlenite)	$MgAl_2O_4$	C
Ca	N	Si	$Ca_2MgSi_2O_7$	$MgSiO_3$ (Enstatite)	Fe
CaO	N_2	SiO	$FeAl_2O_4$ (Hercynite)	Mg_2SiO_4 (Forsterite)	Ni
Fe	NH_3	SiO_2	FeO	$NaAlSi_3O_8$	Si
FeO	NO	SiS			

where m is the number of elements in the chemical system, x_i is the total number of moles of species i, a_{ij} is the number of atoms of element j contained in species i, and b_j is the total number of moles of element j. The total number of moles, x_i, and the mole fraction, X_i of species i are related by $x_i = X_i \times 100\,\mathrm{kmol}$.

We adopt the HSC Chemistry software package to perform equilibrium chemistry calculations (HSC website: http://www.outotec.com/en/Products–services/HSC-Chemistry/). It includes thermodynamic data, such as enthalpies, entropies, and heat capacities for all chemical species we consider in our model. The Gibbs free energy minimization technique with HSC software has been previously used in astrophysical contexts for chemical modelling of accretion disks (Pasek et al., 2005; Pignatale et al., 2011), as well as for tracking abundances of terrestrial planets during N-body simulations (Bond et al., 2010; Elser et al., 2012; Moriarty et al., 2014).

Elemental abundances must be specified as initial conditions for equilibrium chemistry calculations and were taken from the Solar photosphere, scaled up to a total of 100 kmol (Pasek et al., 2005). In order to reduce computation time, only the fifteen most abundant elements have been included. The remaining ones have abundances $b_j < 10^{-4}$ kmol in the 100 kmol system, and are considered negligible for the calculations. The abundances of the fifteen elements considered in the 100 kmol system are listed in table 2.3.

HSC has thermodynamic data on an extensive list of roughly 100 gaseous and 50 solid phase species that can form from the fifteen elements considered. Ideally, the calculation could be done with each of these having a possibility of forming in the chemical system. However, having such a large number of species to track in a calculation is computationally expensive, so a low resolution trial was first performed to determine the species that are not expected to be present within the protoplanetary disk. The low resolution trial was performed over a temperature range of 50-1850 K with a large temperature step of $\Delta T \simeq 100$ K and at pressures 10^{-11}, 10^{-10}, ... ,10^{-1} bar. These limits were chosen to cover the range of temperatures and pressures calculated with the disk model between 0.1-100 AU and 10^5 - 10^7 years. All species that did not form in this low resolution trial were omitted from future calculations to reduce computation time. Among the species that did form in the low resolution trial were 36 gases and 30 solids recorded in table 2.4. This reduced list of 66 species was used in all subsequent high resolution simulations as a set of possible species that could form in equilibrium chemistry calculations.

Using this reduced list, we then performed a high resolution equilibrium chemistry calculation within the same limits outlined above. We used 200 temperature points in the temperature range of $50 - 1850$ K, resulting in a temperature spacing of $\Delta T = 9$ K. We calculated abundances of all species in table 2.4 at each of these 200 temperatures for 2000 pressures that were equally spaced logarithmically within the range of $10^{-11} - 10^{-1}$ bar. The high resolution calculations allowed us to compute 200×2000 arrays of equilibrium abundances for each substance in table 2.4, with each value in the array corresponding to a particular temperature and pressure. Abundances at T and P values within these grid points are calculated using linear interpolation, which is justified due to the high resolution of the grid. We note that abundances of each individual species are often much more sensitive to temperature than they are to pressure. However, since the pressures that are of interest span several orders of magnitude along the disk's midplane, pressure's effect on the abundances must be taken into account.

Using the disk model, we are able to calculate the temperature and pressure throughout the disk and map our abundances to a location within the disk at a particular time. We emphasize that the abundances throughout the disk are time dependent due to the evolving temperatures and pressures within the disk. This results in time-dependent radial abundance profiles for each substance in our chemistry simulation.

We note that while we do compute abundance profiles of solids throughout the disk, we do not consider their effect on the disk's structure through changing the disk's opacity. While this is a simplification, we note that the disk's midplane temperature has a weak dependence on opacity of $T \sim \kappa^{1/3}$ (see equation 2.9). Therefore, even opacity changes by a factor of 10 will lead to corrections

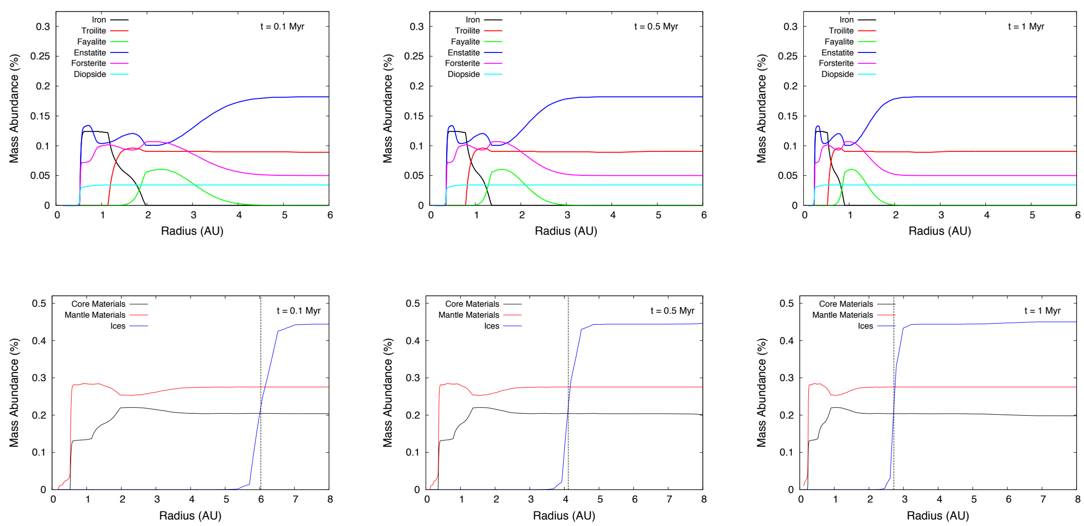

Figure 2.2: **Upper Panels**: Midplane abundance profiles of several important solids at 0.1 Myr (left), 0.5 Myr (center), and 1 Myr (right) into the disk's evolution for a fiducial disk (equation 2.22). Notice that key features in the abundance profile move inwards with time as the disk viscously evolves. **Lower Panels**: Midplane abundance profiles of the three summed solid components at the same times. The water ice line is marked with a black vertical line.

of order unity on our overall disk structure. We have confirmed this by comparing our disk model to the one presented in Stepinski (1998) who used a detailed disk opacity structure, including the ice line's effect on opacity, and finding that our overall surface density and midplane temperature profiles were similar even though our model assumes a constant opacity.

In figure 2.2, top panels, we show several snapshots of the abundance profiles of several prominent minerals along the disk's midplane. Features in the radial abundance profiles of these minerals are seen to shift inwards with time as the disk viscously evolves. We note that while graphite is listed as a solid material that can form in our chemistry model, we do not produce an appreciable amount anywhere in the disk using Solar abundances as our initial condition. The midplane solid abundances we obtain are quantitatively similar with those shown in Bond et al. (2010) & Elser et al. (2012) who also performed equilibrium chemistry calculations on a disk of Solar abundance.

Interior structure models of super Earth-mass planets typically are not interested in abundances of specific minerals. Rather, the abundances of broad groups of solids that characterize where they will end up within the planet's interior after differentiation is of importance (Valencia et al., 2007). Motivated by this, we categorize the solids in our chemical data into three groups:

- **Core Materials :** Iron and nickel based materials, which will build up the core of a differentiated planet. This subset contains eleven of the thirty solids present in the chemistry simulation. The most abundant solids in this subset are iron (Fe), troilite (FeS), fayalite (Fe_2SiO_4), and ferrosilite ($FeSiO_3$).

- **Mantle Materials :** Magnesium, aluminum, and silicate materials, which will build up the mantle of a differentiated planet. This subset contains eighteen of the thirty solids in the chemistry simulation. The most abundant solids in this subset are enstatite ($MgSiO_3$), forsterite (Mg_2SiO_4), diopside ($CaMgSi_2O_6$), gehlenite ($Ca_2Al_2SiO_7$), and hibonite ($CaAl_{12}O_{19}$).

- **Ices** which will lie on the planet's solid surface. This subset only contains water. The omission of CO ices, among others is a limitation of our model, and is discussed in section 2.3.2.

Radial abundance profiles of these three summed components can be seen in the bottom panels of figure 2.2. We find that the ratio between the abundances of mantle materials and core materials throughout the disk is roughly constant, with mantle materials being slightly more abundant. The abundance profile of ice displays a step function profile, with its abundance increasing from zero to its maximum amount of 0.45% in less than an AU. In this sense, the ice line is quite well defined, and we mark its location with a vertical dashed line in figure 2.2. The ice line, along with all other chemical signatures, is seen to shift inwards with time as the disk evolves viscously. The time-dependence of the ice line will be further discussed in section 2.3, as it is one of the planet traps in our model. Lastly, figure 2.2 shows that virtually no solids are present within 0.1 AU as this is the evaporative region of the disk discussed in section 2.1, where the chemistry simulation confirms that the disk temperature is too high for any solids to exist at this location.

In order for equilibrium chemistry to be accurate, the timescale for chemical equilibrium must be shorter than the viscous timescale in the disk, which is $\sim$1 Myr. If this were not the case, the local temperature and pressure governing the chemistry would change faster than the material could find itself in chemical equilibrium. As was found in the experimental work presented in Toppani et al. (2006), solids condense out of nebular gas on short timescales ($\sim$ 1 hour, on average). Thus, they are well represented by an equilibrium approach (Pignatale et al., 2011). Gases on the other hand have equilibrium timescales that are comparable to or longer than 1 Myr, and thus the equilibrium approach in inadequate for this subset of our chemical system. Examples of important non-equilibrium effects are grain surface reactions and UV dissociation (Visser & Bergin, 2012).

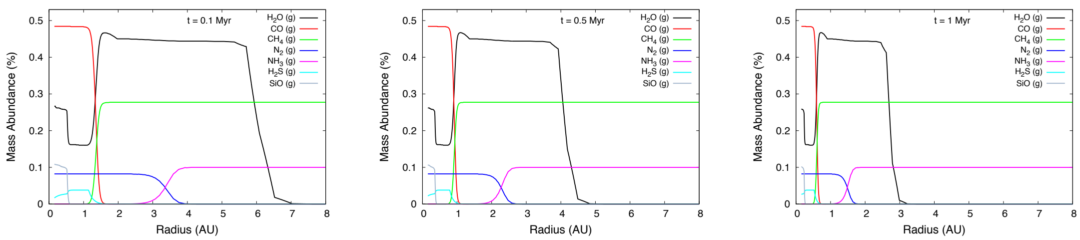

Figure 2.3: Abundance of several prominent gases at 0.1 Myr (left), 0.5 Myr (center), and 1 Myr (right) into the disk's evolution for a fiducial disk (equation 2.22). Crossovers in abundances are shown to exist between carbon monoxide and methane, as well as molecular nitrogen and ammonia. This shows in what molecules it is energetically favourable for carbon and nitrogen, respectively, to exist at different regions of the disk governed by different temperatures. As was the case in figure 2.2, these features are seen to shift inwards with time as the disk evolves.

In figure 2.3, we include abundance profiles of several prominent gases within the disk for completeness. We note that the abundances of molecular hydrogen and helium are by far the most abundant substances in the chemical system. The gases present in figure 2.3 are the gases which have the highest abundances aside from these dominating gases.

Figure 2.3 shows two interesting chemical features among these secondary gases, the first of which occurs at roughly 1.3 AU at 0.1 Myr. This feature displays a crossover in abundances of carbon monoxide and methane, along with an increase in abundance of water vapour, and takes place at a temperature of 1000 K (Mollière et al., 2015). At this location, as the midplane temperature and pressure decrease, it becomes chemically favourable for carbon to exist in methane as opposed to carbon monoxide. The leftover oxygen then combine with the molecular hydrogen, which is extremely abundant throughout the disk, to form more water vapour. This transition between CO and CH_4 is quite abrupt, spanning only a few tenths of an AU.

The second interesting chemical feature shown in figure 2.3 is a crossover between the abundances of molecular nitrogen and ammonia at roughly 3.3 AU at 0.1 Myr. This transition (along with the CO - CH_4 transition) provides a means for explaining the abundances of nitrogen in Terrestrial planet atmospheres in the Solar System, and the amounts of methane and ammonia in the Solar System's Jovians. Here, as the temperature decreases, it becomes more chemically favourable for nitrogen to exist within NH_3 as opposed to N_2. This crossover is much less abrupt, spanning several AU. We note that these distinct transitions in abundances of gaseous molecules are features of the equilibrium chemistry model. Such a sharp transition is not observed when photon driven chemistry and other

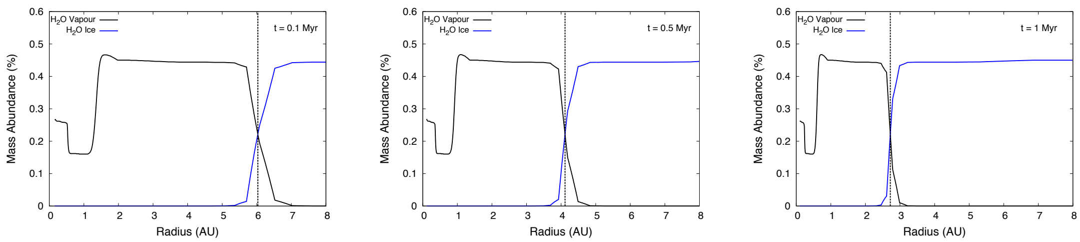

Figure 2.4: Abundance profiles of gaseous and solid water are displayed at 0.1 Myr (left), 0.5 Myr (center), and 1 Myr (right) in a fiducial disk. The vertical lines depict the water ice line in our disk, defined as the radius where the abundance profiles intersect.

non-equilibrium effects are taken into account, such as in Cleeves et al. (2013) and Cridland, Pudritz & Alessi (2016).

2.2.3 Planet Traps

As a planet forms within its natal disk, the mutual gravitational forces cause an exchange of angular momentum between the planet and the disk, leading to planet migration. The two torques that must be accounted for to track a planet's migration through the disk are the Lindblad torque and the corotation torque. As the planet forms, it excites spiral density waves throughout the disk at Lindblad resonances. The Lindblad torque is the summed interaction of the planet with disk material in these spiral waves. For most disk surface density and temperature structures, the Lindblad torque leads to low mass planetary cores losing angular momentum rapidly (Goldreich & Tremaine, 1980). This mechanism of transferring angular momentum from the planet to the disk leads to the planet migrating into its host star on a timescale of roughly 10^5 years. This is problematic, as the core accretion model predicts planet formation to complete on timescales of at least 10^6 years (Pollack et al., 1996). If only the Lindblad torque was operating, then this timescale argument would predict that gas giants cannot form without being tidally disrupted by their host stars. This problem is known as the type-I migration problem.

As a possible mechanism to increase the planet's migration timescale, the corotation torque must also be considered. The corotation torque arises due to gravitational interactions between the planet and disk material orbitting the host star with a similar orbital frequency as the planet. This disk material undergoes horseshoe orbits transitioning from slightly lower orbits than the planet to slightly higher orbits on the libration timescale (Masset, 2001, 2002). If the disk material on horseshoe orbits does not exchange heat with surrounding fluid, there will be no net angular momentum transfer with the planet, and the corotation torque is said to be saturated. In this scenario, the corotation torque cannot act to slow down planet migration, and we are left with the same type-I migration problem outlined above. On the other hand, if the disk material on horseshoe orbits does exchange heat with surrounding disk material, the corotation torque is said to be unsaturated, and acts as a means to transfer angular momentum to the planet (Masset, 2001, 2002). The corotation torque is unsaturated as long as the libration timescale of horseshoe orbits is longer than the disk's viscous timescale. The operation of the corotation torque can act as a means to increase the planet's inward migration timescale to more than 10^6 years as it exerts on outward torque on the planet. This gives planets enough time to form in the core accretion model, and is a solution to the type-I migration problem.

As was shown in Lyra, Paardekooper & Mac Low (2010) and Hasegawa & Pudritz (2011), disks with inhomogeneities in their temperature and surface density structures have unsaturated corotation torques near the inhomeneities. Planets that migrate into these disk inhomogeneities experience zero net torque due to planet-disk interactions. Thus, these inhomogeneities are appropriately named planet traps (Masset et al., 2006). A type-I migrating planet core that migrates to a radius coinciding with a trap will have its inward migration halted, and will grow within the trap. As is discussed in detail in Hasegawa & Pudritz (2011, 2012, 2013), planet traps play a key role in preventing rapid inward migration of forming jovian planets and can reproduce the mass-semimajor axis distribution of exoplanets. The traps themselves migrate inwards on the disk's viscous timescale of roughly 1 Myr, which sets the timescale for the planet's formation. This migration timescale gives the planet enough time to build its core and accrete gases until it becomes massive enough to open up an annular gap in the disk, and liberate itself from the trap.

In this work, we only consider two main migration regimes: trapped type-I migration, and type-II migration following gap formation. Other works, such as Hellary & Nelson (2012) and Dittkrist et al. (2014) consider several type-I migration regimes (one of which is the trapped regime), which depend on the viscous, libration, u-turn, and cooling timescales. These works find that low mass cores (up to $\sim 4M_{\oplus}$) are not trapped, but are rather in a locally isothermal migration regime. Additionally, they find that after the planet is trapped, the corotation torque can saturate for many disk configurations prior to the planet opening a gap in the disk.

We calculate these timescales using our model parameters and find that low mass cores are governed by the locally isothermal migration regime until the reach a mass of $\sim 3-5M_{\oplus}$, depending on the particular trap used. We do not include the effects of this migration regime in this work, and rather force the low-mass cores to be in the trapped regime. Additionally, we find that the corotation torque does not saturate in our planet formation runs until after the planets have opened an annular gap in the disk. Therefore, corotation torque saturation does not affect planets forming in our model. We present this calculation in Appendix A.

The traps that are present within our disk are the heat transition, ice line, and outer edge of the dead zone. Since planets will be forming within the traps, the materials they have available for accretion are dictated by the location of the traps. Therefore, in order to track the materials a planet accretes throughout its formation, it is necessary to have a detailed understanding of the traps' locations in the disk. Below we discuss a summary of the physical origin of each of the three traps in our model, and how they are computed.

Heat Transition

The heat transition exists at the boundary between regions of the disk heated by different mechanisms. As discussed in section 2.1, the inner region of the disk with high surface density is heated predominantly by viscous dissipation, while the outer disk is heated by radiation from the host star due to the disk's flared profile. In order to calculate the location of the boundary throughout the disk's evolution, a heating model must be used. Since this is built into the Chambers (2009) disk model, we can use equation 2.16 to track its location as the disk accretion rate evolves. The heat transition's location is shown to have a power law relationship with $\dot{M}$,

$$r_t \propto \dot{M}^{28/33} \, . \tag{2.26}$$

At the location of the heat transition, the disk's surface density and temperature profile exhibit kinks, or inhomogeneities. Physically, this originates due to an entropy transition across the trap (Hasegawa & Pudritz, 2011).

Ice Line

At an ice line, also known as a condensation front, the disk's opacity changes due to an increased amount of solid grains. While opacity change is not built into our disk model, having a sharp increase in opacity at the ice line would not result in globally different temperature or surface density profiles.

However, at the location of the ice line, the local surface density and temperature profiles would change as a result of the opacity transition (Stepinski, 1998), giving rise to the conditions necessary for a trap (Menou & Goodman, 2004). It is a drawback of the Chambers (2009) model that these effects are omitted. We can still include this trap in the model by a slight modification discussed below.

To first-order, the location of the water ice line can be calculated by tracking the midplane location in the disk that has the condensation temperature of water, 170 K (Jang-Condell & Sasselov, 2004). However, this misses the second-order effects that pressure gradients throughout the disk can have on the ice line's location. Here, we use the equilibrium chemistry code to directly calculate the ice line's location.

Figure 2.4 shows radial abundance profiles of gaseous and solid water along the disk's midplane. We define the location of the ice line, r_{il}, as the point of intersection of the two abundance profiles,

$$X_{H_2O\ \mathrm{gas}}(r_{il}) = X_{H_2O\ \mathrm{solid}}(r_{il}) \ . \tag{2.27}$$

The ice line in figure 2.4 is denoted by a vertical dashed line. As the disk viscously evolves, the water ice line shifts inwards with decreasing disk accretion rate,

$$r_{il} \propto \dot{M}^{4/9} \ , \tag{2.28}$$

which is the same scaling obtained in Hasegawa & Pudritz (2011).

Our definition of the ice line pinpoints one exact radius at each time as the transition between the two phases of water. Figure 2.4 shows that this transition takes place over roughly a few tenths of an AU, which is a small, but non-zero range of radii in the disk. Our model predicts that the disk opacity will be transitioning over this small region, and our definition of the ice line characterizes the average radius where a trapped planet will reside.

The abrupt phase transition of water near the ice line (spanning at most 0.3 AU) may be a result of our simplified 1D model which assumes a constant opacity. The model presented in Min et al. (2011) used a more detailed 2D disk opacity structure while performing radiative transfer calculations. At high accretion rates ($10^{-7} - 10^{-6}$ M$_\odot$/yr), their model found that water undergoes a phase transition along the midplane spanning a larger range of up to ~ 1.5 AU. At lower accretion rates more comparable with typical disk accretion rates ($\dot{M} \sim 10^{-8}$) in our model, however, the Min et al. (2011) model found that the water phase transition spans no more than 0.5 AU along the midplane, which is comparable to the results found in this work.

Our equilibrium chemistry code cannot compute a carbon monoxide ice line, which has been observed around other stars (Qi et al., 2011). Our equilibrium chemistry calculations have resulted in CO having a negligible abundance outside the CO-CH_4 abundance transition, taking place at roughly 1 AU. Given this result, our model does not predict any CO gas in the outer disk for a phase transition to take place. Photon-driven chemistry can cause dissociation of larger molecules, producing CO at intermediate and large radii. Our equilibrium chemistry model does not have the capability to include photon-driven effects. Therefore non-equilibrium chemistry models that include radiation effects, such as those presented in Cleeves et al. (2013, 2014) are best suited to track the structure and location of the CO ice line (Cridland, Pudritz & Alessi, 2016).

We note that we omit the ice line's effect on the disk opacity and resulting temperature and surface density structure in our model. We expect there to be an increase in surface density at the ice line that leads to the dynamic effect of a planet trap, but that is an unnecessary detail for our model as we do not directly compute the lindblad and corotation torques during the trapped type-I phase. Recently, Coleman & Nelson (2016) have shown that condensation fronts are the location of mass-independent planet traps, which further motivates our assumption of trapped migration throughout the type-I migration regime at the ice line.

Dead Zone

The dead zone is a region in the disk where the ionization fraction is insufficient for the magnetorotational instability (MRI) to be actively generating turbulence. Within the dead zone, rapid dust settling takes place due to a lack of turbulence. The outer edge of the dead zone separates the MRI active and inactive regions, and turbulence at this location gives rise to a wall of dust whose radiation heats the dead zone, leading to a thermal barrier on planet migration (Hasegawa & Pudritz, 2010). This section will discuss our method of calculating the location of the dead zone's outer edge, which is a planet trap in our model.

Hasegawa & Pudritz (2011) incorporated a dead zone into their model using a piecewise function for the α parameter governing MRI viscosity. Other models that focus on detailed calculations of ionization rates throughout disks and resulting α values utilize 3D MHD simulations that include the non-ideal effects of ohmic dissipation, ambipolar diffusion, and the Hall effect (Gressel et al., 2015). These works result in α values that vary continuously throughout the disk, resulting in disk accretion rates that are both radially and time dependent. The choice of a constant $\alpha \sim 10^{-3}$ in our analytic model is an average value of these 3D simulations.

Chemical networks are also extremely useful for calculating ionization rates throughout disks. Non-equilbrium chemistry networks are particularly useful as they are able to account for photochemistry and ionization chemistry effects. Inclusion of these important effects allow these models to track ionization and recombination events (Cridland, Pudritz & Alessi, 2016), leading to detailed estimations of ionization fractions throughout the disk and the dead zone's location. The equilibrium chemistry model used throughout this work is limited as it cannot take into account these non-equilibrium effects necessary to track ionizations from first principles. We therefore employ an analytic ionization model as an alternative.

Our calculation of the dead zone follows the analytic model presented in Matsumura & Pudritz (2003). By using an analytic model we are able to efficiently calculate ionization rates and dead zone locations over Myr of disk evolution while capturing the main results of detailed 3D simulations. The complete damping of MRI driven turbulence can be estimated analytically by balancing the MRI growth timescale with the ohmic diffusion timescale for all scales smaller than the disk's pressure scale height (Gammie, 1996). The resulting condition for a dead zone is then expressed via the magnetic Reynolds number (Fleming, Stone & Hawley, 2000; Matsumura & Pudtitz, 2005),

$$\mathrm{Re}_M = \frac{V_A H}{\eta} \lesssim 100 \,, \tag{2.29}$$

where V_A is the Alfvén speed, which is given by,

$$V_A = \frac{B}{(4\pi\rho)^{1/2}} \simeq \alpha_{\mathrm{turb}}^{1/2} c_s = \sqrt{\frac{\alpha_{\mathrm{turb}} kT}{\mu m_H}} \,, \tag{2.30}$$

and η is the diffusivity of the magnetic field (Blaes & Balbus, 1994),

$$\eta = \frac{234}{x_e} T^{1/2} \mathrm{cm}^2\,\mathrm{s}^{-1}. \tag{2.31}$$

It is through the magnetic diffusivity that the magnetic Reynolds number depends on the electron fraction, x_e. It is clear that in regions with sufficiently small electron fractions, η will be large and the

Reynolds number will be small, such that the condition for a dead zone (equation 2.29) is satisfied.

Recent works that use 3D MHD simulations use the magnetic Elsasser number as a measure MRI activity (Blaes & Balbus, 1994; Simon et al., 2013),

$$\Lambda_0 = \frac{V_A^2}{\eta \Omega_K} \lesssim 1 \; . \tag{2.32}$$

The magnetic Reynolds number and the magnetic Elsasser numbers have the same physical origin of a ratio between MRI dissipation and growth, but have slightly different definitions based on the Elsasser number's inclusion of non-ideal MHD effects. Using equations 2.29, 2.30, and 2.32 we see that the magnetic Reynolds number and Elsasser numbers are related by,

$$\Lambda_0 = \alpha_{\rm turb}^{1/2} \mathrm{Re}_M \; . \tag{2.33}$$

Since the α parameter in our disk model is 10^{-3}, the critical magnetic Reynolds number of 100 is consistent within a factor of order unity with a critical Elsasser number of 1. Therefore, our definition of the MRI active regions are consistent with current estimates using the Elsasser number, which take into account 3D MHD effects.

The electron fraction can be calculated in our ionization model as a solution to the following third-degree polynomial (Oppenheimer & Dalgarno, 1974),

$$x_e^3 + \frac{\beta_t}{\beta_d} x_M x_e^2 - \frac{\zeta}{\beta_d n} x_e - \frac{\zeta \beta_t}{\beta_d \beta_r n} x_M = 0, \tag{2.34}$$

where $x_M = 0.0011$ is the metal fraction taken from the initial conditions to our chemistry model (see table 2.3), and n is the local number density of material in the disk. The ionization rate, ζ, takes into account ionization from X-rays ($\zeta = \zeta_X$) or cosmic rays ($\zeta = \zeta_{CR}$).

There are three β terms representing different recombination rate coefficients in equation 2.34: the dissociative recombination rate coefficient for electrons with molecular ions ($\beta_d = 2 \times 10^{-6} T^{-1/2}\,\mathrm{cm^3\,s^{-1}}$), the radiative recombination coefficient for electrons with metal ions ($\beta_r = 3 \times 10^{-11} T^{-1/2}\,\mathrm{cm^3\,s^{-1}}$), and the rate coefficient of charge transfer from molecular ions to metal ions ($\beta_t = 3 \times 10^{-9}\mathrm{cm^3\,s^{-1}}$) (Matsumura & Pudritz, 2003).

The ionization rate from X-ray sources is given by Matsumura & Pudritz (2003),

$$\zeta_X = \left[\left(\frac{L_X}{kT_X 4\pi d^2}\right)\sigma(kT_X)\right]\left(\frac{kT_X}{\Delta\epsilon}\right)J(\tau, x_0)\ , \tag{2.35}$$

where $L_X \simeq 10^{30}$ ergs s^{-1} is the X-ray luminosity of the protostar, and $\sigma(kT_X)$ and $\tau(kT_X)$ are the absorption cross section and optical depth at the energy $kT_X = 4$ keV, which we choose to be an average X-ray energy. The distance between the X-ray source (taken to be 12 $R_\odot$ above the midplane at r= $12R_\odot$, to represent magnetospheric accretion onto the protostar) and some point on the disk surface is denoted by d, and the energy to make an ion pair is $\Delta\epsilon \simeq 13.6$ eV. The first factor in the above equation in square brackets represents primary ionizations, assuming the same energy $E = kT_X$ for all primary electrons. The second term $kT_X/\Delta\epsilon$ represents secondary electrons produced by a photoelectron with energy kT_X. The last factor $J(\tau, x_e)$ represents attenuation of X-rays. The dimensionless energy parameter is defined as $x = E/kT_X$, and the attenuation factor J is written as,

$$J(\tau, x_0) = \int_{x_0}^{\infty} x^{-n}\exp(-x - \tau(kT_X)x^{-n})dx\,. \tag{2.36}$$

The optical depth $\tau(kT_X)$ is given by,

$$\tau(kT_X) = N_H\sigma(kT_X)\ , \tag{2.37}$$

and the absorption cross section is,

$$\sigma(KT_X) = 8.5\times 10^{-23}\,\mathrm{cm}^2\left(\frac{kT_X}{\mathrm{keV}}\right)^{-n}\ , \tag{2.38}$$

where n = 2.81 (Glassgold, Najita & Igea, 1997). The surface number density N_H is measured along the ray path from the X-ray source. If α' is the angle between the ray path and the radial axis, then the surface number density is,

$$N_H = \frac{\int_z^\infty n(a, z')dz'}{\sin\alpha'} \tag{2.39}$$

where a is the disk radius. The integral in equation 2.36 was numerically evaluated by setting the lower limit $x_0 = 1$ and an upper limit of $x = 100$ (Matsumura & Pudritz, 2003).

The ionization rate by cosmic rays is estimated to be 10^{-17} s^{-1} (Spitzer & Tomasko, 1968). Using this with an attenuation length for cosmic rays of 96 g cm^{-2} (Umebayashi & Nakano, 1981),

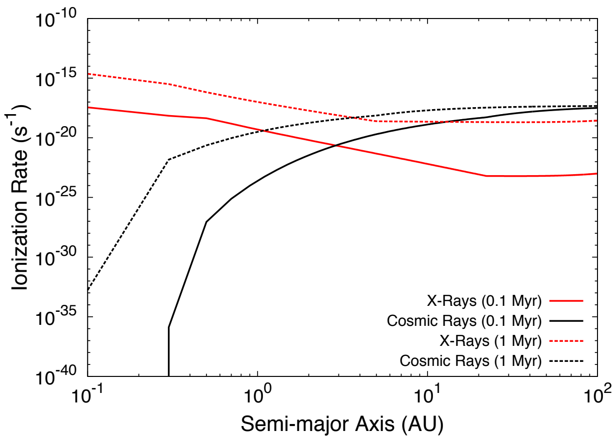

Figure 2.5: Here we picture ionization rates throughout the disk midplane that result from each ionization source. X-rays dominate ionization at small radii, close to the X-ray source, while cosmic rays dominate ionization in the outer disk due to low surface densities. At later times, ionization rates increase due to lower surface densities resulting from disk evolution.

we calculate the ionization rate due to cosmic rays at the disk midplane using (Sano et al., 2000),

$$\zeta_{CR}(a) = \frac{10^{-17}\,\mathrm{s}^{-1}}{2} \exp\left(-\frac{\Sigma(a)}{96\,\mathrm{g\,cm}^{-2}}\right). \tag{2.40}$$

It is currently unclear if X-rays or cosmic rays dominate ionization in protostellar disks. Some models suggest that protostellar winds can attenuate cosmic rays prior to them reaching the disk, resulting in cosmic ray ionization rates 1 to 2 orders of magnitude lower than the assumed value of 10^{-17} s^{-1} (Cleeves et al., 2014). Conversely, recent observations of young protostellar systems have suggested a higher ionization rate throughout molecular clouds (Ceccarelli et al., 2014) than these models would predict. These observations have been attributed to the presence of ionizing cosmic rays which are generated in protostellar jets in the model presented in Padovani et al. (2015).

Due to the uncertainty in the importance of cosmic ray ionization in disks, the ionization model we present here takes the conservative approach of including both X-rays and cosmic rays individually. By separately considering the two ionization effects, we can discern differences in the resulting dead zone locations and time evolutions. Additionally, we can determine the types of planets that form as a result of the dead zone traps caused by the two ionization sources. In a future work, we will use a population approach to determine if the dead zone resulting from each of the two ionization sources can form a mass-period distribution of planets consistent with exoplanetary data (Alessi et al. 2016, in prep.).

In Figure 2.5 we plot ionization rates throughout the disk midplane caused by X-rays and cosmic rays. The ionization rates we obtain agree reasonably well with those presented in Gressel et al. (2015), which were obtained using 3D MHD simulations. A key difference between the two ionization sources in our model is that X-rays originate at the protostar, thus having a diminishing flux at large radii in the disk, while cosmic rays shine down on the disk from an external source and have a constant flux across all radii. We find that X-rays dominate disk ionization in the inner disk, as these regions are closer to the X-ray source, and experience a much higher X-ray flux then outer regions. Additionally, the higher surface densities in the inner disk heavily attenuate cosmic rays, causing the cosmic ray ionization in these regions to be small. In the outer disk, the surface density is smaller, allowing cosmic rays to dominate disk ionization in this region. As the outer regions of the disk are farther from the X-ray source region, more of the X-rays are attenuated by the time they reach the outer disk resulting in a low X-ray ionization rate. Including the effects of X-ray scattering would cause the X-ray ionization rate to be larger in the outer disk than our model predicts, since a portion of the X-rays would be scattered to the outer disk instead of being attenuated. Additionally, figure 2.5 shows that at later times, the ionization rates throughout the disk due to both X-rays and cosmic rays increase. This is due to the disk surface density decreasing as evolution takes place, resulting in lower attenuation rates for both sources.

The X-ray dead zone is the trap that exists at the largest semimajor axes in our model. Planet formation in this trap will lead to planets accreting material within a region of the disk whose chemistry is strongly affected by inheritance from the stellar core (Pontoppidan et al. (2014), see discussion at start of section 2.3), that we do not account for in our chemistry model. We note, however, that the X-ray dead zone trap quickly evolves towards the inner regions of the disk, within several 10^5 years, where the chemistry is dominated by in-situ formation of material that our model considers. Therefore, we do not expect the process of inheritance of chemical materials from the stellar core to have a strong impact on our resulting planet compositions.

After the ionization rates throughout the disk have been determined, the electron fraction x_e as a function of radius can be obtained by numerically solving equation 2.34 at each disk radius. Lastly, the particular radius that gives an x_e satisfying equation 2.29 will be the location of the outer edge of the dead zone.

Figure 2.6 shows the location of the planet traps in the Chambers disk with fiducial parameters (equation 2.22) evolving with time. In this figure, we calculate the dead zone's location by considering X-ray and cosmic ray ionization rates individually. We note that the ionization source does not affect the location of the heat transition or ice line. For the majority of a typical disk's lifetime, the cosmic ray dead zone lies interior to the ice line while the heat transition lies outside. The X-ray dead zone is seen to lie exterior to the ice line only at the earliest times in figure 2.6. After intersecting the heat transition at several 10^5 years, the X-ray dead zone quickly migrates to the innermost regions of the disk, and is the only planet trap in our model to migrate interior to 0.1 AU for a fiducial disk. This behaviour shows that the evolution of the X-ray dead zone is sensitive to the local surface density and temperature profiles. Within the viscous regime, the X-ray dead zone evolves drastically, whereas in the irradiated regime its evolution is much slower.

Throughout the disk's lifetime, the traps intersect, and planets forming within these traps will have a non-negligible dynamical interaction. Dynamical interactions between planets forming within different traps has been considered in Ida & Lin (2010); Hellary & Nelson (2012); Ida, Lin & Nagasawa (2013); Alibert et al. (2013) & Coleman & Nelson (2014). Dynamic effects between multiple forming planets in one disk is not accounted for in our work, as we assume that individual planets form in isolation. Including dynamics between forming planets in our model will be the subject of future work.

2.2.4 Core Accretion Model

We follow the formalism presented in Hasegawa & Pudritz (2012) to calculate accretion and migration rates throughout a planet's formation, which is based upon the model developed in Ida & Lin (2004). In this model, there are several critical masses that act as boundaries between various migration and accretion regimes that a forming planet must surpass as it accretes material, building up a Jovian mass planet. We discuss below in detail these various critcial masses and timescales while summarizing in table 2.5.

We begin our planet formation calculations at 10^5 years into the disk's lifetime with a 0.01 $M_{\oplus}$ core situated at a semimajor axis that coincides with a particular trap in the disk. While it is unlikely that a planetary core will initialize at the exact location of a planet trap, the type-I migration timescale is short enough that the core will rapidly migrate inwards until it encounters a trap. Low mass cores accrete solids via the oligarchic growth process in our model. During this

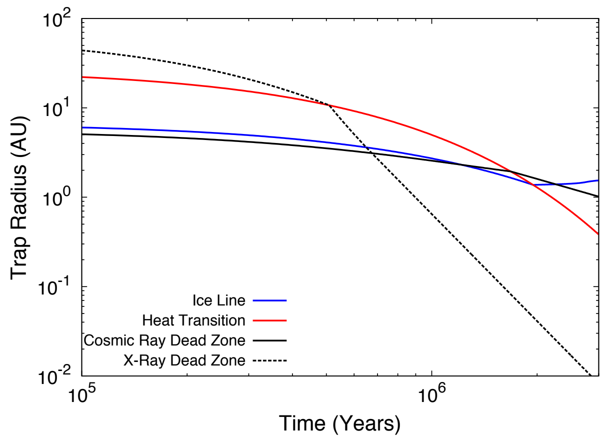

Figure 2.6: Time evolution of planet traps throughout the disk with fiducial parameters (see section 2.1). We compute dead zone locations by considering both X-ray and cosmic ray ionization individually.

phase, we increase the disk's solid surface density to 0.1Σ. This is an order of magnitude beyond the dust-to-gas ratio predicted by the chemistry model. This increase was necessary in order for our model to produce gas-accreting cores on timescales smaller than a fiducial disk lifetime of 3 Myr that lead to Jovian planets forming. Physically, this enhancement of solids can be caused by the effects of dust trapping (Lyra et al., 2009), but currently the value of the solid increase is a free parameter in our model. The planet's accretion timescale in this regime is (Kokubo & Ida, 2002),

$$\begin{aligned}\tau_{c,acc} \simeq & 1.2 \times 10^5 \text{ yr } \left(\frac{\Sigma_d}{10 \text{ g cm}^{-2}}\right)^{-1} \times \left(\frac{r}{r_0}\right)^{1/2} \left(\frac{M_p}{M_\oplus}\right)^{1/3} \left(\frac{M_*}{M_\odot}\right)^{-1/6} \\ & \times \left[\left(\frac{b}{10}\right)^{-1/5} \left(\frac{\Sigma_g}{2.4 \times 10^3 \text{ g cm}^{-2}}\right)^{-1/5} \times \left(\frac{r}{r_0}\right)^{1/20} \left(\frac{m}{10^{18} \text{ g}}\right)\right]^2 ,\end{aligned} \tag{2.41}$$

where $\Sigma_d = 0.1\Sigma$ is the surface density of solids, M_p is the mass of the core, $b \simeq 10$ is a parameter used to define the feeding zone of the core, $\Sigma_g = 0.9\Sigma$ is the surface density of gas, and $m \simeq 10^{18}$ g is the mass of planetesimals being accreted. Using this timescale, the growth of cores is given by,

$$\frac{dM_p}{dt} = \frac{M_p}{\tau_{c,acc}} \propto M_p^{2/3} . \tag{2.42}$$

This stage of core formation, where the planet is accreting solids from a planetesimal disk prior to

Table 2.5: A summary of accretion and migration for various mass regimes throughout our core accretion model.

Mass Range	Migration	Accretion
$M < M_{c,crit}$	Trapped type-I	Planetesimals
$M_{c,crit} < M < M_{\rm GAP}$	Trapped type-I	Gas & Dust
$M_{\rm GAP} < M < M_{\rm crit}$	Type-II	Gas & Dust
$M_{\rm crit} < M < M_{\rm MAX}$	Slowed type-II	Gas & Dust
$M > M_{\rm MAX}$	Slowed type-II	Terminated

gas accretion will be referred to as stage I of planet formation.

During oligarchic growth, a small gaseous envelope surrounding the planetary core will be in hydrostatic balance with pressure provided by the energy released by accreted planetesimals. This hydrostatic balance prevents the planet from accreting any appreciable amount of gas. As found in Ikoma, Nakazawa & Emori (2000), the envelope is no longer in hydrostatic balance when the mass of the core exceeds,

$$M_{c,crit} \simeq 2\,M_{\oplus}\left(\frac{1}{10^{-6}M_{\oplus}\ \mathrm{yr}^{-1}}\frac{dM_p}{dt}\right)^{1/4} . \tag{2.43}$$

where we have not included the dependence of $M_{c,crit}$ on the envelope opacity. This chosen parameterization is not unique, but rather corresponds to a low envelope opacity of $10^{-4} - 10^{-3}$ cm^2 g^{-1}. When the planet's mass exceeds $M_{c,crit}$, it is able to start accreting appreciable amounts of gas from the disk (Ida & Lin, 2004). The planet continues to accrete planetesimals, albeit at a reduced rate, as its inward migration continues to replenish its feeding zone (Alibert et al., 2005).

We assume that the availability of solids is reduced after the oligarchic growth stage takes place, and change the solid surface density to be that which coincides with the dust to gas ratio from the chemistry calculation, $\Sigma_d = 0.01\Sigma$. Solid accretion is still governed by the timescale in equation 2.41, albeit at a reduced rate due to the lower dust to gas ratio. Growth of the planet is now dominated by accretion of gases, governed by the Kelvin-Helmholtz timescale, given by (Ikoma et al., 2000),

$$\tau_{KH} \simeq 10^{c}\,\mathrm{yr}\left(\frac{M_p}{M_{\oplus}}\right)^{-d} . \tag{2.44}$$

where $c = 9$ and $d = 3$ are parameters that depend on the planet's envelope opacity (Ikoma et al., 2000). We note that, in contrast to equation 2.43, the Kelvin-Helmholtz parameters chosen correspond to larger envelope opacity values of 0.1-1 cm^2 g^{-1}. While the envelope opacity, which itself is uncertain, links the parameterization of the critical core mass and Kelvin-Helmholtz timescale, previous works have treated these as independent parameters (Ida & Lin, 2008; Hasegawa & Pudritz, 2012, 2013), similar to the model presented here.[1] The gas accretion rate is then given by,

$$\frac{dM_p}{dt} \simeq \frac{M_p}{\tau_{KH}} . \tag{2.45}$$

We note that our model does not consider the enrichment of the planet's atmosphere due to impacting planetesimals, which is expected to be an important process when considering the atmospheric composition of super Earths or Neptunes (Fortney et al., 2013). Instead, our model assumes gas accretion is solely due to direct accretion from the disk. It is unclear, however, how large of an effect impacting planetesimals will have on gas abundances in Jovian planets' atmospheres.

Initially, when the planet's mass has just increased beyond $M_{c,crit}$, the timescale for gas accretion is long ($\sim 10^6$ years). This stage of slow gas accretion will be referred to as stage II. As the mass of the planet increases, it eventually will become large enough that it will be accreting gas at a fast enough rate such that its atmosphere will no longer be pressure supported, giving rise to an instability. When this occurs, the atmosphere collapses and the planet rapidly accretes its atmosphere. Quantitatively, this takes place when $\tau_{KH} < 10^5$ years. This segment of the formation process is referred to as runaway growth, and will be denoted as stage III.

Throughout the early phases of slow gas accretion, the planet remains in the trapped type-I migration regime (see discussion in section 2.3 and Appendix A). As the planet increases its mass, it exerts an increasingly large torque on the disk, eventually leading to the formation of an annular gap. Gap formation liberates the planet from the trap it was forming within. To estimate the mass at which a planet opens up a gap, two arguments can be used. The first is that the planet's torque on the disk must be greater than the torque that disk viscosity can provide. Otherwise, the disk's viscosity will suppress gap formation. The second argument is that the planet's Hill sphere must be larger than the disk's pressure scale height, or else disk pressure will prevent a gap from opening. This critical mass is referred to as the gap-opening mass, and is given by Matsumura & Pudritz (2006),

$$M_{\rm GAP} = M_* \min\left[3h^2(r_p), \sqrt{40\alpha h^5(r_p)}\right] , \tag{2.46}$$

[1] In a future population synthesis paper, we will restrict our parameterizations of $M_{c,crit}$ and τ_{KH} to be self-consistent in terms of envelope opacity, which will reduce our model's parameter set by two. We note that gas accretion timescales will have small effects on our super Earth masses and compositions, and thus will not affect the main conclusions of this work.

where r_p is the radius of the planet, and $h(r_p) = H_p/r_p$. During the phase where the planet is forming within a gap in the disk, the planet's migration is referred to as type-II migration. We note that our gap-opening criteria predicts the planet to be in the type-II migration regime once it overcomes the gap-suppressing effect of either disk thermal pressure or viscosity, considered independently of one-another. This causes our predicted M_{GAP} values to be smaller than the model shown in Crida, Morbidelli & Masset (2006), which considers both gap-suppressing effects simultaneously.

Once a planet opens a gap in its natal disk, the migration rate of the planet is governed by the accretion timescale of the disk material onto the star ($\sim 10^6$ years). In this regime, the planet migrates inwards with velocity,

$$v_{\rm mig,II} \simeq -\frac{\nu}{r} \; . \tag{2.47}$$

When the planet reaches a critical mass (Ivanov, Papaloizou & Polnarev, 1999),

$$M_{\rm crit} = \pi r_p^2 \Sigma_g(r_p) \; , \tag{2.48}$$

it will be massive enough that its inertia will resist inward migration occurring with the evolution of the disk (Hasegawa & Pudritz, 2012; Hellary & Nelson, 2012). In this regime, the migration velocity is,

$$v_{\rm mig,slowII} \simeq -\frac{\nu}{r(1 + M_p/M_{\rm crit})} \; . \tag{2.49}$$

Typically, type-II migration applies to planets midway through stage II of their formation, while slowed type-II migration applies to planets in the late phases of stage II and throughout stage III in our models.

The last critical mass in our core accretion model is one that acts as an upper limit to how massive a planet will become. We scale a planet's maximum mass with its gap opening mass as follows (Hasegawa & Pudritz, 2013),

$$M_{\rm MAX} = f_{\rm MAX} M_{\rm GAP} \; , \tag{2.50}$$

with $f_{\rm MAX}$ being the parameter that expresses the ratio between a planet's final mass and the mass at which it opened a gap. Previous works have shown that accretion onto a planet slows and eventually terminates after a planet opens a gap in the disk (Lissauer et al., 2009). However, flow onto the planet does not terminate immediately when a gap is opened in the disk. Numerical works have shown that a substantial amount of disk material can flow through the gap and be accreted by the planet (Lubow, Seibert & Artymowicz, 1999; Lubow & D'Angelo, 2006). The parameterization shown in equation 2.50 acknowledges gap opening as a key stage in terminating the accretion onto a planet, linking the planet's final mass with that at which it opens a gap.

Motivated by this, we use the parameterization given equation 2.46 to estimate the mass reservoir that planets can accrete from post-gap formation in our model. Typically f_{MAX} is in the range of 10 to 100, with an f_{MAX} of 10 producing Jovian planets of mass comparable to Jupiter (Hasegawa & Pudritz, 2013). Planets with f_{MAX} outside this range are also possible, as an $f_{\mathrm{MAX}} \simeq 1$ would produce a planet whose accretion is sharply truncated when it opens a gap. Alternatively, an f_{MAX} of several hundred would represent a planet whose accretion is driven long after it opens up a gap. This scenario has been shown to be possible if the disk possesses sufficient viscosity (Kley, 1999) or if the planet can excite spiral density waves giving rise to an eccentric disk (Kley & Dirksen, 2006).

Other works, such as Machida et al. (2010), Dittkrist et al. (2014), and Bitsch et al. (2015) use a disk-limited accretion phase to model the growth of planets in the mass range of $\gtrsim 30$ $\mathrm{M}_{\oplus}$. In these models gas accretion onto a planet post-gap formation is limited by the local supply of material from the disk. With such a model, the accretion rate of gas onto a planet decreases with time after gap formation occurs, in agreement with results found in hydrodynamic simulations such as Lubow et al. (1999).

Conversely, our work only considers the Kelvin-Helmholtz timescale for gas accretion at all planet masses (from stage II onward) until the planet reaches its maximum mass given by equation 2.50. This approach is limited as it produces accretion rates that increase with planet mass even after gap formation has taken place, contrary to results of hydrodynamic simulations. While our step-function model of accretion onto high mass planets is a simplistic treatment of a continuous process controlled by planet and disk properties, it has been shown in Hasegawa & Pudritz (2013) to produce planet populations in agreement with observations. Additionally, in both the Kelvin-Helmholtz and disk-limited accretion methods, accretion onto high mass planets is sensitive to the planets' envelope opacities (Hasegawa & Pudritz, 2014; Mordasini et al., 2014). Depending on the particular envelope opacity that is used, both methods can produce similar mass-period and core mass-envelope mass distributions.

Further study of the late stages of planet formation in our model will be the subject of future

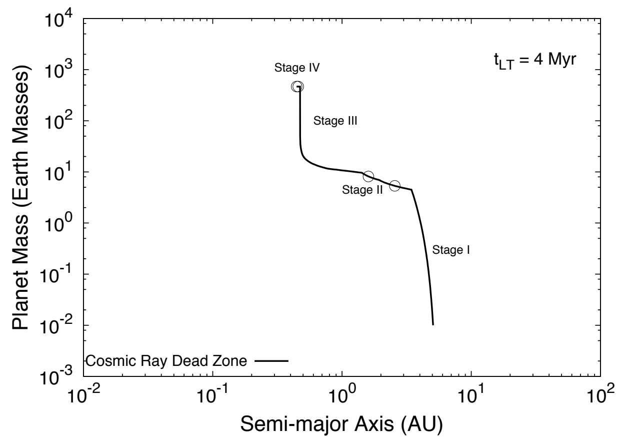

Figure 2.7: An example formation track for a planet forming in our model within the cosmic ray dead zone trap in a fiducial disk (equation 2.22). Open circles along the track represent 1 Myr time markers. Oligarchic growth (stage I) takes place in $\sim 10^6$ years, which is shorter than the migration timescale causing the planet to move nearly vertically in this diagram. Stage II of the planets formation takes $\simeq 2$ Myr for this planet, causing it to move more horizontally as slow gas accretion takes place. Runaway growth (stage III) takes place in $< \ 10^5$ years until gas accretion is terminated as the planet reaches its maximum mass. The planet undergoes slow type-II migration in stage IV until the disk photoevaporates at 4 Myr, giving a final planet mass of 1.56 Jupiter masses and semimajor axis of 0.65 AU.

work (Alessi & Pudritz 2016, in preparation). Here, we adopt a fiducial value of $f_{\rm MAX} = 50$, as this value results in Jovian planet masses that give an average fit to masses of giant exoplanets. After the planet has reached its maximum, or final mass, accretion is terminated. From this time onward, the planet will undergo slowed type-II migration until the disk photoevaporates at $t = t_{LT}$. We refer to this final stage of terminated accretion as stage IV.

In Figure 2.7 we show the resulting formation track for a planet forming within the dead zone trap caused by cosmic ray ionization in a disk with initial mass $0.1\text{M}_\odot$. The figure outlines the four stages, and by plotting the planet's mass as a function of its semimajor axis throughout formation, accretion and migration timescales can easily be compared. In oligarchic growth (stage I) the planet builds up its solid core in a short timescale of $\lesssim 10^6$ years, accreting a few $\text{M}_\oplus$ of solids while its trapped inward migration allows it to only move radially roughly 1 AU. The timescale to build the core is significantly shorter than the disk lifetime, which is 4 Myr in this case.

As the core mass reaches a few $\text{M}_\oplus$ the solids in the planet's feeding zone have been depleted and its main accretion source becomes the gas and dust in the disk. Initially, gas accretion takes place slowly in stage II, and the evolution of the cosmic ray dead zone trap causes the planet to migrate appreciably as it accretes its atmosphere. Midway through stage II, the planet's mass exceeds the gap opening criterion, whereby the planet is no longer trapped and begins to undergo type-II migration. The timescale for stage II is roughly 2 Myr in this case, which is significantly longer than the oligarchic growth timescale. We emphasize that the timescale for slow gas accretion is comparable to disk lifetimes for planets forming in our model. As the planet enters stage III, runaway growth proceeds, whereby the planet rapidly accretes gas and reaches its maximum mass in less than 10^5 years. Runaway growth allows the planet to satisfy the mass criterion for slowed type II migration. This allows it to migrate inwards on a timescale longer than the disk's viscous timescale during stage IV after accretion has been terminated. Thus, the planet does not migrate inwards appreciably for the remaining 1-2 Myr of the disk material being present, prior to photoevaporation taking place. The end of the disk's lifetime marks the final mass and semimajor axis of the planet.

We emphasize that the disk lifetime sets an upper limit to the time that the planet formation process can take. Planets that have a formation time which is less than the disk lifetime are able to reach their maximum mass defined in equation 2.50. For the alternate scenario, planet accretion and migration ceases at the disk lifetime as the disk material is no longer present. Depending on the timing of disk dispersal, planets can be stranded during stages I, II or III of their formation. Since the timescale for stage II to take place is much longer than stages I or III, it is much more probable that a planet will be stranded in stage II than other stages of formation. Comparing with figure 2.7, stranding a planet during stage II would result in a planet with mass consistent with a super Earth or mini Neptune.

During our planet formation runs, we use the disk's abundance at the planet's current location to characterize the abundance of the material accreted onto the planet. In doing so, we assume that planets are sampling the disk's local abundance throughout their formation. We present a detailed algorithm describing our process of tracking planets' compositions throughout their formation in Appendix B.

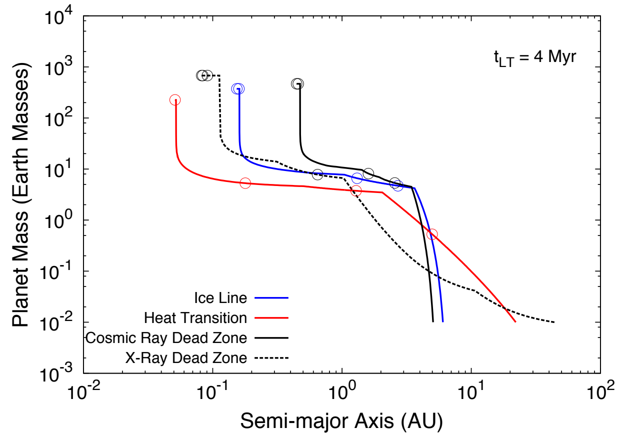

Figure 2.8: Formation tracks for planets forming within each of the traps in a fiducial disk with a 4 Myr lifetime. Open circles along the tracks represent time stamps at 1 Myr intervals. The disk lifetime is sufficiently long for all four planets to complete stage III of their formation, resulting in four Jovian planets with distinct semimajor axes.

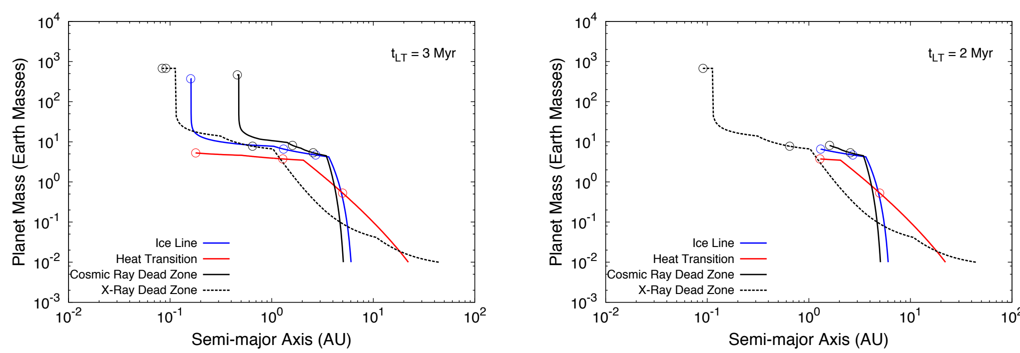

Figure 2.9: Here we plot planet formation tracks in each of the four traps in a fiducial disk (0.1 $M_{\odot}$ initial mass) with reduced disk lifetimes. In the left panel, $t_{LT} = 3$ Myr, and this set up results in the heat transition trap producing a super Earth. In the right panel, $t_{LT} = 2$ Myr, and planets forming ice line, cosmic ray dead zone, and heat transition traps are all super Earths. Only the planet forming in the X-ray dead zone trap, which has the shortest formation timescale, produces a Jupiter-mass planet in both cases.

2.3 Results

2.3.1 Dependence of Planet Evolutionary Tracks on Disk Lifetime

Figure 2.8 shows evolutionary tracks for planets forming within each of the traps in our model, in a 0.1 $M_\odot$ disk with a 4 Myr lifetime. This disk is sufficiently long-lived for Jovian planets to result from planet formation in all of the traps. The cosmic ray dead zone planet formation track is the same track that was presented in figure 2.7. We now compare accretion and migration timescales for planets forming in all four of the traps by contrasting the shapes of the evolutionary tracks on this diagram.

The formation tracks pertaining to the ice line and cosmic ray dead zone traps appear similar due to the traps themselves occupying nearby regions of the disk. The resulting planets, however, have substantial differences in their semimajor axes, with the cosmic ray dead zone producing a 0.45 AU gas giant while the ice line gives rise to a warm gas giant at 0.15 AU in this case. The difference in the final semimajor axes of these two planets is caused by the ice line's inward migration occurring on a shorter timescale than the inward migration of the cosmic ray dead zone.

The heat transition is shown to produce a hot Jupiter in the 4 Myr-lived disk, as is shown in figure 2.8. The trap itself migrates inwards the fastest out of the three traps. Also, due to the trap being the farthest out in the disk, the planet forming within this trap is in a region with the smallest surface density of solids among these three planets. This causes the planet forming in the heat transition to have a small accretion rate during stage I, so the resulting timescale for stage I of formation is $\sim$ 2 Myr. These factors cause the planet to have a significantly lower mass at the beginning of gas accretion compared to the other tracks, causing the timescale for slow gas accretion to be longest ($\gtrsim$ 1.5 Myr) in the heat transition. This long timescale causes the planet to migrate inwards past 0.1 AU prior to runaway growth taking place, and the planet resulting from formation within the heat transition is a hot Jupiter.

Lastly, the planet forming within the X-ray dead zone trap starts the farthest out in the disk. However, due to the X-ray dead zone's rapid inward migration (see figure 2.6), the planet migrates within an AU prior to 1 Myr into the disk's lifetime. This allows the planet to build its solid core in a region with a large amount of solids, completing stage I of its formation in $\lesssim 10^6$ years. With such a high accretion rate of planetesimals, its mass at the beginning of stage II is the largest among any of the four planets shown in figure 2.8. Due to this, gas accretion takes place quickly when compared with the other formed planets. The planet reaches its maximum mass prior to the 2 Myr mark, showing that the X-ray dead zone lends itself to forming planets the fastest out of all the traps in our model.

Figure 2.9 shows one of the key issues this paper addresses; namely, how do super Earths form? Specifically, we show the effects of decreasing the disk lifetime by plotting the same tracks as shown in figure 2.8, but in disks that get photoevaporated after 3 Myr (top) or 2 Myr (bottom). In the case of a 3 Myr disk, the planets forming in the ice line and both dead zone traps remain unaffected as their formation is complete prior to the disk lifetime. However, the planet forming within the heat transition is still in its slow gas accretion phase at the point of disk dispersal and gets stranded with a mass of 5.4 $M_\oplus$ at roughly 0.2 AU, resulting in a super Earth.

In the case of a disk with a lifetime of 2 Myr (figure 2.9, lower panel), we find that planets forming in the ice line, cosmic ray dead zone, and heat transition traps become stranded in their slow gas accretion phase of formation at the time of disk dispersal. Planet formation in each of these three traps in this short-lived disk result in failed cores at roughly 1 AU. The heat transition produces a super Earth with a mass of 4 $M_\oplus$, and the ice line and cosmic ray dead zone traps produce planets with masses of roughly 10 $M_\oplus$. Conversely, the planet forming in the X-ray dead zone has a formation timescale of less than 2 Myr, so its formation completes prior to disk dispersal, and is again unaffected by the shorter disk lifetime. The X-ray dead zone is the only trap in our model that produces a Jovian planet in a 2 Myr-lived disk.

2.3.2 Dependence of Planet Evolutionary Tracks on Disk Mass

Up to this point, we have focused only on the variation of the disk's lifetime, and how small values of t_{LT} can lead to super Earth and hot Neptune formation. The disk's mass is another key parameter in our model that has been shown by Ida & Lin (2004), Mordasini et al. (2012a), & Hasegawa & Pudritz (2013) to play a key role in shaping the mass period relation of exoplanets.

We chose an initial disk mass of 0.1 $M_\odot$ as a fiducial value, and we now vary this initial disk mass in order to determine the effect on resulting planet masses and final locations. In figure 2.10, we plot planet tracks from each of the four traps in our model that are computed in disks with initial masses of 0.05 $M_\odot$, 0.1 $M_\odot$, and 0.15 $M_\odot$. We hold the disk lifetime at a constant value of 4 Myr as this value resulted in all four traps producing a gas giant in a fiducial mass disk (see figure 2.8).

In figure 2.10 we see that traps move out to larger radii as the disk mass increases. This causes the planets to begin their formation farther from their host stars. In all four traps, planet formation in a more massive disk (0.15 $M_\odot$) takes place on a shorter timescale, and results in more massive planets orbiting at larger semimajor axes than the fiducial disk mass produces. Conversely, smaller disk masses result in lower mass planets forming at smaller separations from their host stars. Additionally, planet formation takes longer as the disk mass decreases. This is shown in figure 2.10, as the ice line and cosmic ray dead zone traps produce super Earths in the 0.05 $M_\odot$ disk mass case, showing that the planet formation timescale increased beyond the 4 Myr disk lifetime in both traps. The results are consistent with those presented in Hasegawa & Pudritz (2011, 2012).

In figure 2.10, we find that the ice line and cosmic ray dead zone traps are the most sensitive to the initial disk mass. Variation of this parameter from 0.05 to 0.1 to 0.15 $M_\odot$ causes these two traps to produce planets of entirely different classes. In particular, we find that the two traps produce 1 AU Jupiters in the heaviest disks, warm Jupiters in the fiducial case, and super Earths in the lightest disks. The X-ray dead zone and heat transition traps, on the other hand, are insensitive to the particular disk mass used. While it remains true for these two traps that the planet formation timescale increases for smaller disk masses, a disk lifetime of 4 Myr still produced gas giants in both traps, even in the lightest disks considered. Moreover, the final locations of planets that result from the X-ray dead zone and heat transition occupy a small region on the mass-semimajor axis diagram. Both traps produce hot Jupiters in all cases considered, and the final masses and locations of the planets do not depend heavily on the initial disk mass used.

2.3.3 Super Earth Abundances

In figure 2.11, we show the solid composition of the super Earth produced in the heat transition in the t_{LT} = 3 Myr disk (see figure 2.9, top panel, for the planet's formation track). The left panel shows how this planet's solid mass is distributed among core materials, mantle materials, and ice. Since the heat transition trap lies exterior to the ice line for the majority of the disk's lifetime, the super Earth spends the majority of its time accreting solids in an ice-rich environment. This leads to the planet accreting a substantial amount of ice (36% of its mass) prior to the time of disk dispersal. Because the planet migrates throughout its formation, it samples disk chemistry over a range of disk radii. Therefore, its final composition does not correspond to that of any single radius in the disk.

Figure 2.11 also shows how the 3 Myr heat transition planet's mass is distributed among specific solids in the chemistry model. In addition to having over one third of its solid mass in ice, there

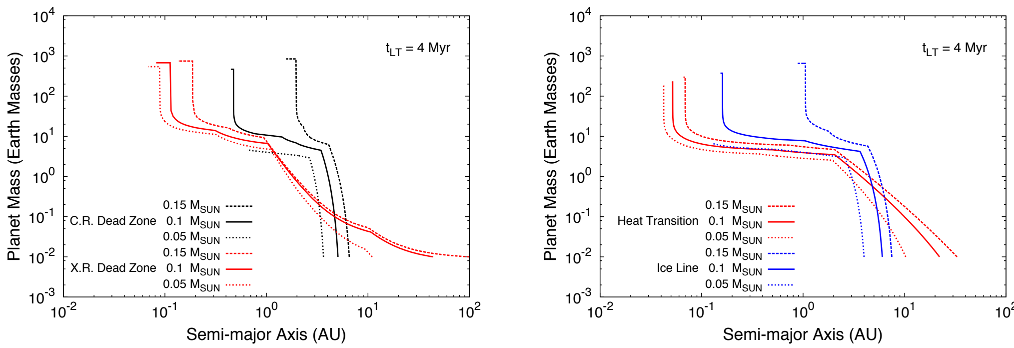

Figure 2.10: Planet formation tracks are shown within each of the four traps while the initial disk masses are varied. Initial masses considered are 0.05 $M_\odot$, 0.1$M_\odot$, and 0.15 $M_\odot$. We find that the heat transition and X-ray dead zone traps are the least sensitive to the disk's mass, producing planets of similar masses and final locations in all three cases. Conversely, the cosmic ray dead zone and ice line traps are quite sensitive to this parameter. Both traps produce super Earths in the case of the 0.05 $M_\odot$ disk.

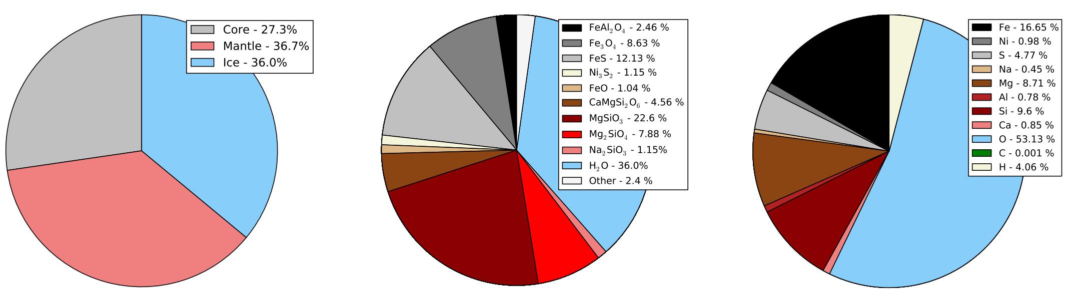

Figure 2.11: **Left**: The mass distribution among solid components for the super Earth formed in the heat transition in the $t_{LT} = 3$ Myr run (figure 2.9, top panel), with final mass 5.4 $M_\oplus$ and semimajor axis of roughly 0.2 AU. Since the planet accretes solids primarily exterior to the ice line, it has a substantial mass fraction in ice. **Middle**: Mass fractions in individual solids are plotted for the same planet. The first five materials in the legend are classified as core materials. The next four are considered mantle materials. Water ice shows the same abundances in both plots as it is the only ice considered in our chemical model. All solids that had a mass fraction of < 1 % on the planet were binned as other on the pie chart. **Right**: Mass fractions in individual elements are shown for this planet.

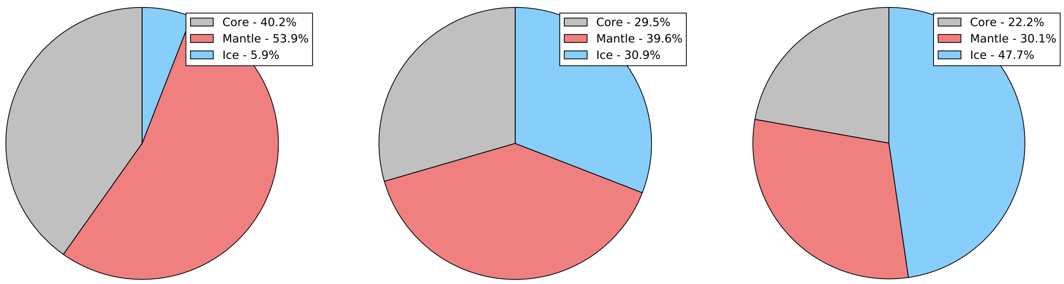

Figure 2.12: Solid mass abundances among solid components for the super Earths formed in the simulation with $t_{LT} = 2$ Myr, shown in figure 2.9 (bottom). The dead zone planet (left) is quite dry as it forms interior to the ice line, while the ice line (middle) and heat transition (right) planets have accreted a substantial mass in ice as they form in colder regions of the disk.

are several other core and mantle refractories that comprise a large fraction of the planet's solid mass. The planet's core material component is dominated by mass in troilite (FeS) and magnetite (Fe_3O_4), while the major silicates that have been accreted onto this planet are enstatite ($MgSiO_3$) and forsterite (Mg_2SiO_4).

Lastly, the right panel of figure 2.11 shows the elemental abundances of this super Earth's solid component. We find the planet is very enriched in oxygen compared to Solar abundances. The large oxygen content mainly results from the abundant amount of ice the planet has accreted. Iron and sulphur comprise the majority of the planet's content in core materials, while magnesium and silicon make up its mass in mantle materials. We also find that the planet has a negligible amount of carbon in its solid component. This is consistent with Bond et al. (2010), who found little carbon content among terrestrial planets forming in disks with C/O ratios similar to the Solar value of 0.54.

Bond et al. (2010) found that substantial amounts of graphite can form along the midplane only in disks with C/O ratios over 2 times the Solar value, leading to an appreciable fraction of planets' solid masses being comprised of graphite. Our disk model, conversely, uses a Solar C/O ratio, leading to negligible amounts of graphite forming along the disk midplane. Because of this, our planet formation models result in very small C/O ratios in the solid components of super Earths.

By tracking solids accreted onto the three super Earths formed in the 2 Myr disk (see figure 2.9, lower panel, for formation tracks), we can compare solid abundances that arise from super Earth formation within the ice line, cosmic ray dead zone, and heat transition.

In figure 2.12, we show how each planet's solid mass is distributed among solid components at the end of their formation. The cosmic ray dead zone planet has the lowest ice content among the three planets shown (6 % ice by mass) as it spends the majority of its time accreting solids interior to the ice line, acquiring most of its mass in refractory materials. It is only at late stages of its formation that the planet is situated close to the ice line, and is able to accrete a small amount of icy solids. By definition of the trap, the planet forming within the ice line is able to accrete a substantial amount of icy solids during its formation. At the end of its formation, the planet formed in this trap has roughly one third of its solid mass in ices. Lastly, as the planet formed in the heat transition lies exterior to the ice line, it is able to accrete a lot of icy solids, resulting in nearly half of its solid mass being ice. We do not show pie charts of abundances for the super Earths formed in the 0.05 $M_{\oplus}$ case, as the abundances are consistent with the super Earths formed in the cosmic ray dead zone and ice line shown in figure 2.12.

Migration Across the Ice Line: A Means of Achieving Time-Dependent Composition

By comparing the composition of the heat transition planet at 2 Myr (figure 2.12, right) and at 3 Myr (figure 2.11), the effects of time dependent chemistry can be seen as the planet's composition changes over the last Myr of its formation. In particular, we see that after 2 Myr the planet has nearly half its solid mass in ice, and after 3 Myr it has decreased to roughly one third. In order to connect these two snapshots, we plot the continuous solid abundances of the planet during its formation in figure 2.13. Compositional changes are expected in planets that encounter compositional gradients throughout the disk during their formation. The most recognizable compositional gradient in protoplanetary disks is the ice line, and this has a direct effect on the ice content in solids that a planet can accrete. The location of a trap (in this case, the heat transition) with respect to the ice line dictates the types of material available for formation. Interior to the ice line, there are few icy solids available for accretion, while outside they are in abundance.

In the case of figure 2.13, the heat transition trap intersects the ice line at roughly 2 Myr (see figure 2.6), and the planet forming within the heat transition encounters a steep compositional gradient, causing a decrease in its ice abundance. Prior to the 2 Myr point, it accretes in an ice rich environment, building up nearly half its solid mass in ice. After the traps intersect, the planet transitions to an ice deficient environment interior to the ice line. Solid accretion in this dry region of the disk results in only refractories being accreted. This results in the ice abundance decreasing from 47.7 % to 36 % between 2 and 3 Myr. In turn, the mass abundances of core materials and mantle materials increase during this period.

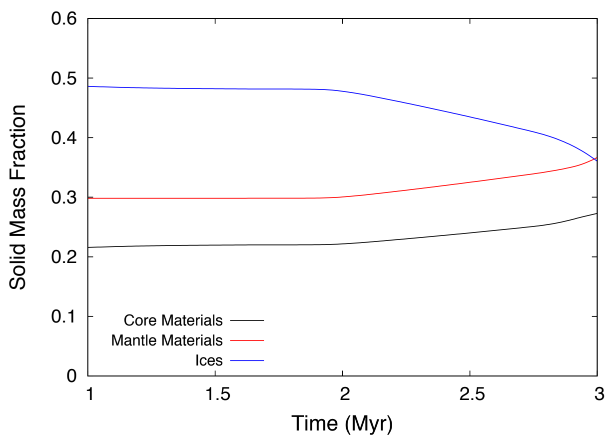

Figure 2.13: The time dependent mass fraction in solid components for the planet forming in the heat transition. We connect the compositions at 2 and 3 Myr (shown in figures 2.12 bottom, and figure 2.11, respectively) by tracking the mass fractions between these two times. Since the heat transition lies interior to the ice line after 2 Myr, the planet spends the last Myr of its formation accreting dry refractory materials.

Comparing Cosmic Ray and X-ray Dead Zone Results

While the X-ray dead zone does not form a super Earth in any of the simulations presented, the time marker in figures 2.8 and 2.9 indicate that a disk that is photoevaporated after only 1 Myr will result in the X-ray dead zone producing a super Earth of mass 7.8 $M_\oplus$ at 0.65 AU. While a 1 Myr disk lifetime is short compared to the fiducial value of 3 Myr discussed earlier, it is not entirely unreasonable as it lies within the 0.5-10 Myr range of estimated disk lifetimes as suggested by observations (Hernández et al., 2007; Mamajek, 2009). Other theoretical models (Hasegawa & Pudritz, 2013) have used a $t_{LT} \sim 1$ Myr as a lower limit to a range of disk lifetimes in core accretion scenarios.

In Figure 2.14, upper panel, we show the mass abundance of the 1 Myr X-ray dead zone planet in solid components. We see that the planet is very dry at this point in its formation, with only 1 % of its solid mass being in ice. The X-ray dead zone intersects the ice line early in the fiducial disk's lifetime, at roughly 0.7 Myr. As previously noted, a planet forming within a trap that sweeps past the ice line will have an evolving composition during its formation. We therefore expect the planet forming within the X-ray dead zone to have a time-dependent solid composition over the first Myr of its formation.

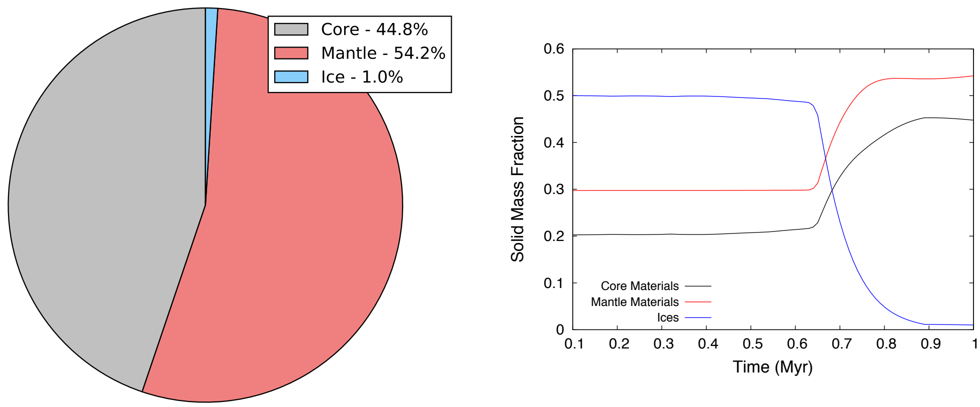

Figure 2.14: **Left**: The solid abundances of the planet forming within the X-ray dead zone are shown 1 Myr into its formation. At this time, its mass is 7.8 $M_\oplus$, consistent with a super Earth. It is very dry at this time in its formation, suggesting it accreted most of its solids interior to the ice line. **Right**: By plotting the time dependent abundances of the three solid components on this planet, we see that the planet started out accreting in an icy environment (outside the ice line), prior to migrating inwards, and accreting only dry, rocky materials.

In figure 2.14 (lower panel), we show the time dependent mass abundance of the planet forming in the X-ray dead zone from the start of its formation (0.1 Myr) to the 1 Myr point where its mass is consistent with a super Earth. We find that the planet initially accretes icy solids, having a substantial mass abundance in ice of nearly 50 % before decreasing drastically at 0.7 Myr to only 1 %. At this time the X-ray dead zone sweeps past the ice line, leaving the planet to accrete from dry regions of the disk, resulting in the decreasing ice abundance on the planet.

The small ice abundance of 1 % on this planet suggests that it must have accreted much more solids inside the ice line than early in its formation when it was outside the ice line. We can confirm this by noting the solid accretion rate onto a planet is proportional to the planet's mass, with the scaling $\dot{M}_p \propto M_p^{2/3}$, as is shown in equations 2.41 and 2.42. This causes the planet forming in the X-ray dead zone to accrete solids faster in the later stages of its formation (interior to the ice line) than in early stages of its formation (outside the ice line). Thus, the total mass accreted in the dry regions of the disk between 0.7 Myr and 1 Myr greatly exceeds the mass accreted before 0.7 Myr in the icy regions of the disk. This causes the mass in ice that the planet was able to accrete early in its formation to comprise only a small fraction of 1 % of the planet's total mass after 1 Myr.

Contrasting the X-ray dead zone planet's composition after 1 Myr with the super Earth formed in the cosmic ray dead zone (Figure 2.12, left panel), we see that the cosmic ray ionization model results in a super Earth with 6 % of its mass in ices as opposed to 1 % in the case of the planet

Table 2.6: Abundances in specific minerals for the five super Earths whose solid abundances are shown in this results section. In the top row, we note the trap the planets formed within as well as the lifetimes of their natal disks. The upper portion of the table gives mass abundances for the top three iron minerals and the top three silicate minerals, calculated with equation 2.60. The lower portion normalizes these mass abundances in terms of the planet's total mass in core materials (for the 3 iron minerals, using equation 2.51) or mantle materials (for the 3 silicate minerals, using equation 2.52).

Planet: Disk t_{LT} & Trap	3 Myr HT	2 Myr HT	2 Myr CRDZ	2 Myr IL	1 Myr XRDZ
Figure	2.11	2.12 right	2.12 left	2.12 middle	2.14
% of planet's solid mass					
Troilite (FeS)	12.13	9.88	17.66	12.83	19.01
Magnetite (Fe_3O_4)	8.63	8.1	16.44	11.88	3.97
Hercynite ($FeAl_2O_4$)	2.46	2.06	3.72	2.72	3.76
Enstatite ($MgSiO_3$)	22.61	19.86	35.71	26.2	24.14
Forsterite (Mg_2SiO_4)	7.88	5.45	9.88	7.2	20.21
Diopside ($CaMgSi_2O_6$)	4.56	3.71	6.74	4.93	7.16
Mass relative to planet's mass in core materials					
Troilite (FeS)	0.44	0.45	0.44	0.44	0.42
Magnetite (Fe_3O_4)	0.32	0.37	0.41	0.40	0.09
Hercynite ($FeAl_2O_4$)	0.09	0.09	0.09	0.09	0.08
Mass relative to planet's mass in mantle materials					
Enstatite ($MgSiO_3$)	0.62	0.66	0.66	0.66	0.45
Forsterite (Mg_2SiO_4)	0.22	0.18	0.18	0.18	0.37
Diopside ($CaMgSi_2O_6$)	0.12	0.12	0.13	0.12	0.13

formed in the X-ray ionized model.

The differences can be explained by considering the difference in locations of the two traps. While the cosmic ray dead zone always lies interior to the ice line, it is always within 1 AU of it. While the planets forming in the cosmic ray dead zone are dry, they are still able to accrete a small amount of ice due to the trap's proximity to the ice line. Conversely, the X-ray dead zone lies drastically interior to the ice line, except for the first 0.7 Myr. This causes planets forming within this trap to accrete effectively no ice while forming in the dry regions of the disk.

Super Earth Mineral Abundances

In Table 2.6, we show abundances of the top three iron and silicate minerals for the five super Earth examples from our model discussed in this section. In the top portion of this table, we show solid abundances of each mineral that were calculated using equation 2.60 on each planet. While the raw abundances show what minerals dominate the planet's solid mass, we note that these quantities are heavily dependent on each planet's mass in core minerals and mantle minerals. For example, a dry planet with little water will naturally have large abundances of core and mantle minerals, as is the case for the super Earths formed in the dead zone traps. Conversely, the planets that formed in the heat transition and ice line traps have systematically lower abundances of these minerals due to the high ice content on the planets.

To remove the systematic variation in mineral abundances with each planet's total water content, we normalize the mineral abundances in the following manner. For each iron mineral, we compute its relative abundance with respect to the planet's total mass in core materials,

$$\text{Abundance of } i \text{ relative to core} = \frac{X^{\text{solid}}_{\text{i, planet}}}{X^{\text{solid}}_{\text{core, planet}}} \,. \tag{2.51}$$

A similar approach is taken to normalize the mantle minerals,

$$\text{Abundance of } i \text{ relative to mantle} = \frac{X^{\text{solid}}_{\text{i, planet}}}{X^{\text{solid}}_{\text{mantle, planet}}} \,. \tag{2.52}$$

By normalizing the abundances in this manner, we can discern how much a particular mineral contributes to the total mass of the planet's core (or mantle).

In the lower portion of Table 2.6, abundances of the dominating iron and silicate minerals are shown relative to the planet's total mass in core minerals or mantle minerals. As an example, we see that troilite (FeS) contributes roughly 43-44 % of each super Earth's mass in core materials, regardless of the trap each particular planet formed within. Therefore, when considering our 3-component chemistry model (core materials, mantle materials, & ice), we can conclude (albeit with a small sample of five super Earths) that each planet's iron content is composed of roughly 43-44 % in troilite. Aside from the planet formed in the X-ray dead zone, the other minerals follow a similar trend across the planets, as each mineral comprises a similar fraction of their corresponding planet's iron (or silicate) content. Unlike the case of troilite, however, there is a variation of $\sim$10% in some cases in the abundances of a particular mineral on different planets.

Table 2.6 shows that the super Earth formed in the X-ray dead zone has mineral abundances that differ greatly from the other four planets shown. This is due to the fact that the X-ray dead zone planet forms early in the disk's evolution, and accretes all its solids prior to 1 Myr. This, coupled with its orbital migration to the inner regions of the disk ($<$ 1 AU) causes it to sample disk chemistry at higher temperatures than the other four planets shown. The X-ray DZ planet shows that we cannot simply assume a constant fraction of enstatite, for example, in the planet's silicate content. In this way, binning our solids into core and silicate components hides the ratios of the underlying minerals. While the three-component chemistry model does provide a simple description of the planet's composition giving the necessary density information for modelling its interior structure (as in Valencia et al. (2007)), it is important to realize that each planet's unique formation history results in different abundances of particular minerals that are hidden when quoting compositions in terms of the summed components.

2.4 Discussion

2.4.1 Observational Constraints on Disk Chemistry

One method of constraining our chemistry results is via the use of observed locations of condensation fronts. For example, in Zhang et al. (2013) the location of the ice line in TW Hya was shown to have an upper limit of 4.2 AU using the observed water vapour content throughout the disk. Additionally, they found that the water vapour content drops rapidly at the location of the ice line, over a short distance of 0.5 AU. The ice line location found in our work falls within their constrained regime, as do the sharp transitions between water vapour and ice profiles we find at the ice line in our model.

Table 2.7: Mass abundances of secondary gases in atmospheres of Jovian planets formed in the t_{LT} = 4 Myr run (see figure 2.8). Each column denotes the natal trap of a particular planet. The second row shows the planet's final masses. Planets that accreted their gas in cooler regions of the disk, such as the planet formed in the cosmic ray dead zone, have larger abundances of H_2O, CH_4, and NH_3. Conversely, gas accretion from hot regions of the disk, as is the case for the planet formed in the X-ray dead zone, results in larger abundances of CO, N_2, and SiO.

	Ice Line	Heat Transition	Cosmic Ray Dead Zone	X-ray Dead Zone
$M_P/M_{Jupiter}$	1.17	0.71	1.47	2.13
H_2O	0.352 %	0.163 %	0.446 %	0.26 %
CO	0.183 %	0.485 %	0 %	0.484 %
CH_4	0.169 %	6.15×10^{-4} %	0.279 %	1.54×10^{-4} %
N_2	8.19×10^{-2} %	8.24×10^{-2} %	4.56×10^{-2} %	8.22×10^{-2} %
NH_3	7.42×10^{-4} %	1.47×10^{-4} %	4.52×10^{-2} %	2.47×10^{-7} %
H_2S	1.51×10^{-2} %	3.79×10^{-2} %	6.62×10^{-8} %	2.59×10^{-2} %
SiO	0 %	7.27×10^{-5} %	0 %	0.103 %

In addition to the water ice line, the CO condensation front has been observed in disks at roughly 30 AU (Qi et al., 2011). Our equilibrium chemistry model does not predict the existence of carbon monoxide in solid or gas phase in the outer regions of the disk and cannot predict the location of the condensation front, which is a limitation of the model. We note, however, that the inclusion of a CO ice line in this model would not greatly affect the resulting super Earth compositions. This is because super Earth formation in all traps leads to solid accretion from regions of the disk within 30 AU, and in most cases within 10 AU. In addition to observations of condensation fronts, future ALMA observations of chemical signatures in disks can be used to further constrain our disk chemistry model.

Compositions of exoplanet atmospheres can place additional constraints on our disk chemistry and planet formation models. By comparing atmospheric abundances of modelled planets with exoplanetary data, abundances of the underlying disks can be contrasted (Cridland, Pudritz & Alessi, 2016). While there are currently only several exoplanets with atmospheric abundance data, there are many future prospects whose compositional data may become available with the advent of JWST.

While gas phase chemistry throughout the disk is not a main focus of this paper, we are still able to track the gases our modelled planets accrete throughout their formation as computed by equilibrium chemistry. Our results show that Jovian planets have roughly Solar abundances in their atmospheres, which are composed almost entirely of molecular hydrogen and helium. This is a direct result of the initial condition of Solar abundances being assumed for the disk chemistry calculation. Variations in secondary gas abundances do exist between different Jovian planets formed in our model, however, and we discuss these below.

In table 2.7, we show the abundances of secondary gases for planets formed in the fiducial disk with a lifetime of 4 Myr (see figure 2.8). Among these four Jovian planets arising from each of the traps in our model, we see variations among the secondary gases that result from each planet's unique formation history. The location of each particular planet at the time when it undergoes runaway growth plays a key role in these results, as the disk's composition at this radius will be reflected in the planet's atmosphere.

For example, the planet formed in the cosmic ray dead zone undergoes runaway growth in the coolest region of the disk compared to the other planets. As a result, it has the largest abundance of H_2O, CH_4, and NH_3. Conversely, planets that accrete gas in hot regions of the disk, as is the case for the planet formed in the X-ray dead zone, achieve the highest compositions in CO, N_2, and SiO. In particular, the planet formed in the X-ray dead zone accretes the largest amounts of gaseous SiO due to it accreting gas from the hottest regions of the disk (small radii prior to 2 Myr into the disk's evolution). These results show that abundances of certain gases can constrain a planet's formation history to have taken place within a particular region of the disk.

2.4.2 Planet Formation Model

Planet-Planet Dynamics

Throughout this work, we have noted that traps intersect throughout the disk's lifetime. Thus, planets forming in these traps would undergo a dynamical interaction. Our work is limited as we do not account for the dynamical interaction between multiple forming planets. Rather, our planets form in isolation. Detailed N-body simulations in Hellary & Nelson (2012) show several interesting effects take place when dynamic interactions are accounted for while multiple planet cores are forming in a disk with an opacity transition. Handling the detailed dynamics between multiple forming planets in a disk with multiple traps is a prospect for future work, and in doing so we hope to see the effects of scattering and resonant traps in our model.

Oligarchic Growth or Pebble Accretion?

The first stage of our planet formation model assumes that planetary cores accrete km-sized solids via oligarchic growth, an N-body process. An alternative method of core growth has been proposed in recent models, such as in Ormel & Klahr (2010), and Bitsch, Lambrechts, & Johansen (2015), and is referred to as pebble accretion. In this model, planetary cores grow by accreting from a sea of cm-sized pebbles coupled to the gas. These cm-sized pebbles are seeded by forming via the streaming instability (Johansen et al., 2007), and their constant production can result in large accretion rates onto the planetary core, even in MMSN disks.

While our model uses oligarchic growth to handle solid accretion, it is possible that pebble accretion can be used as well, providing the important physical processes can be captured in a semi-analytic framework. If the two methods of solid core growth result in a 5-10 $M_{\oplus}$ core in less than 1 Myr, in principle they should not result in drastically different planets after gas accretion has been terminated. However, if the core growth timescales are drastically different, as the rapid core growth calculated using pebble accretion suggests it may be (Bitsch et al., 2015), the final locations of planets on the mass-semimajor axis diagram at the end of gas accretion may vary appreciably as a result.

Final Masses of Gas Giants

During the final phase of gas accretion, our planets undergo runaway growth, and are limited only by the Kelvin-Helmholtz timescale. In the final stages of planet formation in our model, the Kelvin-Helmholtz timescale allows the planet's accretion to supersede the accretion rate throughout the disk. Additionally, we parameterize the planet's final mass in terms of its gap opening mass, as opening a gap is a key step to shutting off gas flow onto a planet. This approach is necessary to limit the planet's mass from diverging prior to the disk being photoevaporated.

As discussed in section 2.4, other works, such as Machida et al. (2010); Dittkrist et al. (2014); Bitsch et al. (2015), & Mordasini et al. (2015) use an alternative approach to limit the accretion onto the planet. In these models, the gas accretion onto a planet is limited by the accretion rate throughout the disk. Using a time-dependent decreasing disk accretion rate can lead to the planets reaching a few Jupiter masses at the end of the disk's lifetime, avoiding an abrupt termination of gas accretion onto the planet. However, a disk-limited accretion model does require a parameterization of the fraction of the disk's accretion that gets accreted onto the planet, making the planets' final masses in this alternative approach dependent on model parameters pertaining to late stages of accretion. In both approaches, the model parameters are estimating the fraction of the available gas reservoir that gets accreted onto the planet.

Comparing these two methods, the Kelvin-Helmholtz timescale leads to planets moving upwards on the mass-semimajor axis diagram during stage III of their formation. The alternate model causes planets to move diagonally on the diagram, migrating inwards on a similar timescale as their accretion rate during this final stage of gas accretion. These two methods would lead to different final locations of planets at the end of their formation, and this will directly impact the mass-period relation the two models predict. In a future paper focusing on population synthesis, we will further compare the two methods in their ability to reproduce exoplanet data.

2.4.3 Extension to Planet Population Synthesis

By varying the disk's initial mass and lifetime, we have shown that our planet formation model can produce planets occupying entirely different regions of the mass-period diagram. For example, we have found that super Earth formation is strongly tied to the disk lifetime. Short-lived disks ($t_{LT} \lesssim 2$ Myr) typically result in the planets having insufficient time to accrete more than ~ 10 $M_\oplus$ of disk material, and are stranded at an early stage of their formation at the time of disk dispersal. Meanwhile, in sufficiently long-lived disks, we have shown in figure 2.10 that the types of Jupiters produced are tied not only to the traps that the planets formed within, but also to the mass of their natal disks. Heavier disks (0.15 $M_\odot$) typically result in planets forming at large semi-major axes, and are more prone to forming 1 AU Jupiters. Conversely, lighter disks (0.05 $M_\odot$) tend to form planets closer to their host stars, and may also result in super Earth formation due to a longer planet formation timescale in low mass disks.

The mutual effects of the disk's initial mass and lifetime provides a means of populating all the regions of the mass-period diagram coinciding with the observed locations of exoplanets. In a future work (Alessi et al. 2016, in prep.), we will employ a continuous range of these parameters within observational constraints in order to determine how frequently different regions of the mass-period diagram are populated, which is a similar approach taken in Hasegawa & Pudritz (2013).

In this work we have shown that planet traps define the regions of a disk that a planet can accrete from. In this way, super Earth compositions are tied to the trap they formed within, with each planet's composition reflecting the composition in the disk at the locations where it accreted its solids. In taking a population approach in our future work, we expect to find ranges of super Earth compositions that arise from formation in different traps. Based on our results in this work, we anticipate that traps sweeping past the ice line will produce super Earths with a variety of compositions. Meanwhile, we expect traps that do not migrate significantly will produce super Earths with relatively uniform compositions, regardless of the mass of the disk they form within.

With the model that has been developed in this paper, we are able to provide the initial conditions, namely a planet's mass and solid composition, necessary for models of interior structure of super Earths, such as Valencia et al. (2007). The variety of compositions predicted from super Earth formation in different planet traps can be extended with an interior model to predict a range of mean densities of these planets. For example, the dry and rocky planets will have higher densities than planets of the same mass with a substantial amount of ice. Interior models provide a link between planet compositions calculated with our model and planet's locations on the mass-radius diagram. In a similar approach to Mordasini et al. (2012b,c), combining an interior model with our future population approach will allow us to determine how our formed planets distribute themselves on the mass-radius diagram, allowing us to further compare with observations.

We note that the planets shown in table 2.6 have accreted non-negligible amounts of gas during their formation, ranging from 1.6 % by mass in the smallest case (2 Myr ice line) up to 27 % (corresponding to the 2 Myr cosmic ray dead zone planet). As shown in Lopez & Fortney (2013) a small amount of atmosphere can greatly increase the planet's radius. In this case, the planet's internal composition cannot be deduced from observations of the planet's radius. Our model does not track the evolution of the planets post-formation, or specifically their atmospheres. It is therefore unclear whether or not these planets would retain their atmospheres over billion-year timescales, and it remains possible that the planets' internal compositions are discernible through radius observations.

2.5 Conclusions

We have made a major extension of the model by Hasegawa & Pudritz (2011, 2012, 2013) by including the effects of disk chemistry in order to model the ice line's location, the dust to gas ratio, and most importantly, to track accreted solids onto super Earths. Our major findings in this work are listed below:

- Super Earth formation is linked to the timing of disk dispersal. Our model has resulted in super Earth formation in disks with lifetimes $\lesssim$ 2 Myr. Additionally, our model has produced super Earths in light disks (initial mass 0.05 $M_\odot$).

- Super Earths formed within the ice line and heat transition traps have substantial ice contents, ranging from 30 % of their masses and up to nearly 50 %. Conversely, both the X-ray and dead zone traps produce dry and rocky super Earths, with as little as 1 % of their mass in ice.

- Troilite and magnetite make up the majority ($\sim$ 70 % - 80 %) of the core materials in the super Earths formed in this paper. Meanwhile, enstatite and forsterite make up the majority ($\sim$ 75 % - 85 %) of these planets' mantle materials.

- The types of Jupiters formed in our model depend on the trap they formed within. In sufficiently long-lived disks (t_{LT} = 4 Myr) the heat transition and X-ray dead zone result in hot Jupiters while the ice line and cosmic ray dead zone produce Jupiters at 1 AU.

- Variations in secondary gas abundances exist among the Jovian planets formed with our model, and are sensitive to the disk temperature where the planets undergo runaway growth. Abundances of CO, N_2, and SiO result from gas accretion in hot regions of the disk, while accretion from colder regions of the disk results in higher abundances of H_2O, CH_4, and NH_3.

- We find that planet formation in the X-ray dead zone and heat transition traps are insensitive to the masses of the disks they form within. Planets forming from these two traps have final locations varying at most over 0.1 AU using a 0.05 $M_\odot$ - 0.15$M_\odot$ initial disk mass range.

- The cosmic ray dead zone and ice line traps result in planets whose masses and final locations are sensitive to disk mass. Increasing the disk mass from 0.1 $M_\odot$ to 0.15 $M_\odot$ increases the planet's final locations by up to an AU, while using a small disk mass of 0.05 $M_\odot$ resulted in super Earths forming out of these two traps.

We will extend these models in a future planet population synthesis paper that takes into account the ranges of disk parameters that can shape that observed mass-period relation of exoplanets.

Appendix A: Type-I Migration Regimes

As is discussed in Hellary & Nelson (2012) and Dittkrist et al. (2014), there are several type-I migration sub-regimes governing planet migration prior to the forming planet opening a gap in the disk. Namely, they are the locally isothermal regime, the trapped regime whereby the corotation torque is unstaturated, and lastly the saturated corotation torque regime.

Throughout this work we only considered the trapped type-I migration regime and here we validate that approach. As shown below, when considering alternate sub-regimes of type-I migration using our model's parameters, we find that planets in our model are always in the trapped type-I migration regime until they open a gap in the disk. This validates our assumption of trapped type-I migration prior to planets reaching their gap-opening masses.

We follow the approach in Dittkrist et al. (2014) that compared four distinct timescales to discern which sub-regime a type-I migrating planet belongs to. An important length scale in this discussion is the width of the horseshoe region, x_s, which denotes the range of radii around a planet where disk material will undergo horseshoe orbits. The form of x_s, taken from Masset & Papaloizou (2003) is,

$$x_s = 0.96 r_p \sqrt{\frac{q}{h_p}} \; , \tag{2.53}$$

where $q = M_p/M_*$, and $h_p = H_p/r_p$ is the disk's aspect ratio at the planet's location.

To distinguish between the locally isothermal regime (which can apply for planets $\lesssim 5M_\oplus$) and the trapped regime, we first compare the u-turn timescale, $t_{\text{u-turn}}$, and the cooling timescale, t_{cool}. The u-turn timescale characterizes how long it takes for a gas parcel on a horseshoe orbit to undergo a u-turn in front of or behind the planet,

$$t_{\text{u-turn}} = \frac{64 x_s h_p^2}{9 q r_p \Omega_p} \; . \tag{2.54}$$

The cooling timescale for the gas parcel undergoing a u-turn is (Dittkrist et al., 2014),

$$t_{\text{cool}} = \frac{l_{\text{cool}} \rho C_V}{8 \sigma T^3} \left(8 \rho \kappa l_{\text{cool}} + \frac{1}{\rho \kappa l_{\text{cool}}} \right) \; , \tag{2.55}$$

where l_{cool} is the minimum of H_p and x_s. Here $t_{\text{cool}} > t_{\text{u-turn}}$ implies that the planet is in the trapped regime (providing the corotation torque is not saturated, see discussion below), while $t_{\text{cool}} < t_{\text{u-turn}}$

implies the planet is in the locally isothermal regime.

To determine whether or not the corotation torque is saturated, we compare the viscous timescale (Masset & Papaloizou, 2003; Cridland et al., 2016),

$$t_{\rm vis} = \frac{x_s^2}{3\nu} \, , \tag{2.56}$$

to the libration timescale, characterizing the duration of a gas parcel's horseshoe orbit,

$$t_{\rm lib} = \frac{4\pi r_p}{1.5\Omega_p x_s} \, . \tag{2.57}$$

In this case, $f_{\rm vis}t_{\rm vis} < t_{\rm lib}$ implies that the corotation torque is unsaturated and the planet is trapped, while the converse case $f_{\rm vis}t_{\rm vis} > t_{\rm lib}$ implies that the corotation torque is saturated. The parameter $f_{\rm vis}$ is a factor of order unity introduced in Dittkrist et al. (2014) who considered a range of $f_{\rm vis}$ values from 0.125 - 1.0, but found that $f_{\rm vis} = 0.55$ provided a best fit between their model and hydrodynamics simulations.

For all planets tracks presented, we find the u-turn timescale to be longer than the cooling timescale for planet masses less than $\sim 3-5M_\oplus$ (depending on the specific trap used), meaning that the locally isothermal regime applies to low-mass planet cores in our model. We do not include the effects of this migration regime in this work, and force the low-mass planets to be trapped even when $t_{cool} < t_{u-turn}$. Additionally, we find the quantity $t_{\rm lib}/f_{\rm vis}t_{\rm vis}$ is greater than one for all planets prior to them opening a gap, implying that corotation torque saturation does not apply for planets in the type-I migration regime in our model.

In figure 2.15, we plot the ratio $t_{\rm lib}/f_{\rm vis}t_{\rm vis}$ for the four planets formed in the 4 Myr run in figure 2.8. Our results show that these planets have unsaturated corotation torques for all times until they open a gap in the disk. At a slightly higher mass, the corotation torques would saturate as $t_{\rm lib}/f_{\rm vis}t_{\rm vis} < 1$, but this argument no longer applies as the planets are in the type-II migration regime. We show the exact gap-opening masses and saturation masses, $M_{\rm sat}$ (defined to be the planet mass when $t_{\rm lib}/f_{\rm vis}t_{\rm vis} < 1$), for each planet track in the 4 Myr disk run in table 2.8. For planet formation in all four traps, the planets open gaps prior to their corotation torques saturating, implying that they are in the trapped regime for the entirety of type-I migration.

This timescale approach is an order-of-magnitude estimate of where the corotation torque sat-

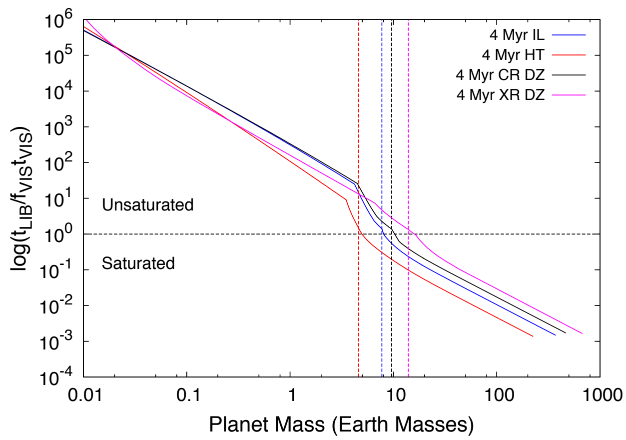

Figure 2.15: We plot the ratio $t_{\rm lib}/f_{\rm vis}t_{\rm vis}$ for the planets formed in the 4 Myr disk run. The vertical dashed lines represent the gap opening masses for each planet. The horizontal dashed line represents a ratio of one where the corotation torque saturates. In all cases, the planets reach their gap opening masses prior to the corotation torque saturating, meaning that they are in the trapped regime for the entirety of type-I migration.

Table 2.8: Here we show the gap-opening masses and corotation torque saturation masses (defined where $t_{\rm lib} = f_{\rm vis}t_{\rm vis}$) for each of the Jovian planets formed in the fiducial 4 Myr run (see figure 2.8). We also include the disk aspect ratio at the time and orbital radius where each planet opens a gap. Our results show that each planet opens a gap prior to its corotation torque saturating, validating our assumption that planets are trapped during type-I migration.

Trap	$M_{\rm gap}$ ($M_\oplus$)	$M_{\rm sat}$ ($M_\oplus$)	$h = H/r$
Ice Line	7.67	8.08	2.66×10^{-2}
Heat Transition	4.56	5	2.16×10^{-2}
C.R. Dead Zone	9.55	10.36	2.9×10^{-2}
X.R. Dead Zone	13.83	16.44	3.36×10^{-2}

urates. Furthermore, the results we obtain depend on the values of parameters, for example f_{vis}. While the results in this section show that this approach predicts that the corotation torque will not saturate during type-I migration with the current choices of parameters, a higher setting of f_{vis} will lead to the corotation torque saturating slightly before gap formation takes place. We predict, however, that the difference between M_{gap} and M_{sat} will be roughly a few tenths $M_\oplus$ for planet tracks in our model, making the saturated corotation torque phase short-lived. This will limit the effect that corotation torque saturation can have on planet tracks presented in this paper.

The planet tracks computed using our model are qualitatively similar to those presented in Dittkrist et al. (2014) during early phases of planet formation. We note, however, that their model includes the effects of multiple type-I migration sub-regimes in addition to the trapped phase. The other two sub-regimes (the locally isothermal regime and the saturated corotation torque regime) can cause the planet to undergo rapid inward migration or outward migration on timescales shorter than the disk's viscous timescale. This contrasts with the trapped inward migration on the viscous timescale planets in our model undergo.

Appendix B: Tracking Planet Compositions

The following algorithm is used to track planets' compositions throughout their formation. A time step of $\Delta t \sim 100 - 1000$ years is used during our planet formation runs.

1. Initial conditions: 0.01 $M_\oplus$ planet core at a radius coinciding with a planet trap at 10^5 years. The solid mass abundances in the disk at the planet's location are scaled up to 0.01 $M_\oplus$ to obtain the planet's initial composition.

2. Update the planet's orbital radius, $r_p(t)$, due to the inward migration during Δt. This could be either due to the planet trap moving inwards, or, for high mass planets, to type II migration. Steps 3 through 8 are skipped if the planet is in stage IV of its formation (accretion has stopped).

3. Calculate the disk's temperature, pressure, and surface density at r_p and the time into the disk's lifetime.

4. Calculate mass abundances of solids, $X_{i,\mathrm{solid}}(r_p(t), t)$ and gases, $X_{i,\mathrm{gas}}(r_p(t), t)$.

5. Calculate the accretion rate of solids, $\dot{M}_{p,\mathrm{solid}}$, onto the planet using equations 2.41 and 2.42. The mass $\dot{M}_{p,\mathrm{solid}}\Delta t$ is then added onto the planets current mass.

6. The amount of solid substances in the planet is updated using the local abundances of solids,

$$\begin{aligned} M_{i,\mathrm{planet}}(t) &= M_{i,\mathrm{planet}}(t-\Delta t) \\ &\quad + \dot{M}_{p,\mathrm{solid}}\Delta t X_{i,\mathrm{solid}}(r_p(t),t) \ . \end{aligned} \tag{2.58}$$

Steps 7 and 8 can be skipped if the planet in stage I ($M_p < M_{c,crit}$)

7. Calculate the accretion rate of gases, $\dot{M}_{p,\mathrm{gas}}$ using equations 2.44 and 2.45. The mass $\dot{M}_{p,\mathrm{gas}}\Delta t$ is then added onto the planet.

8. Update the amount of gaseous substances within the planet using the local abundance of gases,

$$\begin{aligned} M_{i,\mathrm{planet}}(t) &= M_{i,\mathrm{planet}}(t-\Delta t) \\ &\quad + \dot{M}_{p,\mathrm{gas}}\Delta t X_{i,\mathrm{gas}}(r_p(t),t) \end{aligned} \tag{2.59}$$

9. Repeat steps 2-8 throughout the planet's formation, until the time exceeds the disk's lifetime. At this point the gas will be dispersed, shutting off all accretion and planet-disk interactions (migration).

We denote the solid mass abundance of material or component i on a planet as the ratio between the component's mass on the planet, $M_{i,\mathrm{planet}}$, and the planet's total mass in solids, $M_{\mathrm{solid,planet}}$,

$$X^{\mathrm{solid}}_{i,\mathrm{planet}} = 100\frac{M_{i,\mathrm{planet}}}{M_{\mathrm{solid,planet}}}\ \% \ , \tag{2.60}$$

where we use planet in the subscript to distinguish between mass abundances throughout the disk.

Acknowledgments

We thank an anonymous referee for their useful comments that improved the quality of this manuscript. The authors would also like to thank Yasuhiro Hasegawa for his useful insights and discussions regarding this work. R.E.P. also thanks the MPIA and the Institut für Theoretische Astrophysik (ITA) in the Zentrum für Astronomie Heidelberg for support during his sabbatical leave (2015/16) during the final stages of this project. M.A. acknowledges funding from an Ontario Graduate Scholarship (OGS) and from the National Sciences and Engineering Research Council (NSERC) through a CGS-M scholarship. R.E.P. is supported by an NSERC Discovery Grant. A.J.C. acknowledges funding through the NSERC Alexander Graham Bell CGS/PGS Doctoral Scholarship.

Chapter 3

Foreshadowing Population Synthesis: Model Sensitivities

The planet formation model we presented in chapter 2 is sensitive to several parameters present in our core accretion model. We have alluded to the importance of the disk lifetime and mass in their roles in shaping the mass-semimajor axis distribution. Namely, the disk lifetime sets the upper limit that planets have to form. Low disk lifetime values often lead to super Earth formation in the core accretion model, while larger values give planets enough time to undergo runaway gas accretion and populate high mass zones of the mass-semimajor axis diagram. Additionally, the disk mass plays a key role in planet formation runs as it sets the column density of material throughout the disk, affecting accretion timescales of forming planets. In high mass disks, the planet formation timescale is short, favouring the formation of Jupiters at roughly 1 AU. Conversely, low mass disks lead to longer formation timescales, favouring the formation of super Earths, or hot Jupiters whereby the long formation timescale has allowed migration to carry the planets into small orbital radii.

In order to gain a complete understanding of a particular parameter's effect on the results of our core accretion model, a planet population synthesis approach is required that takes into account the entire range of disk lifetimes and masses as well as their statistical weighting from observed distributions. Using this method, one can analyze how the entire computed distribution is affected by varying this parameter, and can obtain a "best fit" value of said parameter by comparing to the observed distribution. While a full population study is beyond the scope of this thesis, we can still test the importance of certain parameters by considering choice values of a subset of key model parameters and show their effect on individual planet formation tracks.

In this chapter, we will explore the effects of varying important model parameters on the results of planet formation runs. Specifically, we will show the effects of varying the Kelvin-Helmholtz timescale parameters that set the rate of gas accretion onto planets in our model. Additionally, we will again explore the effects of varying the disk mass. As a supplement to the results presented in chapter 2, the results presented in this chapter will begin to show the disk mass's effect on super Earth compositions.

3.1 Kelvin-Helmholtz Parameters

During the initial gas accretion phase onto a planet in the core accretion scenario, the forming planet will be fully embedded in the gaseous disk. The outer boundary of the planet's envelope, or the planet's radius, can be defined as the location where the envelope's pressure is equal to the pressure of the surrounding disk material. In order for the planet to be accreting, surrounding disk material needs to be flowing into the planet's radius, leading to the requirement that the planet's atmosphere must be cooling and contracting. The rate at which accretion happens is controlled by how quickly the planet's envelope can cool and contract, and is governed by the Kelvin-Helmholtz timescale (equation 2.44).

As was discussed in section 2.2.4, the gas accretion timescale in the core accretion model can be expressed using the Kelvin-Helmholtz timescale, rewritten for convenience,

$$\tau_{KH} = 10^c \left(\frac{M_p}{M_\oplus}\right)^{-d} \text{ years} , \tag{3.1}$$

where c and d are constants. We employed fiducial values of $c = 9$ and $d = 3$ based on previous works such as Ikoma et al. (2000), Ida & Lin (2004), and Hasegawa & Pudritz (2013). Using this parameterization the gas accretion timescale for a 10 $M_\oplus$ core is,

$$\tau_{KH} = 10^9 \left(\frac{10\ M_\oplus}{1\ M_\oplus}\right)^{-3} \text{ years} = 10^6 \text{ years} , \tag{3.2}$$

while it is 10^3 years for a 100 $M_\oplus$ planet.

The particular values for the Kelvin-Helmholtz c and d parameters can be obtained as fits to hydrodynamic simulations that model the forming planet's gaseous envelope. The fitted-values are sensitive, however, to the grain opacity of the planet's envelope as it has strong effects on the forming planet's ability to cool and accrete. Using different envelope opacities, one can obtain a different fit to simulations and obtain a different set of Kelvin-Helmholtz parameters. Ikoma et al. (2000), Ida & Lin (2004), and Hasegawa & Pudritz (2014) have reported large ranges of the Kelvin-Helmholtz parameters, with a range of 8-10 for c and 2-4 for d. These large ranges are due to the uncertainty surrounding the correct value of grain opacity in the planet's envelope.

Owing to the effect of the envelope opacity, κ_{env}, on the Kelvin-Helmholtz timescale, previous authors have rewritten equation 3.1 directly including its effect (Bryden, Lin, & Ida, 2000),

$$\tau_{KH} = 10^{10} \left(\frac{M_p}{M_\oplus}\right)^{-3} \left(\frac{\kappa_{env}}{1 \text{ cm}^2 \text{ g}^{-1}}\right) . \tag{3.3}$$

Writing τ_{KH} this way directly connects the range of Kelvin-Helmholtz timescales to an uncertainty in the grain opacity in the forming planet's envelope. Lower envelope opacities allow the planet to cool and contract faster, leading to shorter accretion timescales in equation 3.3, and faster accretion rates.

Physically, we expect different forming planets to have a range of possible κ_{env} values due to forming in disks with differing metallicities, or due to accreting in regions of disks with different compositions. For example, accreting gas interior as opposed to exterior to the snow line will result in lower grain opacities. A recent semi-analytic treatment of the core accretion model presented in Hasegawa & Pudritz (2014) considered envelope grain opacities in the range of 8×10^{-3} cm^2 g^{-1} - 1 cm^2 g^{-1}. Additionally, the model presented in Mordasini et al. (2014) considered a full hydrodynamic model of the forming planet's envelope and considered a range of opacities of [0.003,1] cm^2 g^{-1}. Based on equation 3.3, these ranges of envelope opacities can vary the Kelvin-Helmholtz timescale by factors of $\sim$100.

Here, we consider $c = [8.5, 9.5]$, $d = [2.5, 3.5]$ as a plausible range of Kelvin-Helmholtz fitting parameters, and do not explicitly include the envelope opacity's effect on τ_{KH} (thus using equation 3.1). Even with this more constrained range of c and d values, different settings can vary the Kelvin-Helmholtz timescale by up to a factor of 100 depending on the planet's mass considered. However, this large range is in agreement with the range of envelope opacities considered in recent analytic core accretion models and is therefore justified.

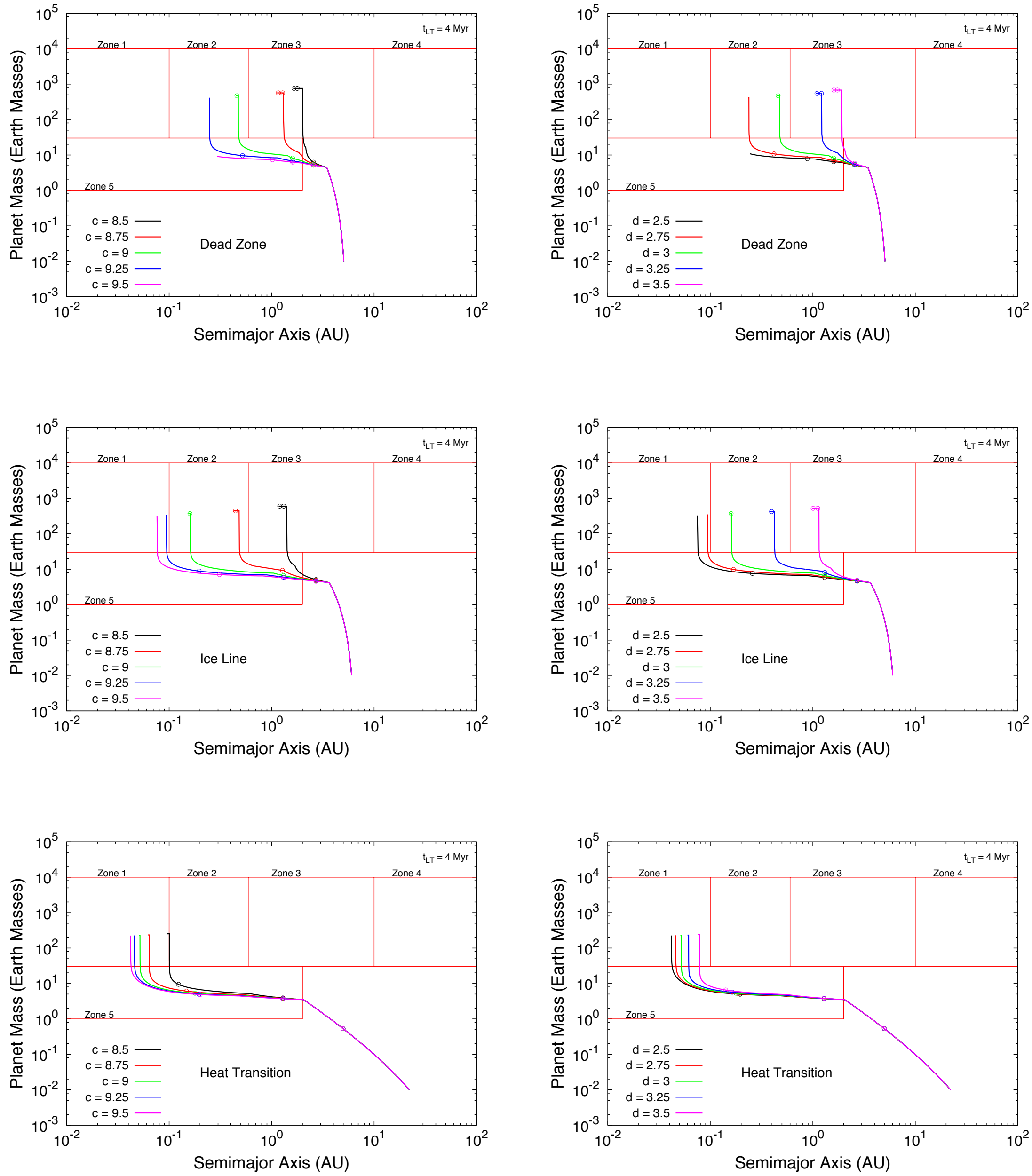

Figure 3.1: Planet formation tracks within each planet trap are shown while varying the Kelvin-Helmholtz timescale c (left) and d (right) parameters. The disk lifetime for all calculations is 4 Myr. The open circles on each formation track represent each planet's location after 1 Myr, 2 Myr, and 3 Myr of formation.

In figure 3.1, we show planet formation tracks in the cosmic ray dead zone, ice line, and heat transition while varying the K.H. c and d parameters. Within the C.R. dead zone and ice line traps, the K.H. parameters have a strong effect on the planet formation timescales, and the final locations of planets on the mass-semimajor axis diagram are highly sensitive to the particular settings of c and d used. Conversely, planet formation in the heat transition is less sensitive to the K.H. parameters, and with the range of values considered the resulting planets have different semimajor axes restricted to the hot Jupiter region of the diagram.

It is evident that our planet formation model is quite sensitive to K.H. parameters, especially when forming planets in the cosmic ray dead zone and the ice line. The range of K.H. parameters we have explored in figure 3.1 corresponds to the envelope opacity ranges considered in Hasegawa & Pudritz (2014) and Mordasini et al. (2014); roughly to values in the range of 0.01 - 1 cm^2 g^{-1}. From these results, we can conclude that the envelope grain opacity is an important parameter in this model as the rate of gas accretion onto planets is so strongly linked to its setting. Unfortunately, the envelope opacity values on forming planets is a somewhat poorly constrained parameter.

Detailed models of a forming planet's envelope opacity are difficult but will be necessary to further constrain their κ_{env} values. In order to model the opacity of a forming planet's envelope self-consistently, one needs to combine a disk chemistry model for solids with a dust model throughout the disk that outputs the size distributions of dust grains at different radii (as is done in Cridland, Pudritz & Birnstiel, in prep). Combining these two model parts would allow for grain size distributions and compositions within the planet's envelope to be tracked throughout formation. Coupling this information with an atmosphere model of the forming planet would allow for an estimation of κ_{env}. As was previously mentioned, planets are not expected to all have one κ_{env} value during their formation as every planet's unique formation history will allow it to accrete grains with different compositions and size distributions. Further study of κ_{env} values that forming planets acquire within disks of solar metallicity would constrain Kelvin-Helmholtz parameters and would inform semi-analytic gas accretion models such as the one presented in this thesis.

In contrast to detailed modelling of individual forming planets' envelope opacities, an additional method of constraining K.H. parameters is through a population synthesis approach. In such a study, one could compare the statistical mass-semimajor axis distribution output from our core accretion model to the observed exoplanetary distribution. The results presented in this section suggest that the computed distribution will be strongly dependent on the K.H. parameters. By finding a best-fit to the observed population, a population synthesis approach could draw out optimal τ_{KH} c and d parameters from a statistical standpoint, which would in turn determine the envelope opacity value that is best-suited to reproducing observed planet distributions. While this problem is degenerate in the sense that there could be multiple sets of c and d values that produce best fits to a population, one can constrain the K.H. parameters to a pair of c and d that correspond with a particular κ_{env} value.

3.2 Effects of Disk Mass on Super Earth Compositions

The exoplanetary population of super Earths displays an interesting variety of compositions inferred through their mean densities. They range from dense and rocky planets to those with substantial amounts of water or atmospheres. In chapter 2 of this thesis, we showed that our core accretion model with planet traps can reproduce a compositional variety among super Earths while only considering a fiducial initial disk mass of 0.1 $M_\odot$. This was an outcome of the planet traps themselves being located in different regions of the disk, causing planets to accrete from regions of the disk with distinct compositions.

The most important chemical signature in our disk model is the water ice line. Where a planet accretes with respect to the ice line determines its water content. In chapter 2, we showed that planets with substantial water contents accreted at, or outside the ice line in cold regions of the disk. This was the case for planets forming in the ice line or heat transition traps in the fiducial disk model. Conversely, planets accreting in hot regions of the disk interior to the snow line achieved dry and refractory-dominated compositions, which was the case for planets forming in the dead zone trap.

In this section, we extend this idea to disks with varying masses in order to determine the effect that disk masses have on resulting super Earth compositions. Since the planet traps set the radii where planets can accrete during early stages of formation whereby the planets build up their solid cores, determining the radii of the traps themselves in disks with different masses can allow for predictions of the resulting compositions of planets. As the locations of the planet traps are sensitive to column densities throughout the disk, we expect their locations to differ when different disk masses are considered. We define a parameter f_M, as a ratio of the disk's initial mass to the mass of the star, which is 1 $M_\odot$ in our model,

$$f_M \equiv \frac{M_{disk}}{M_*} = \frac{M_{disk}}{1\,\mathrm{M}_\odot}\ . \tag{3.4}$$

For the fiducial mass model, $f_M = 0.1$.

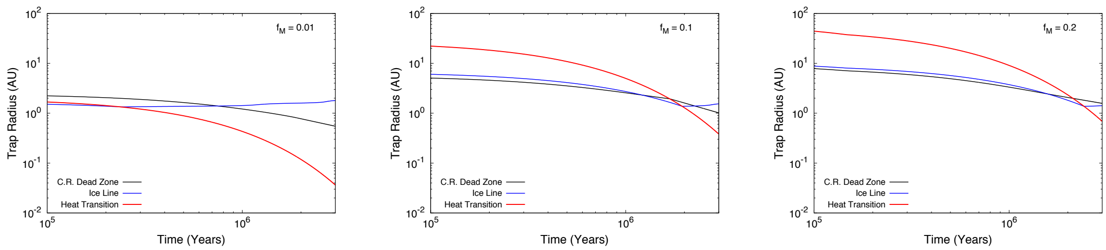

Figure 3.2: Planet trap evolution is shown in disks with varying masses. The left panel corresponds to a light disk with initial mass 0.01 $M_\odot$, the middle panel to a fiducial disk with an initial mass of 0.1 $M_\odot$, and the right panel to a heavy 0.2 $M_\odot$ initial mass. In the lightest disk, the heat transition is located primarily interior to the ice line, while the cosmic ray dead zone can be either inside or outside the ice line depending on the stage of disk evolution.

In figure 3.2, we plot the evolution of planet traps in our model within disks with different initial masses. We consider the fiducial initial disk mass of 0.1 $M_\odot$, as well as a light initial disk mass of 0.01 $M_\odot$ and a heavy initial mass of 0.2 $M_\odot$. This range of disk masses considered here is roughly representative of the range predicted observationally. As we consider heavier disk masses, the column density of disk material is increased throughout the disk, causing the locations of the traps to shift outwards. Comparing the 0.1 $M_\odot$ and 0.2 $M_\odot$ cases, all three traps are shifted outwards in the heavier disk, but the shape of their evolution profiles is roughly the same. Based on these results, we can predict that super Earth compositions resulting from formation in each planet trap will be similar when either the fiducial or heavier disk masses are considered.

The evolution profiles in the 0.01 $M_\odot$ initial disk mass case, however, look substantially different from the other two disk masses presented. While the heat transition lies outside the ice line in the fiducial disk mass model, we find that it lies interior to the ice line when considering the lighter disk. Additionally, the cosmic ray dead zone is situated outside the ice line in the 0.01 $M_\odot$ case while it is inside the ice line in the fiducial mass model. These results allow us to predict that super Earth compositions resulting from formation in the heat transition or dead zone will be significantly different when comparing the 0.01 $M_\odot$ and fiducial mass cases.

To test these composition predictions, we ran a set of planet formation models within disks with different initial masses. In these runs, we considered a short disk lifetime of 2 Myr so that our model would produce super Earths. We tracked the compositions of super Earths throughout their formation within each of the three planet traps for every disk mass considered.

Table 3.1: Results of planet formation runs in disks with 2-Myr lifetimes and varying disk masses (f_M values) are shown below. For planet formation in each trap, we present the final orbital radii (a_p), total planet masses (M_p), and planet core masses ($M_{core} = M_p - M_{gas}$) for varying disk mass (f_M) values. We also show the percentage of each planet's solid mass in irons, silicates, and water ice. In low-mass disks, super Earths formed in the cosmic ray dead zone accrete up to 25 % of their solid mass in ice, in contrast to the low value of 5.7 % in the fiducial disk mass (f_M=0.1) case. Conversely, super Earths formed in the heat transition in low mass disks show the opposite trend, with their water contents decreasing as lower-mass disks are considered.

Dead Zone						
f_M	a_p (AU)	M_p ($M_\oplus$)	M_{core} ($M_\oplus$)	% Iron	% Silicate	% Ice
0.01	0.78	2.46	2.44	34.3	46.3	19.4
0.05	1.26	5.78	4.94	32	43.2	24.8
0.1	1.61	8.11	5.92	40.2	54.1	5.7
0.15	1.85	10.47	6.5	40.2	54.2	5.6
0.2	1.82	18.11	7.17	40.6	54.7	4.7
Ice Line						
f_M	a_p (AU)	M_p ($M_\oplus$)	M_{core} ($M_\oplus$)	% Iron	% Silicate	% Ice
0.01	0.89	3.36	3.23	31.9	43	25.1
0.05	0.94	6.23	5.26	29.9	40.4	29.7
0.1	1.32	6.58	5.46	29.5	39.6	30.9
0.15	1.51	8.09	6.07	29.7	39.9	30.4
0.2	1.78	8.17	6.12	29.7	39.9	30.4
Heat Transition						
f_M	a_p (AU)	M_p ($M_\oplus$)	M_{core} ($M_\oplus$)	% Iron	% Silicate	% Ice
0.01*	0.086	10.26	9.39	38.3	59.6	2.1
0.05	0.68	4.47	4.28	24.3	32.7	43
0.1	1.3	3.74	3.68	22.2	30.1	47.7
0.15	1.72	3.64	3.6	21.9	29.9	48.2
0.2	2.35	3.52	3.5	21.9	29.8	48.3

$*t_{LT}$=1 Myr was used in this case.

In table 3.1 we present the results of this set of calculations. For each initial disk mass (f_M value) considered, we show the final orbital radius, total mass, core mass, and solid mass distribution among irons, silicates and ice corresponding to the super Earths that formed in each trap. We find that for the fiducial disk mass ($f_M = 0.1$) and heavier disk cases, the super Earth compositions are fairly consistent. This was expected based on the locations of the planet traps with respect to the water ice line.

Only when considering lighter disks ($f_M = 0.05$ or $f_M = 0.01$) did we find substantial compositional differences among super Earths. For example, the dead zone super Earths formed in these light disks achieved substantial water contents of up to 25 %, which is in contrast to the fairly dry planets (~ 5 % ice) that formed in the dead zone in the fiducial mass disk. This result suggests that in light disks, the dead zone planets build their solid cores in cold regions of the disk outside the ice line. We have confirmed this through tracking the dead zone's location in the disk in figure 3.2.

Super Earth formation in the heat transition also resulted in compositional differences when comparing the case of light disks to the fiducial mass model. Since the heat transition lies interior to the snow line in the light disk, planets forming in this trap accrete in warm, dry environments. This resulted in the $f_M = 0.01$ heat transition super Earth only accreting 2.1 % of its solid mass in ice, with the majority of its mass being comprised of iron and silicate based minerals. This is significantly different than the fiducial mass model results which found heat transition super Earths to have substantial amounts of water - close to 50 % of their solid mass.

Super Earths formed in the ice line did not show substantial compositional variety regardless of the disk mass considered. The ice abundance only varied by roughly 5 % among super Earths formed across the whole range of disk masses considered. Since the location of the ice line is defined by a chemical feature in the disk, it is not surprising that super Earth compositions resulting from formation in this trap are fairly uniform as the trap is forcing them to accrete from this particular chemical environment at the water phase transition.

The results presented in this section show that considering a large range of disk masses can result in super Earths formed in our model achieving an interesting variety of compositions. In this sense, our model predicts that a super Earth's composition is tied to both the planet trap it formed in and the mass of its natal disk. When extending this model to a population synthesis approach, we expect that it will be necessary to consider a large range of initial disk masses as well as planet formation in all three of our model's traps in order to reproduce the range of compositions and mean densities super Earths are observed to have. Additionally, we expect that the individual populations of super Earths formed in the cosmic ray dead zone and heat transition will themselves show a range of compositions due to the range of disk masses based on the results presented in this section, while the set of ice line super Earths will be fairly uniform in composition.

Chapter 4

Conclusions & Future Work

In this thesis we have presented a model that combines protoplanetary disk structure and chemistry with a core accretion model of planet formation that includes the effects of trapped type-I migration. In doing so, we have developed a method for tracking planet compositions during and post-formation in order to link super Earth compositions to their regions of formation in the disk. Our planet formation model has been able to produce planets in each zone of the mass-semimajor axis diagram, with the exclusion of zone 4 planets that have semimajor axes that are too large to be reproduced with this model. Furthermore, we have shown that our model can produce super Earths with a range of solid compositions and mean densities, as is shown by observed radii of super Earths. We discuss our major conclusions in this section.

The planet formation model has resulted in the formation of Jovian planets over a wide range of semimajor axes, populating zones 1, 2 and 3 of the mass semimajor axis diagram. The different traps we considered in our model favoured the formation of different classes of Jupiters. For example, the heat transition and X-ray dead zone traps favoured the formation of hot Jupiters due to the fast evolution of the traps into inner regions of the disk. Conversely, the ice line and cosmic ray traps produced zone 2 and zone 3 Jupiters near 1 AU in the fiducial model. The traps themselves lying in different locations in the disk causes planets forming within them to accrete from regions with different surface densities, thus having different core formation timescales. The interplay between the formation timescales and the trap migration timescale causes this model to produce Jovian planets over a range of semimajor axes, roughly 0.02 AU - 2 AU.

In this thesis, we considered two separate ionization sources - interstellar cosmic rays, and X-rays from the host star - that lead to different dead zone locations and time-dependencies. The cosmic ray dead zone was found to lie within 1-5 AU, moving slowly through the fiducial disk's evolution. The X-ray dead zone was conversely very sensitive to the disk's column density structure as the ionizing photons are attenuated by more disk material. In the fiducial model, the X-ray dead zone started far out in the disk at roughly 50 AU, but quickly evolved inside 0.5 AU within 1 Myr. The differences in dead zone location and evolution resulting from the two different ionization sources were caused by different ionizing photon energies and fluxes, as well as different radiation field geometry, with cosmic rays shining vertically downwards onto the disk while X-rays were modelled as a point source of ionization from the host star. Due to the location of the traps, the cosmic ray dead zone produced planets near 1 AU, while the X-ray dead zone favoured the formation of hot Jupiters near 0.1 AU. Further constraint of disk ionization sources and comparison with photochemical models is a prospect for future work.

We also studied the role the disk's mass plays in the result of planet formation runs. We found that heavier disks resulted in higher densities, and therefore overall shorter planet formation timescales. These set-ups favoured the formation of Jovian planets. Additionally, with shorter planet formation timescales, migration was seen to have smaller effects on planet formation tracks as the effects of migration had less time to impact forming planets. This favoured the formation of planets with larger orbital radii. Conversely, when lighter disks were considered, the longer planet formation timescale resulted in Jovian planets forming with shorter orbital timescales, or, in the case where the increased planet formation timescale exceeded the disk's lifetime, in super Earth formation.

The results of our planet formation model were shown to be sensitive to the Kelvin-Helmholtz parameters controlling the rate of gas accretion onto planets. Altering the Kelvin-Helmholtz c and d parameters within the ranges outlined in other works in the fiducial-mass disk allowed Jovian planets to form within the ice line and dead zone traps with a large range of radii, populating zones 1, 2, and 3. The heat transition trap was shown to be less sensitive to these parameters as all planet formation tracks produced hot Jupiters regardless of the parameter settings. The sensitivity of our model to these parameters reveals that further constraint of c and d is important. They physically are affected by the opacity of the forming planets' envelope, and detailed numerical models of κ_{env} that consider dust grain composition and size distributions within the planet's envelope may provide a means of constraining the K.H. parameters. Since gas accretion timescales in semi-analytic planet formation models are so sensitive to these parameters, future work in restricting their range of acceptable values will aid in models' predictability.

In the core accretion scenario, super Earth formation is tied to the timing of disk dispersal. Disks that dissipate during a planet's slow gas accretion phase strand the planet at roughly 5-15 $M_\oplus$. In this sense, super Earths are "failed Jupiters" in the core accretion model, as they are planets whose hydrostatic growth timescale was longer than their natal disk's lifetime, and therefore had insufficient time to reach the rapid runaway gas accretion phase of their formation. This result was seen to be robust in our planet formation model, as short disk lifetimes lead to super Earths forming in all planet traps considered.

By forming planets in different traps in our model, we were able to produce super Earths with a variety of compositions as is seen in the data. In a fiducial disk-mass model, both the cosmic ray and X-ray planet traps lie interior to the ice line, while the heat transition trap lies outside the ice line. This causes the dead zone traps to produce dry super Earths with less than 6 % of their solid mass in ice. Conversely, the ice line and heat transition traps produced ice-rich super Earths, with up to 50% of the planets' masses in ice. We have shown that the compositions of super Earths are tied to the traps they formed within, and the traps provide a link between the planet's final composition and the region of the disk where they accreted their solids.

We also considered super Earth formation in disks with different masses. When considering heavier disks, we found that the super Earth compositions resulting from formation in each trap were consistent with the fiducial mass model. Conversely, in light disks, we found that the cosmic ray dead zone lies exterior to the snow line, while the heat transition lies within the snow line. This is the opposite to the fiducial-mass model case. This leads to dry, rocky planets forming in the heat transition and ice rich planets forming in the dead zone in the light disk mass case.

Planet population synthesis represents a direct extension of this model and represents a prospect for future work. This thesis explored our planet formation model's sensitivity to the disk lifetime and mass, and a population synthesis approach will allow us to further explore this with a comprehensive statistical sampling of disk parameters. By fitting our computed planet population with observations, we can obtain best fit parameter values of model parameters that are somewhat unconstrained, such as the Kelvin-Helmholtz parameters. This also represents a means to compare competing models for different size regimes of the core accretion model. By comparing oligarchic growth and pebble accretion, for example, we can test the two models in their ability to reproduce observations.

The outputs of our modelled super Earths - providing planet masses and solid mass distributions among irons, silicates, and ice - provide the initial conditions for planet interior structure models. Including such models would allow us to calculate the radii of our formed planets and represents another direction for future work and application of this thesis' model. Interior structure calculations provide a means for mapping planets from the mass-semimajor axis diagram to the mass-radius diagram, and is a necessary step to further compare with observations. Additionally, estimating transit observational biases corresponding to modelled planets require the planet's radius to be known a priori, so calculating their radii with interior structure models will be useful to perform synthetic observations on computed planet populations from our model.

Bibliography

Aikawa Y., Herbst E., 1999, ApJ, 526, 314

Akiyama E., Hasegawa Y., Hayashi M., Iguchi S., 2016, ApJ, 818, 158

Alibert Y., Mordasini C., Benz W., Winisdoerffer C., 2005, A&A, 434, 343

Alibert Y., Carron F., Fortier A., Pfyffer S., Benz W., Mordasini C., Swoboda D., 2013, A&A, 558, A109

ALMA Partnership et al., 2015, ApJ, 808, L3

Andrews S.M., Williams J.P., 2005, ApJ, 631, 1134

Andrews S.M., Williams J.P., 2007, ApJ, 671, 1800

Armitage P.J., 2010, Astrophysics of Planet Formation, New York, NY: Cambridge University Press

Bai X.-N., Stone J.M., 2013, ApJ, 769, 76

Balbus S.A., Hawley J.F., 1991, ApJ, 376, 214

Baruteau C. et al, 2014, in Protostars and Planets VI, Beuther H., Klessen R.S., Dullemond C.P., Henning T. (eds.), Tucson: University of Arizona Press, pp. 667

Beckwith S.V.W., Sargent A.I., Chini R.S., Guesten R., 1990, A.J., 99, 924

Birnstiel T., Dullemond C.P., Brauer F., 2010, A&A, A79

Birnstiel T., Klahr H., Ercolano B., 2012, A&A, 539, A148

Bitsch B., Lambrechts M., Johansen A., 2015, A&A, 582, A112

Blaes O.M., Balbus S.A., 1994, ApJ, 421, 163

Bond J.C., O'Brien D.P., Lauretta D.S., 2010, ApJ, 715, 1050

Borucki W.J., et al., 2011, ApJ, 728, 117

Bryden G., Lin D.N.C., Ida S., 2000, ApJ, 544, 481

Butler R.P., Marcy G.W., 1996, ApJ, L153

Cassan A., et al., 2012, Nature, 481, 167

Ceccarelli C., Dominik C., López-Sepulcre A., Kama M., Padovani M., Caux E., Caselli P., 2014, ApJ, 790, L1

Chambers J.E., 2009, ApJ, 705, 1206

Chambers J.E., 2010, in Exoplanets, Seager S. (ed.), Tucson: University of Arizona Press, p. 297

Chiang E.I., Goldreich P., 1997, ApJ, 490, 368

Chiang E., Laughlin G., 2013, MNRAS, 431, 3444

Cieza F., Williams J., Kourkchi E., Andrews S., Casassus S., Graves S., Schreiber M., 2015, arXiv:1504.06040v2

Cleeves L.I., Adams F.C., Bergin E.A., 2013, ApJ, 772, 5

Cleeves L.I., Bergin E.A., Adams F.C., 2014, ApJ, 794, 123

Coleman G.A.L., Nelson R.P., 2014, MNRAS, 445, 479

Coleman G.A.L., Nelson R.P., 2016, arXiv:1604.05191v2

Crida A., 2009, ApJ, 698, 606

Crida A., Morbidelli A., Masset F., 2006, Icar, 181, 587

Cridland A.J., Pudritz R.E., Alessi M., 2016, arXiv:1605.09407v1

D'Alessio P., Cantó J., Calvet N., Lizano S., 1998, ApJ, 500, 411

D'Alessio P., Calvet N., Hartmann L., Lizano S., Cantó J., 1999, ApJ, 527, 893

D'Alessio P., Calvet N., Hartmann L., 2001, ApJ, 553, 321

D'Angelo G., Weidenschilling S.J., Lissauer J.J., Bodenheimer P., 2014, Icar., 241, 298

Dittkrist K.-M., Mordasini C., Klahr H., Alibert Y., Henning T., 2014, A&A, 567, A121

Eisner J.A., Hillenbrand L.A., White R.J., Akeson R.L., Sargent A.I., 2005, ApJ, 623, 952

Elser S., Meyer M.R., Moore B., 2012, Icar, 221, 859

Fleming T.P., Stone J.M., Hawley J.F., 2000, ApJ, 530, 464

Fortney J.J., Marley M.S., Barnes J.W., 2007, ApJ, 659, 1661

Fortney J.J., Mordasini C., Nettelmann N., Kempton E.M.-R., Greene T.P., Zahnle K., 2013, ApJ, 775, 80

Gammie C.F., 1996, ApJ, 457, 355

Glassgold A.E., Najita J., Igea J. 1997, ApJ, 480, 344

Goldreich P., Ward W.R., 1973, ApJ, 183, 1051

Goldreich P., Tremaine S., 1980, ApJ, 241, 425

Gressel O., Turner N.J., Nelson R.P., McNally C.P., 2015, ApJ, 801, 84

Gressel O., Pessah M.E., 2015, ApJ, 810, 59

Hartmann L., 1998, Accretion Processes in Star Formation, New York, NY: Cambridge University Press

Hasegawa Y., Pudritz R.E., 2010, ApJ, 710, L167

Hasegawa Y., Pudritz R.E., 2011, MNRAS, 417, 1236

Hasegawa Y., Pudritz R.E., 2012, ApJ, 760, 117

Hasegawa Y., Pudritz R.E., 2013, ApJ, 778, 78

Hasegawa Y., Pudritz R.E., 2014, ApJ, 794, 25

Hayashi C., 1981, Progr. Theor. Phys. Suppl., 70, 35

Hellary P., Nelson R.P., 2012, MNRAS, 419, 2737

Hernández J. et al., 2007, ApJ, 662, 1067

Howard A.W. et al., 2013, Nature, 503, 381

Hubickyj O., Bodenheimer P., Lissauer J.J., 2005, Icar, 179, 415

Hueso R., Guillot T., 2005, A&A, 442, 703

Ida S., Lin D.N.C., 2004, ApJ, 604, 388

Ida S., Lin D.N.C., 2008, ApJ, 673, 487

Ida S., Lin D.N.C., 2010, ApJ, 719, 810

Ida S., Lin D.N.C., Nagasawa M., ApJ, 2013, 775, 42

Ikoma M., Nakazawa K., Emori H., 2000, ApJ, 537, 1013

Ivanov P.B., Papaloizou J.C.B., Polnarev A.G., 1999, MNRAS, 307, 79

Jang-Condell H., Sasselov D.D., 2004, ApJ, 608, 497

Johansen A., Oishi J.S., Mac Low M.-M., Klahr H., Henning T., Youdin A., 2007, Nature, 448, 1022

Kley W., 1999, MNRAS, 303, 696

Kley W., Dirksen G., 2006, A&A, 447, 369

Kley W., Nelson R.P., 2012, Annu. Rev. Astron. Astrophys., 50, 211

Kokubo E., Ida S., 2002, ApJ, 581, 666

Lin, D.N.C., Papaloizou, J.C.B., 1993, in Protostars and Planets III, ed. E. H. Levy, J. I. Lunine, 749

Lissauer J.J., 1993, Annu. Rev. Astron. Astrophys. 31, 129.

Lissauer J.J., Hubickyj O., D'Angelo G., Bodenheimer P., 2009, Icar, 199, 338

Lopez E.D., Fortney J.J., 2013, ApJ, 776, 2

Lubow S.H., Seibert M., Artymowicz P., 1999, ApJ, 526, 1001

Lubow S.H., D'Angelo G., 2006, ApJ, 641, 526

Lubow S.H., Ida S., 2010, in Exoplanets, Seager S. (ed.), Tucson: University of Arizona Press, p. 347

Lynden Bell D., Pringle J.E., 1974, MNRAS, 168, 603

Lyra W., Johansen A., Zsom A., Klahr H., Piskunov N., 2009, A&A, 497, 869

Lyra W., Paardekooper S.-J., Mac Low M.-M., 2010, ApJ, 715, L68

Machida M.N., Kokubo E., Inutsuka S.-I., Matsumoto T., 2010, MNRAS, 405, 1227

Mamajek E.E., 2009, in AIP Conf. Ser. 1158, Exoplanets and Disks: Their Formation and Diversity, ed. T. Usuda, M. Tamura, & M. Ishii (Melville, NY: AIP), 3

Marcus P.S., Pei S., Jiang C.-H., Barranco J.A., Hassanzadeh P., Lecoanet D., 2015, ApJ, 808, 87

Marcy G.W., Butler R.P., 1996, ApJ, 464, L147

Masset F.S., 2001, ApJ, 558, 453

Masset F.S., 2002, A&A, 387, 605

Masset F.S., Papaloizou J.C.B., 2003, ApJ, 588, 494

Masset F.S., Morbidelli A., Crida A., Ferreira J., 2006, ApJ, 642, 478

Matsumura S., Pudritz R.E., 2003, ApJ, 598, 645

Matsumura S., Pudritz R.E., 2005, ApJ, 618, L137

Matsumura S., Pudritz R.E., 2006, MNRAS, 365, 572

Matsumura S., Pudritz R.E., Thommes E.W., 2007, ApJ, 660, 1609

Mayor M., Queloz D., 1995, Nature, 378, 355

Mayor M., et al., 2004, A&A, 415, 391

Mayor M., et al., 2011, arXiv:1109.2497v1

Melo C., et al., 2007, A&A, 467, 721

Menou K., Goodman J., 2004, ApJ, 606, 520

Min M., Dullemond C.P., Kama M., Dominik C., 2011, Icar, 212, 416

Mohanty S., Ercolano B., Turner N.J., 2013, ApJ, 764, 65

Mollière P., van Boekel R., Dullemond C., Henning T., Mordasini C., 2015, ApJ, 813, 1

Mordasini C., Alibert Y., Benz W., 2009, A&A, 501, 1139

Mordasini C., Alibert Y., Benz W., Naef D., 2009, A&A, 501, 1161

Mordasini C., Alibert Y., Benz W., Klahr H., Henning T., 2012, A&A, 541, A97

Mordasini C., Alibert Y., Klahr H., Henning T., 2012, A&A, 547, A111

Mordasini C., Alibert Y., Georgy C., Dittkrist K.-M., Klahr H., Henning T., 2012, A&A, 547, A112

Mordasini C., Klahr H., Alibert Y., Miller N., Henning T., 2014, A&A, 566, A141

Mordasini C., Mollière P., Dittkrist K.-M., Jin S., Alibert Y., 2015, International Journal of Astrobiology, 14, 201

Moriarty J., Madhusudhan N., Fischer D., 2014, ApJ, 787, 81

Morton T.D. et al., 2016, arXiv:1605.02825

Öberg K.I., Adwin Boogert A.C., Pontoppidan K.M., Van Den Broek S., Van Dishoeck E.F., Bottinelli S., Blake G.A., Evans II N.J., 2011, ApJ, 740, 109

Oppenheimer M., Dalgarno A., 1974, ApJ, 192, 29

Ormel C. W., Klahr H. H., 2010, A&A, 520, A43

Owen J.E., Ercolano B., Clarke C.J., 2011, MNRAS, 412, 13

Padovani M., Hennebelle P., Marcowith A., Ferrière K., 2015, arXiv:1509.06416v1

Pascucci I., Sterzik M., 2009, ApJ, 702, 724

Pasek M., Milsom J., Ciesla F., Lauretta D., Sharp C., Lunine J., 2005, Icar, 175, 1

Pignatale F.C., Maddison S.T., Taquet V., Brooks G., Liffman K., 2011, MNRAS, 414, 2386

Pollack J.B., Hubickyj O., Bodenheimer P., Lissauer J.J., Podolak M., Greenzweig Y., 1996, Icar, 124, 62

Pontoppidan K.M., Salyk C., Bergin E.A., Brittain S., Marty B., Mousis O., Öberg K.I., 2014, in Protostars and Planets VI, Beuther H., Klessen R.S., Dullemond C.P., Henning T. (eds.), Tucson: University of Arizona Press, pp. 363-386.

Pudritz R.E., Norman C.A., 1986, ApJ, 301, 571

Qi C., D'Alessio P., Öberg K.I., Wilner D.J., Hughes A.M., 2011, ApJ, 740, 84

Roberge A., Kamp I., 2010, in Exoplanets, Seager S. (ed.), Tucson: University of Arizona Press, p. 269

Rowe J.F. et al., 2014, ApJ, 785, 45

Sano T., Miyama S.M., Umebayashi T., Nakano T., 2000, ApJ, 543, 486

Shakura N.I., Sunyaev R.A., 1973, A&A, 24, 337

Siess L., Dufour E., Forestini M., 2000, A&A, 358, 593

Simon J.B., Bai X.-N., Stone J.M., Armitage P.J., Beckwith K., 2013, ApJ, 764, 66

Spitzer L.J., Tomasko M.G., 1968, ApJ, 152, 971

Stepinski T.F., 1998, Icar, 132, 100

Tanaka H., Takeuchi T., Ward W.R., 2002, ApJ, 581, 1344

Testi L., 2014, in Protostars and Planets VI, Beuther H., Klessen R.S., Dullemond C.P., Henning T. (eds.), Tucson: University of Arizona Press, pp. 339

Thomas S.W., Madhusudhan N., 2016, MNRAS, 458, 1330

Toppani A., Libourel G., Robert F., Ghanbaja J., 2006, Geochimica et Cosmochimica Acta, 70, 5035

Udry S., Santos N.C., 2007, ARAA, 45, 397

Umebayashi T., Nakano T., 1981, PASJ, 33, 617

Valencia D., Sasselov D.D., O'Connell R.J., 2006, Icar., 181, 545

Valencia D., Sasselov D.D., O'Connell R.J., 2007, ApJ, 665, 1413

Visser R., Bergin E.A., 2012, ApJ, 754, L18

White W.B., Johnson S.M., Dantzig G.B., 1958, J. Chem. Phys., 28, 751

Williams J.P., Andrews S.M., Wilner D.J., 2005, ApJ, 634, 495

Wolfgang A., Rogers L.A., Ford E.B., 2015, ApJ, 825, 19

Youdin A.N., Goodman J., 2005, ApJ, 620, 459

Zhang K., Pontoppidan K.M., Salyk C., Blake G.A., 2013, ApJ, 766, 82

Zhang K., Blake G.A., Bergin E.A., 2015, ApJ, 806, L7